Claudio Ledovich

Preliminary studies for a measurement of B-mixing with di-muon events in CMS

Tesi di Laurea Magistrale in Fisica

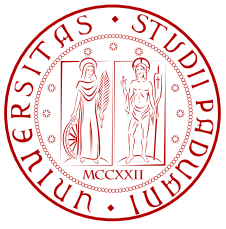

Relatore: dott. Franco Simonetto
Co-relatore: dott. Martino Margoni

Universitá degli Studi di Padova
Dipartimento di Fisica e Astronomia “Galileo Galilei”
Anno accademico 2011–2012

a Dario,
insieme prima ancora di conoscerci...

Contents

Chapter 1

Introduction

Due to the large b-quark production cross section, high statistics data samples are available soon after the LHC startup. This makes the CMS experiment an excellent facility for the study of heavy flavor physics. Even though the CMS detector is primarily designed for high transverse momentum physics, it is very well suited for heavy flavor physics thanks to the muon system capable to identify low transverse momentum muons and the excellent tracking detectors.

This thesis consists in a preliminary study for a measurement of the B-mixing with the CMS experiment at the LHC. In particular it is divided in two studies. First one is the analysis of the *pile-up*: here we evaluate the pile up effect for the dimuonic analysis in data 2010 and 2011; the aim is to subtract this effect in the subsequent measurement of the B-mixing . In the second analysis we want to determine the angular resolution in the measurement of the B-direction. In this case we take not only muons but also jets. Here we compare real data (2010) with a Monte Carlo simulation to evaluate the smearing in resolution between them. These measures are among the possible cause of systematic error in a measure of the average time integrated mixing probability, $\bar{\chi}$.

The contents are organised as follows.

In Chapter 2 a brief summary on the Standard Model is reported, with particular attention for the B-mixing and the measurements of $\bar{\chi}$ at the end of the chapter. In Chapter 3 is presented the CMS detector at LHC, here an overview of the Monte Carlo event generators used in the analysis and the selections on the data are briefly presented. In Chapter 4 the analysis of pile up is presented and in Chapter 5 the studies on the angular resolution in the measurement of the B-direction. Conclusions are outlined in Chapter 6.

Throughout this thesis, natural units are used in which $c = \hbar = 1$.

Chapter 2

Introduction to the Standard Model

In this chapter we review the Standard Model (SM) of particle phisycs. Since its introduction in the early 1970's by Sheldon Glashow [1], Steven Weinberg [**?**] and Abdus Salam [3], it has successfully explained a wide range of experimental results and precisely predicted a large variety of phenomena from the elementary world to the universe.

SM is the theory describing the elementary particles and their interactions. It was conceived after more than 50 years of theoretical works and is based on the fundamental concepts of quantum field theory and on the experimental observations. Quantum field theory is based on concepts of special relativity and quantum mechanics. Particles are represented by relativistic fields obeying to specific propagation equations. In particular a field theory introduces creation and annihilation operators to take into account the possible creation and annihilation of particles.

SM consists of 12 spin-$\frac{1}{2}$ fermions and 12 spin-1 gauge bosons which act as carrier of the fundamental forces[1]. Three of the four fundamental forces, namely electromagnetism, weak interaction and strong interaction, are included in the SM. The gravitational force which is dominant at macroscopic distances is omitted since its effects are small on microscopic scales[2]. The 12 fermions are divided into 6 quarks (u, d, s, c, b, t) and 6 leptons (e, μ, τ, ν_e, ν_μ, ν_τ), all of which possess charge conjugate states, called anti-particles.

All quarks and leptons are subject to the weak force, while only quarks and charged leptons (e, μ, τ) undergo electromagnetic interactions. A major achievement of the SM is the unification of the electromagnetic and the weak force into an electroweak force embedded in the theory of Quantum Electrodynamics (QED). In QED the photon is the gauge boson of the electromagnetism and the W- and Z-bosons are the mediators of the weak interaction. The strong force is responsible for the interaction between color charged quarks (*red, green* and *blue*) and gluons (g, there are 8 gluons) where the latter are the mediators in the theory of Quantum

[1]Fermions have semi-integer spin values and follow the Fermi-Dirac statistics while bosons have integer ones and are described by the Bose-Einstein statistics.

[2]The coupling constant of the gravitational interactions is about forty order of magnitude smaller than the coupling constant of the other ones.

Chromodynamics (QCD).

To resume all these particles see the Tables 2.1, 2.2 and 2.3.

Flavour	Charge	Quantum Number	Mass [GeV]
e	-1	$L_e = +1$	0.511×10^{-3}
ν_e	0	$L_e = +1$	$< 225 \times 10^{-9}$
μ	-1	$L_\mu = +1$	105.7×10^{-3}
ν_μ	0	$L_\mu = +1$	$< 0.19 \times 10^{-3}$
τ	-1	$L_\tau = +1$	1.777
ν_τ	0	$L_\tau = +1$	$< 18.2 \times 10^{-3}$

Table 2.1: Flavour, charge, quantum number and mass of leptons [4].

	Interaction	Charge	Mass [GeV]	Width [GeV]
g	strong	0	0	
γ	electromagnetic	0	0	
Z^0	weak	0	91.1876 ± 0.0021	2.4952 ± 0.0023
$W^\pm$	weak	± 1	80.398 ± 0.025	2.141 ± 0.041

Table 2.2: Charge, mass and width of force carriers [4].

Flavour	Charge	Quantum Number	Mass [GeV]
u	$+2/3$	$U = +1$	$(1.5 \div 3.3) \times 10^{-3}$
d	$-1/3$	$D = -1$	$(3.5 \div 6.0) \times 10^{-9}$
c	$+2/3$	$C = +1$	$1.27^{+0.07}_{-0.11}$
s	$-1/3$	$S = -1$	$104^{+26}_{-34} \times 10^{-3}$
t	$+2/3$	$T = +1$	171.2 ± 2.1
b	$-1/3$	$B = -1$	$4.2^{+0.17}_{-0.07}$

Table 2.3: Flavour, charge, quantum number and mass of leptons [4].

To colmplete the SM it was introducted another particle, the *Higgs boson*. The Higgs boson plays an important role in the SM as it provides an explanation for the masses of the elementary particles and gives rise to the phenomenon of electroweak symmetry breaking. The search for the Higgs particle has been one of the main motivations for the construction of the Large Hadron Collider (LHC) at CERN.

2.1 Electroweak interaction

The electroweak theory unifies the weak and the electromagnetic interactions under the simmetry group $SU(2)_L \times U(1)_Y$. The L refers to the fact that the constituent of the weak interaction are left-handed weak isospin doublets, while the Y is a reminder that the U(1) group contains right-handed weak hypercharge singlets. The left-handed fermion fields

$$\psi_i = \begin{pmatrix} \nu_i \\ \ell_i^- \end{pmatrix} \text{ and } \begin{pmatrix} u_i \\ d_i' \end{pmatrix}$$

for the i-th fermion family transform as doublets under $SU(2)$ while the right-handed ones are singlets of $SU(2)$. The weak isospin and the hypercharge Y are respectively the generators of the symmetry transformations. Defined T_3 the third component of the weak isospin vector and Q the electric charge, we have the relation

$$Q = T_3 + \frac{Y}{2}.$$

Now, the electoweak Lagrangian is given by

$$\mathcal{L} = -\frac{1}{4}W^{\mu\nu}W_{\mu\nu} - B^{\mu\nu}B_{\mu\nu} + i\bar{\psi}\not{D}\psi \tag{2.1}$$

where we can define the covariant derivative operator as

$$D_\mu = \partial_\mu + igW_\mu T + \frac{i}{2}g'B_\mu Y$$

where T is the weak isospin operator while g and g' are two different coupling constants for the electroweak interactions, g for $SU(2)_L$ and g' for $U(1)_Y$. If we define B_μ as the the massless gauge field representing the singlet of $U(1)_Y$, therefore $B_{\mu\nu}$ is the follow tensor, similar to the electromagnetic one

$$B_{\mu\nu} = \partial_\mu B_\nu - \partial_\nu B_\mu.$$

Defined W_μ as the the gauge field of $SU(2)$, we can define the tensor

$$W_{\mu\nu} = \partial_\mu W_\nu - \partial_\nu W_\mu.$$

We have to do an important precisation: W^1_μ, W^2_μ, W^3_μ and B_μ fields have no physical meaning, the physical fields are A_μ, Z_μ and $W^\pm_\mu$. A_μ is a neutral electromagnetic field, Z_μ describes the weak neutral current while $W^\pm_\mu$ are the weak charge current fields. The fields with which the weak Lagrangian is defined are related to the physical ones by the transformation leads by the *weak angle* (or Weinberg's angle) θ_W

$$\begin{pmatrix} Z \\ A \end{pmatrix} = \begin{pmatrix} \cos\theta_W & -\sin\theta_W \\ \sin\theta_W & \cos\theta_W \end{pmatrix} \begin{pmatrix} W^3 \\ B \end{pmatrix}$$

There is also a relation between the electromagnetic coupling constant e and the coupling constants g and g'

$$e = g\sin\theta_W = g'\cos\theta_W$$

and accordingly

$$g' = g\tan\theta_W$$

The fields W^1_μ and W^2_μ are related to the observable fields $W^\pm_\mu$ by the relation

$$W^\pm_\mu = \frac{1}{\sqrt{2}}(W^1_\mu \mp W^2_\mu)$$

and for the fields Z_μ and A_μ we have

$$Z_\mu = \frac{-g' B_\mu + g W_\mu^3}{\sqrt{g^2 + g'^2}} \qquad A_\mu = \frac{g B_\mu + g' W_\mu^3}{\sqrt{g^2 + g'^2}}$$

Finally we can rewrite the term $i\bar{\psi}\not{D}\psi$ in the electroweak Lagrangian (2.1) responsible for the interaction for quarks and leptons with the gauge bosons as

$$e J_{EM}^\mu A_\mu + \frac{g}{\sqrt{2}}(J_L^{+\mu} W_L^+ + J_L^{-\mu} W_L^-) + \frac{g g'}{e} J_Z^\mu Z_\mu$$

where we have introducted the weak charge currents $J_L^{\pm\mu}$, the weak neutral current J_Z^μ and the electromagnetic current J_{EM}^μ, respectively

$$J_L^{\pm\mu} = \sqrt{2}\bar{\psi}\gamma^\mu T_L^{\pm\mu}\psi$$

$$J_Z^\mu = \bar{\psi}\gamma^\mu(T_{3L} - Q\sin^2\theta_W)\psi$$

$$J_{EM}^\mu = \bar{\psi}\gamma^\mu Q\psi$$

Since the electroweak Lagrangian mass terms for the gauge bosons violate the gauge invariance, the bosons need to be massless. While the photon is in fact massless, the short range feature of the weak interactions and the experimental measurements show that Z and $W^\pm$ are effectively massive, their mass having been measured with high precision at LEP [5] and Tevatron [6]:

$$m_Z = 91.1876 \pm 0.0021 \text{ GeV}$$

$$m_W = 80.425 \pm 0.038 \text{ GeV}$$

The mathematical mechanism which allows the introduction of gauge boson masses is based on the *spontaneous electroweak symmetry breaking* in presence of a scalar field: the Higgs field.

Moreover, the quark mass eigenstates are not proper states of the flavour basis. The flavour interaction eigenstates are instead linear combinations of the mass eigenstates. A unitary mixing matrix is therefore introduced in the theory, corresponding to the base change from the interaction eigenstates to the mass eigenstates one. This matrix is called Cabibbo-Kobayashi-Maskawa or CKM matrix [7, 8]:

$$\begin{pmatrix} d' \\ s' \\ b' \end{pmatrix} = \begin{pmatrix} V_{ud} & V_{us} & V_{ub} \\ V_{cd} & V_{cs} & V_{cb} \\ V_{td} & V_{ts} & V_{tb} \end{pmatrix} \begin{pmatrix} d \\ s \\ b \end{pmatrix} \tag{2.2}$$

where the down quark vector on the left side of the equation correspond to the interaction eigenstates and the vector to the right side of the CKM matrix are the mass eigenstates. It must be noted that the diagonal elements of this matrix have values close to 1, which favors the flavour exchange within the same generation.

2.2 Heavy Flavour Physics

The study of heavy quark production is an important research area at the LHC. Heavy quarks will be produced with a large cross section at a yet unreached center-of-mass energy, enabling precision measurements to improve our understanding of heavy flavour physics. In the context of this work the term heavy quark stands for charm and beauty quarks since the mass of the up, down and strange quark are significantly lower. The heavier top quark has a very short lifetime and does therefore not form bound states of heavy hadrons because it is not able to hadronize before to decay.

Heavy quark production is interesting on its own as it presents a key process for the study of the theory of strong interactions, Quantum Chromodynamics (QCD). Furthermore, a well-established theory of heavy quark production is needed for many searches at the LHC.

In this section the theoretical concepts relevant to describe the physics of heavy quarks at the LHC are introduced. The main ideas of Quantum Chromodynamics are reviewed, before their application to high-energy hadron-hadron collisions is discussed. This includes the factorization ansatz, the evolution of the parton distribution functions, the partonic processes important for beauty quark production and the phenomenological treatment of heavy quark fragmentation. A further section is dedicated to the description of the decay of b-hadrons via the weak interaction. The Monte Carlo event generators which are used in this analysis to generate full hadronic events within the QCD framework are presented in the last section.

2.2.1 Quantum Chromodynamics

QCD [9, 10, 11] is the field theory describing the strong interaction between color charged partons. Color charge comes in three versions (red, green and blue) which form a fundamental representation of the SU(3) symmetry group and is carried by massive spin-$\frac{1}{2}$ quarks and massless spin-1 gluons. Analogous to the photons in Quantum Electrodynamics (QED) [12, 13], the gluons are the gauge bosons in QCD and mediate the strong interaction. Since the gluons themselves carry color charge, they can directly interact with other gluons. This possibility is not available in QED, as photons do not have an electric charge.

In QCD, as in any renormalizable quantum field theory, ultraviolet divergences appearing in the calculation can be removed by introducing a scale dependent coupling $\alpha_s(Q^2)$ and a new scale, the renormalization scale μ_R [14]. The dependence of α_s on the energy-scale Q^2 is known as running of the coupling. A summary of measurements of $\alpha_s(Q^2)$ as a function of the respective energy scale Q is presented in Figure 2.1 . At the scale set by the mass of the Z boson the average value of the strong coupling constant is $\alpha_s(M_Z) = 0.1184 \pm 0.0007$ [15]. The renormalization scale is used to set the validity limit of the perturbative approach, is usually defined as Λ_{QCD} and experimentally is found to be of the order of 200 MeV [16]. At energy scales below Λ_{QCD} the strong coupling rises to infinity, resulting in the confinement of quarks and gluons inside color-singlet hadrons. The use of

a perturbative approach is instead legitimate at scales $Q^2 \gg \Lambda_{QCD}$.

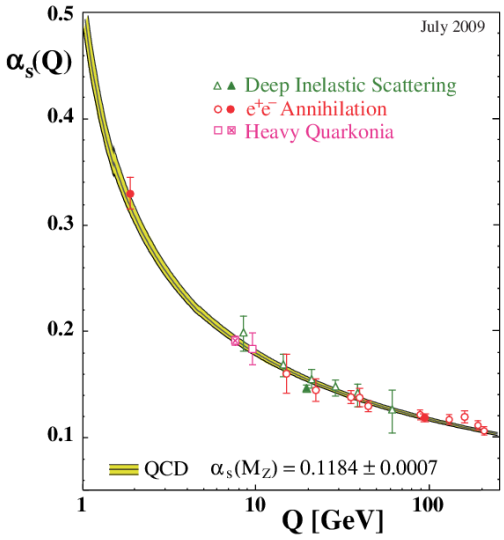

Figure 2.1: Summary of measurements of α_s as a function of the respective energy scale.

Hadronic Collisions

Due to the asymptotic freedom in QCD, the interaction between quarks and gluons becomes arbitrarily weak at short distances. Consequently hadrons behave as collections of free parton at large transferred momenta and their interaction can therefore be described using a parton model.

A generic scattering process of two hadrons $(h_1; h_2)$ with four-momenta P_1 and P_2, respectively, is illustrated in figure 2.2. The scattering process is caused by the interaction of two partons of the initial hadrons with four-momentum $p_1 = x_1 P_1$ and $p_2 = x_2 P_2$.

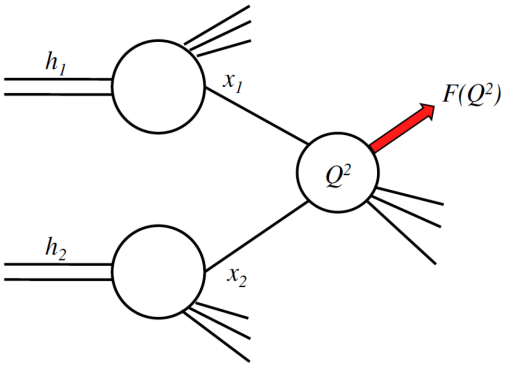

Figure 2.2: Scattering process of two hadrons h_1 and h_2 in the parton model. Two partons with momentum fractions x_1 and x_2 undergo an hard interaction at the scale Q^2.

Since the center-of-mass of the partonic interaction is normally boosted with respect to the laboratory frame, it is useful to classify the final state according to

variables that are invariant under longitudinal boosts. The squared center-of-mass energy of the hadronic system is

$$s = (P_1 + P_2)^2. \tag{2.3}$$

In the massless limit, the virtuality of the process is defined as

$$Q^2 = \hat{s} = x_1 x_2 s. \tag{2.4}$$

The momentum imbalance of the partons participating in the hard interaction is reflected in the rapidity distribution of the outgoing particles. The transverse momentum of the outgoing partons in the center-of-mass frame of the colliding partons is denoted by $\hat{p_T}$ and is of particular interest for the Monte Carlo event generators (see section ....).

Factorization

Soft processes resulting in the production of low momentum hadrons will be the most common events in proton-proton collision at the LHC. Although these processes are QCD related, they cannot be calculated by perturbative QCD (pQCD). Perturbative approaches only lead to reliable results if a hard scale is present in the interaction. In the case of heavy flavour physics, the hard scale is provided by the mass of the heavy quark, its transverse momentum or the virtuality of the process.

Most of the processes calculated by pQCD feature infrared divergences emerging from real gluon emission. Singularities arise either if a gluon is emitted in the direction of the outgoing parton (collinear divergences) or if a low momentum gluon is emitted (soft divergence). Similar to the ultraviolet divergencies which are removed by introducing a renormalization scale, μ_R, the infrared divergencies can be absorbed when imposing a factorization scale, μ_L . The factorization scale can be thought of as the scale which separates the short- and the long-distance physics. The short-distance part covers the hard process calculable in pQCD, while the long-distance part includes the collinear and soft divergencies which are not accessible to perturbative calculations. The factorization ansatz is validated by the factorization theorem [17, 18, 19].

According to the factorization theorem the cross section for a hard scattering originating from an interaction of two hadrons with four-momenta P_1 and P_2 can be written as

$$\sigma(P_1, P_2) = \sum_{i,j} \int \mathrm{d}x_1 \mathrm{d}x_2 \, f_i^{h_1}(x_1, \mu_F^2) \, f_j^{h_2}(x_2, \mu_F^2) \, \hat{\sigma}_{i,j}(x_1 P_1, x_2 P_2, \alpha_s(\mu_R), Q^2; \mu_F^2, \mu_R^2) \tag{2.5}$$

where:

- $f_i^h(x, \mu_F^2)$ is the parton distribution function (PDF) for the parton i in the hadron h,
- x_1 is the momentum fraction of the hadron h_1 carried by the parton i,

- x_2 is the momentum fraction of the hadron h_2 carried by the parton j,
- $\hat{\sigma}_{i,j}$ is the short-distance scattering cross section of partons i and j,
- μ_R is the renormalization scale, and
- μ_F is the factorization scale.

The parton distribution functions $f_i^h(x, \mu_F^2)$ describe the probability of extracting a parton i from a hadron h with momentum fraction x. Hence, the factorization theorem implies that the probability of extracting the parton can be treated independently from the parton undergoing an interaction. This assumption was successfully verified in deep inelastic lepton-hadron scattering (DIS) which is characterized by a large virtuality ($Q^2 \gg \Lambda_{QCD}$). In the DIS regime, the factorization theorem is proven to be valid to all orders in perturbation theory [19]. Nonetheless it is not obvious that the factorization theorem can be adapted to hadron-hadron collisions since gluons from the hadron remnant might interact and spoil the factorization. Explicit calculations have shown that factorization breaking effects are present but are suppressed by powers of Λ_{QCD}/Q^2 in the high energy limit [20]. The partonic short-distance cross section $\sigma_{i,j}$ can be computed in pQCD as

$$\hat{\sigma}_{i,j} = \alpha_s^k \sum_n \left(\frac{\alpha_s}{\pi}\right)^n c_{ij}^{(n)} \tag{2.6}$$

were the coeffcients $c(n)$ are functions of the kinematic variables and the factorization scale. Different hard processes will contribute with different leading powers k to the partonic cross section.

Evolution of Parton Distribution Functions

As discussed in the previous section the long-distance, non-perturbative part of the cross section is absorbed in scale dependent PDFs which cannot be calculated by pQCD. Nevertheless, the dependence on the factorization μ_F is described by perturbative calculation. The pQCD parton evolution equations predict the evolution of the PDFs to any scale $Q > Q_0^2$ once $f_i^h(x, Q_0^2)$ is known at a starting scale Q_0^2. The scale dependence of the PDFs is a consequence of gluon radiation and gluon splitting effects, which are incorporated in the DGLAP evolution equations [rif.] for the quark ($q_i(x, Q^2)$) and gluon ($g(x, Q^2)$) PDFs:

$$\frac{dq_i(x,Q^2)}{d\log Q^2} = \int_x^1 \frac{\mathrm{d}y}{y}\left(q_i(y,Q^2)P_{qq}\left(\alpha_s(Q^2),\frac{x}{y}\right) + g(y,Q^2)P_{qg}\left(\alpha_s(Q^2),\frac{x}{y}\right)\right) \tag{2.7}$$

$$\frac{dg(x,Q^2)}{d\log Q^2} = \int_x^1 \frac{\mathrm{d}y}{y}\left(\sum_i q_i(y,Q^2)P_{gq}\left(\alpha_s(Q^2),\frac{x}{y}\right) + g(y,Q^2)P_{gg}\left(\alpha_s(Q^2),\frac{x}{y}\right)\right) \tag{2.8}$$

where the sum $i = 1, ..., 2nf$ runs over quarks and antiquarks of all flaavours. The functions $P_{ab}(\alpha_s(Q^2), z)$ are called splitting functions and represent the probability

to find a parton a in a parton b at the scale Q^2 with a momentum fraction z. The splitting functions are calculable using a perturbative expansion in α_s. The diagrams contributing to the leading order splitting functions are shown in figure 2.3

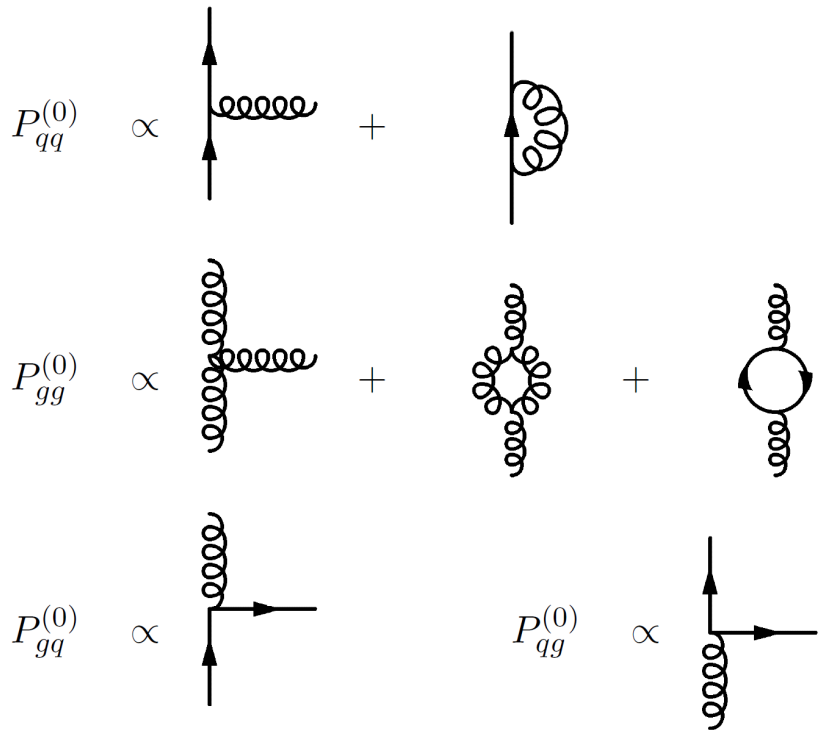

Figure 2.3: Feynman diagrams contributing to the leading order splitting functions.

In practice the PDFs used for calculations in the LHC energy regime are obtained by evolving the PDFs measured in fixed target experiments and in electron-proton scattering at HERA. The standard procedure is to first parametrize the x dependence of the PDFs at afixed input scale Q_0^2 and then extrapolate the function to the desired scale Q^2 according to the DGLAP equations. Several groups have performed PDF fits to the data obtained in DIS experiments, for example the CTEQ [21], MRST [**?**], MSTW [23] and NNPDF [24, 25] groups. The quark and gluon distribution functions measured at HERA at $Q^2 = 10$ GeV are shown in figure 2.4.

2.2.2 Heavy Quark Production

The leading-order (LO) process for the production of a heavy quark Q with mass m_Q in hadronic collisions is flaavour creation, i.e. quark-antiquark annihilation and gluon-gluon fusion

$$q\bar{q} \to Q\bar{Q} \quad \text{and} \quad gg \to Q\bar{Q} \tag{2.9}$$

The corresponding diagrams are shown in figure 2.5. When evaluating these diagrams and integrating over the two-body phase space the total partonic cross

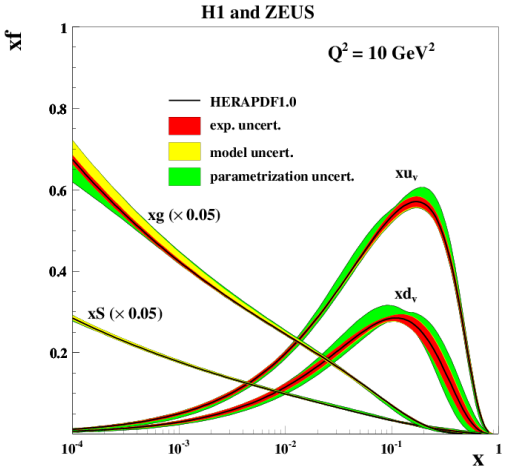

Figure 2.4: The proton parton distribution functions measured at HERA at $Q^2 = 10$ GeV, for valence quarks xu_v and xd_v, sea quarks xS, and gluons xg. The gluon and sea distributions are scaled down by a factor 20.

section at LO in perturbation theory can be obtained [26, 27, 28]. The large energy limit of the partonic cross section is

$$\hat{\sigma}(q\bar{q} \to Q\bar{Q}) \to \frac{1}{\hat{s}} \tag{2.10}$$

$$\hat{\sigma}(gg \to Q\bar{Q}) \to \frac{1}{\hat{s}} \left(\frac{1}{\beta} \log \left(\frac{1+\beta}{1-\beta} - 2 \right) \right) \tag{2.11}$$

where $\hat{s}$ is the center-of-mass energy available in the partonic system and $\beta \equiv \sqrt{1 - \frac{4m_Q^2}{\hat{s}}}$ is the velocity of the heavy quark. The quark annihilation process vanishes more quickly at high $\hat{s}$ thus gluon-gluon fusion is the dominant process for heavy quark production at the LHC. In flavour creation processes, the final states involving the heavy quarks are observed back-to-back with little combined transverse momentum.

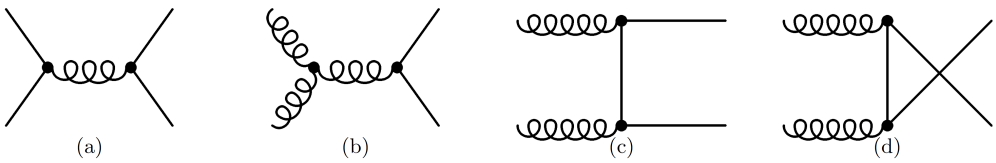

Figure 2.5: Leading order diagrams for heavy-quark pair production: (a) quark-antiquark annihilation $q\bar{q} \to Q\bar{Q}$, (b)-(d) gluon-gluon fusion $gg \to Q\bar{Q}$.

At next-to-leading order (NLO), contributions of real and virtual emission diagrams have to be taken into account. In addition, heavy quarks can be produced in flavour excitation processes and gluon splitting events (figure 2.6). In the flavour excitation process, the heavy quark is considered to be already present in the incoming hadron. It is excited by the exchange of a gluon with the other hadron and appears on mass-shell in the final state. Since the heavy quark is not a valence quark it must originate from a pair production process $g \to Q\bar{Q}$. In most

PDF parametrizations the heavy-flavour contributions are assumed to vanish for $Q^2 < m_Q^2$, the hard scattering in flavour excitation processes must therefore have a virtuality above m_Q^2. The heavy quark final states do not need to be back-to-back as the third parton can carry away some transverse momentum.

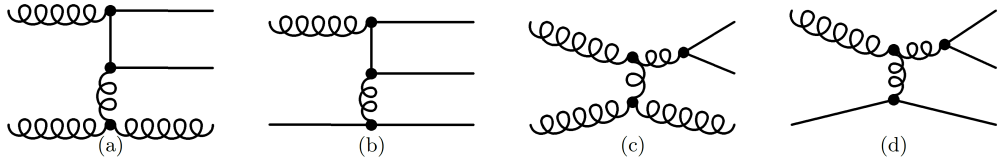

Figure 2.6: Next-to-leading order diagrams for heavy-quark pair production: (a),(b) flavor excitation; (c),(d) gluon splitting.

In gluon splitting events the heavy quark occurs in $g \to Q\bar{Q}$ events in the initial- or final-state shower. The resulting heavy flavoured final state can carry a large combined transverse momentum and thus be concentrated within a small cone of angular separation. The contribution of the different processes to the total b-quark production cross section predicted by PYTHIA (see section 3.4) is shown in figure 2.7 as a function of the center of mass energy.

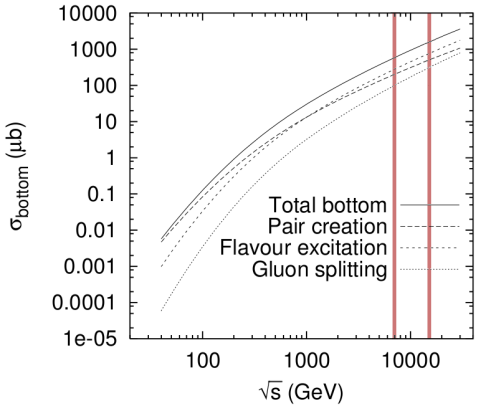

Figure 2.7: Total b cross-section as a function of the center-of-mass energy $\sqrt{s}$ in proton-protoncollisions. The contribution from pair production, flavor excitation and gluon splitting are shown. Vertical lines indicate 7 and 14 TeV in center of mass energy.

2.2.3 Semileptonic Decays of Heavy Quarks

The presence of hadrons containing heavy quarks is deduced by the observation of their decay products. In a first approximation of b-flavoured hadron decays, only the beauty quark participates in the transition while the other quark acts as a spectator quark. The b quark can decay via the weak interaction into a c- or a u-quark. The charged current couplings for the flaavour-changing transition between quarks are described in terms of the Cabibbo-Kobayashi-Maskawa (CKM) matrix given by

$$V_{CKM} = \begin{pmatrix} V_{ud} & V_{us} & V_{ub} \\ V_{cd} & V_{cs} & V_{cb} \\ V_{td} & V_{ts} & V_{tb} \end{pmatrix}. \tag{2.12}$$

The universality of the weak decay is reflected in the unitarity of the CKM matrix. Hence, the CKM matrix can be parametrized by three mixing angles and one irreducible phase which accounts for the CP-violation intrinsic to the weak decay in the Standard Model. The decay width is proportional to the squared CKM matrix element. Measurements of semileptonic decays of B mesons have shown that the matrix elements relevant for the weak decay of the b quark are very small compared to other elements: $|V_{cb}| = 0.0412 \pm 0.0011$ and $|V_{ub}| = 0.00393 \pm 0.00036$ [29]. Consequently, the b quark decay is highly suppressed and the b quark has a relatively large lifetime of $\tau \sim 10^{-12}$ s. Since $|V_{cb}|$ is about an order of magnitude larger than $|V_{ub}|$ the preferred decay is $b \to cW^-$ with a branching ratio of almost 100 %.

The lifetime $\tau$of a b-hadron is related to the decay length l by

$$l = \frac{p_B}{m_B} c\tau = \beta\gamma c\tau, \tag{2.13}$$

where p_B, m_B and $\beta\gamma$ are the particle's momentum, mass and boost, respectively. The distance of closest approach of the extrapolated muon track to the interaction point is defined as impact parameter d:

$$d = l \sin\delta = \beta\gamma c\tau \sin\delta, \tag{2.14}$$

where δ is the angle between the direction of the secondary track and the direction of the parent particle. Objects originating from a secondary vertex are generally characterized by a large transverse impact parameter (figure 2.8). The transverse impact parameter is then defined as

$$d_{xy} = d \sin\theta = \beta\gamma c\tau \sin\delta \sin\theta, \tag{2.15}$$

where θ is the polar angle between the hadron direction and the beam axis.

Properties of b-hadrons are listed in Table 2.4. Their mean decay length is c =466 μm. This transforms into an average observable decay length of $L = \beta\gamma c\tau$ =3$\div$5 mm in the rest frame at the LHC which can be observed as a displaced (or secondary) vertex in the detector. In CMS a lifetime based tag of b-hadrons is possible thanks to the pixel detector which achieves a track impact parameter resolution of about 20 μm. For comparison, also the properties of c-hadrons are listed in Table 2.4.

The W boson originating from the weak decay of the b-quark decays either hadronically or leptonically. Within this analysis the semileptonic decay of b quarks into muons is studied since the muon provides a clean signature which is relatively easy to detect experimentally. The decay $W^- \to \mu^- \bar{\nu}_\mu$ has a branching ratio of about 10%. In addition, about 10% of the subsequent charm decays also have a muon and a neutrino in the final state. The Feynman diagrams of the semileptonic decay of a b-hadron with a muon in the final state are illustrated in figure 2.9.

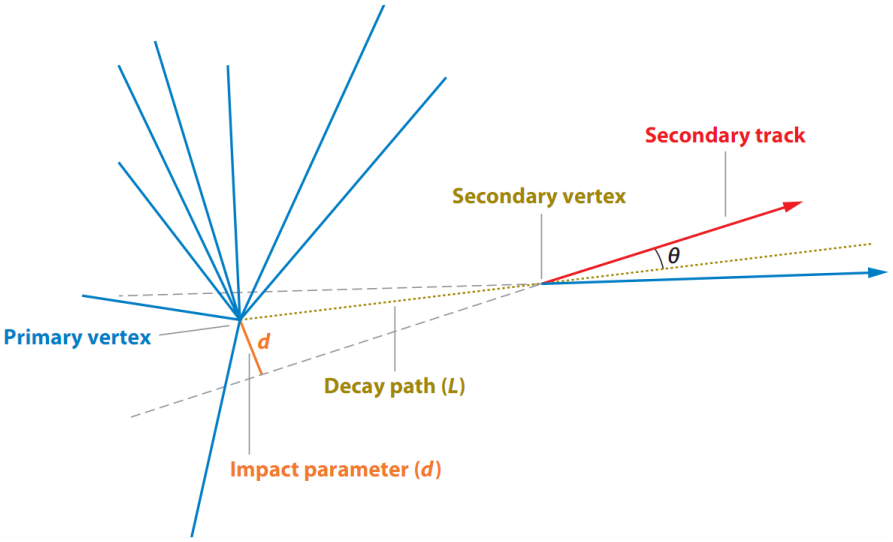

Figure 2.8: Illustration of the transverse impact parameter d of the decay products of a long-lived particle. The decay particles emerging from the secondary vertex are characterized by a large transverse impact parameter compared to that of the particles emerging from the primary vertex.

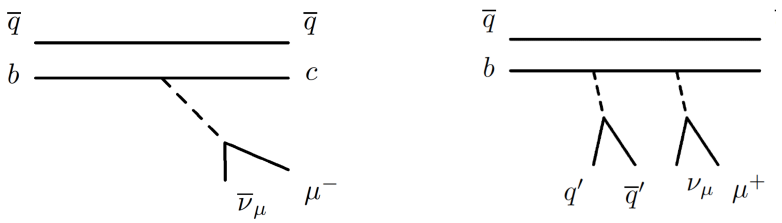

Figure 2.9: Weak decay of b-hadrons with a muon in the final state.

	quark content	mass m [MeV]	lifetime τ [ps]	decay length $c\tau$ [μm]	fraction
B^0	db	5279.50 ± 0.30	1.518 ± 0.007	455.1	0.403 ± 0.009
B^+	$u\bar{b}$	5279.17 ± 0.29	1.641 ± 0.008	492.0	0.403 ± 0.009
B_s^0	$s\bar{b}$	5366.3 ± 0.6	1.477 ± 0.022	442.8	0.103 ± 0.009
Λ_b^0	ubd	5620.2 ± 1.6	1.425 ± 0.032	427.2	0.090 ± 0.015
D^0	$c\bar{u}$	1864.80 ± 0.14	0.415 ± 0.004	124.4	0.557 ± 0.053
D^+	$c\bar{d}$	1869.57 ± 0.16	1.057 ± 0.015	316.9	0.233 ± 0.027
D_s^+	$c\bar{s}$	1968.45 ± 0.33	0.467 ± 0.017	140.0	0.103 ± 0.029
Λ_c^0	udc	2286.2 ± 1.6	0.206 ± 0.012	61.8	0.08 ± 0.05

Table 2.4: Properties of b- and c-hadrons. The table shows the quark content, the mass, the lifetime and the decay length [29].

2.3 B-mixing

Quantum mechanics and the structure of the weak interaction permit to few neutral mesons to change from their particle to their antiparticle. In 1955 Gell-Mann and Pais predicted the oscillations of neutral strange mesons and Lande at Brookhaven confirmed this prediction through the observation of two strange neutral particles with different life time and masses. The only hadrons that can undergo these oscillation are K^0, D^0, B^0 and B_s^0. Since this analysis deals with the B mixing all the formalism is presented in terms of b quarks coupled with d, s quarks, though it was first derived for the kaon system. In the following notation B is used to mean either B^0 and B_s^0 when a results is valid for both. In figure 2.10 box diagrams for B-mixing.

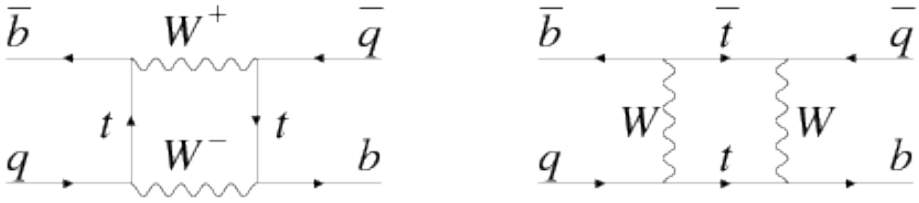

Figure 2.10: Dominant box diagrams for the $B_q^0 \to \bar{B}_q^0$ transitions ($q = d$ or s). Similar diagrams exist where one or both t quarks are replaced with c or u quarks.

2.3.1 Mixing formalism

The oscillation effect follows from a perturbative solution to Schodinger's equation. The strong interaction creates two stable states

$$|B\rangle = |\bar{b}q\rangle \tag{2.16}$$

$$|\bar{B}\rangle = |b\bar{q}\rangle \tag{2.17}$$

where $q = d, s$, that are *eigenstates* of non perturbative Hamiltonian $\mathcal{H}$

$$\mathcal{H} = \begin{pmatrix} m_0 & 0 \\ 0 & m_0 \end{pmatrix}, \tag{2.18}$$

where the masses $m_B = m_{\bar{B}} = m_0$ are equal because of the CPT symmetry.
When the weak interaction is added also the decays, must be considered. A consequence of this is that the matrix elements between the two states and a continuum states become different from zero. The continuum state can be split up in three groups:

1. States $|\alpha\rangle$ accessible only to $|B\rangle$. This means that there are not possibility for $|\bar{B}\rangle$ to decay in this states: $\langle\alpha|\mathcal{H}_W\bar{B}\rangle$.

2. States $|\beta\rangle$ accessible only to $|\bar{B}\rangle$, that is states in which $|B\rangle$ can not decay.

3. States accessible from decays of both $|B\rangle$ and $|\bar{B}\rangle$.

In addition the two discrete states are connected by a direct matrix element $W_{12} = \langle B|\mathcal{H}_W\bar{B}\rangle$ or via off-shell continuum states accessible to both. The introduction of continuum states has several effects:

1. The masses of both states $|B\rangle$ and $|\bar{B}\rangle$ is shifted by δE, such that they become $M = m_0 + \delta E$.

2. The possible interactions between the two states through off-shell continuum states accessible to both or via $\mathcal{H}_W$ products a non diagonal elements in the real part of the Hamiltonian different to zero.

3. The decays introduce an imaginary part to $\mathcal{H}$ that is connected with the on-shell decays unique to each (Γ) and with continuum states common to both (Γ_{12}).

Now the complete Hamiltonian $\mathcal{H} = \mathcal{H} + \mathcal{H}_W$ has infinite dimensions. Even if this matrix is not Hermitian it can be referred to as a Hamiltonian and can be derived as follows:

$$\mathcal{H} = \begin{pmatrix} m_0 + \delta E & W_{12} + \delta E_{12} \\ W_{12}^* + \delta E_{12}^* & m_0 + \delta E \end{pmatrix} - \frac{i}{2}\begin{pmatrix} \Gamma & W_{12} + \Gamma_{12} \\ \Gamma_{12}^* & \Gamma \end{pmatrix}. \tag{2.19}$$

The eigenstates and the eigenvalues can be find diagonalising this matrix. The difference of masses between the two eigenstates leads the notation to be H and L, respectively for the Heavy and the Light eigenstate. The eigenstates of the Hamiltonian are

$$|B_L\rangle = p|B\rangle + q|\bar{B}\rangle \tag{2.20}$$
$$|B_H\rangle = p|B\rangle - q|\bar{B}\rangle \tag{2.21}$$

where p and q are two complex number, and the eigenvalues are

$$\lambda_{H,L} = m_{H,L} - \frac{i}{2}\,\Gamma_{H,L} \tag{2.22}$$

The masses and the widths of these states are

$$m_{H,L} = M \pm \Re e\ y \equiv M \pm \Delta m/2 \tag{2.23}$$

$$\Gamma_{H,L} = \Gamma \pm 2\ \Im m\ y \equiv \Gamma \pm \Delta\Gamma/2 \tag{2.24}$$

where

$$y = \sqrt{|M_{12}|^2 - \frac{|\Gamma_{12}|^2}{4} - i\ \Re e(M_{12}\Gamma_1 2^*)}. \tag{2.25}$$

So we have a mass difference $\Delta m = m_H - m_L > 0$ and a total decay width difference $\Delta\Gamma = \Gamma_L - \Gamma_H$. In the absence of CP violation in the mixing we have $|q/p| = 1$. Moreover the lifetime difference $\Delta\Gamma$ between $|B_L\rangle$ and $|B_H\rangle$ is so small that can be neglected.

The time evolution of a state which was a pure $|B\rangle$ at $t = 0$ expressed in terms of flavour eigenstates can be obtained through the simple time dependence $|B_{L,H}(t)\rangle = e^{-i\lambda_{L,H}t}\ |B_{L,H}(t=0)\rangle$. So we get

$$|B(t)\rangle = \frac{|B_L(t)\rangle + |B_H(t)\rangle}{\sqrt{2}} \tag{2.26}$$

$$= e^{-i\Delta m t - \frac{\Gamma}{2}t} \cdot [\cos(\Delta m\ t)|B\rangle + i \sin(\Delta m\ t)|\bar{B}\rangle]. \tag{2.27}$$

The probability to find a B or a $\bar{B}$ after t seconds from its creation is

$$P_u(t) = \frac{|\langle B|B(t)\rangle|^2}{\int_0^\infty \langle B(t)|B(t)\rangle\ dt} \tag{2.28}$$

$$= \frac{\Gamma}{2} e^{-\Gamma/t} \cdot [1 + \cos^2(\Delta m\ t)], \tag{2.29}$$

$$P_m(t) = \frac{|\langle \bar{B}|B(t)\rangle|^2}{\int_0^\infty \langle B(t)|B(t)\rangle\ dt} \tag{2.30}$$

$$= \frac{\Gamma}{2} e^{-\Gamma/t} \cdot [1 - \cos^2(\Delta m\ t)], \tag{2.31}$$

where the index m indicates the *mixed* probability, that is the probability to find a final state different from the initial one. In the same way the index u means *unmixed*. The time-integrated versions expresses the probability that a B decays as a $\bar{B}$. Using the $\Delta\Gamma = 0$ approximation they can be written as follows:

$$\chi_d = \int_0^\infty P_m(t)\ dt = \frac{1}{2}\frac{x}{1+x^2} \tag{2.32}$$

$$\chi_s = \int_0^\infty P_m(t)\ dt = \frac{1}{2}\frac{x}{1+x^2} \tag{2.33}$$

where

$$x \equiv \frac{\Delta m}{\Gamma}. \tag{2.34}$$

A common variable used in hadron colliders, where both B^0 and B_s^0 can be produced, is the *average time-integrated mixing probability*

$$\bar{\chi} = f_d\chi_d + f_s\chi_s. \tag{2.35}$$

where f_d is the B^0 fraction in the b sample while f_s is the B_s^0 fraction.

2.3.2 Measurements of $\bar{\chi}$

As we have seen in the previous section, flavor changing neutral currents induce the flavor (F) transformation $\Delta F = 2$ of a neutral B-meson into its antiparticle and viceversa. In the standard model this phenomenon is described by box diagrams involving the exchange of two up-like quarks (mostly top) and two W bosons (figure 2.10).

Precise measurements of the flavor oscillation frequencies, $\Delta m_d = 0.508 \pm 0.003$ (stat) ± 0.003 (syst) ps^{-1} and $\Delta m_s = 17.77 \pm 0.10$ (stat) ± 0.07 (syst) ps^{-1} have been performed for B^0 mesons by the B-factories, and for B_s mesons by the CDF collaboration. The corresponding time integrated mixing probabilities,

$$\chi_d = \frac{\Gamma(b \to B^0 \to \bar{B^0})}{\Gamma(b \to B^0)} = 0.1873 \pm 0.0024$$

and

$$\chi_s = 0.49927 \pm 0.00003$$

computed by integrating the functions describing the time dependent B-flavor oscillation, are known with astonishing precision.

We have defined the average time integrated mixing probability,

$$\bar{\chi} = \frac{\Gamma(b \to B \to \bar{B})}{\Gamma(b \to B)} = f_d \chi_d + f_s \chi_s$$

where charge conjugate processes are always implied. Here f_d and f_s are the fractions of B^0 and B_s mesons in an unbiased sample of weakly decaying b-hadrons. The measurement of $\bar{\chi}$ provides therefore a constraint on the values of f_d and f_s. Uncertainties on the b-sample composition are among the largest sources of systematic errors in the measurements of b-hadrons branching fractions at LHC.

Experimentally, $\bar{\chi}$ is measured by comparing the rates of events with two equal or opposite charge leptons from the semileptonic decay $B \to \ell^+ \nu_\ell X$. Same-charge events occur when one, and one only, of the two B-hadrons produced undergoes mixing (hereafter, mixed events). Opposite-charge leptons (hereafter, unmixed) are observed when either none or both the mesons have oscillated. Precise measurements of $\bar{\chi}$ have been performed by the LEP collaborations in e^+e^- collisions at $\sqrt{s} = 91$ GeV. The LEP average $\bar{\chi} = 0.126 \pm 0.004$ is still the most precise determination of $\bar{\chi}$. The latest CDF result $\bar{\chi} = 0.126 \pm 0.008$ is well consistent with the LEP value, conferming the hypothesis that B-hadrons are produced in equal proportions in e^+e^- and $p\bar{p}$ colliders. It should be noted that, to derive this result, a sizable fraction of the CDF dimuon sample is assigned to an unknown origin, not explained by standard model source .

It is not expected a priori that the B-hadron sample composition at the LHC be the same as at LEP or Tevatron, because the initial state in a pp collision is not flavor symmetric, with four valence u-quarks and two valence d-quarks. The LHCb collaboration has measured the composition of the B-hadron mixture by comparing the event rates in fully reconstructed final states. These measurements are however performed in a different kinematical domain, and are intrinsically limited by the knowledge of the branching ratios of the reference B decays. A measurement

of $\bar{\chi}$ at CMS allows therefore a comparison with the results obtained at flavor symmetric colliders or in a different kinematic range at LHC. Besides increasing our understanding of the $b \to B$ fragmentation process, this helps improving the measurements of rare B decays from the LHC experiments.

Chapter 3

The CERN Large Hadron Collider and the Compact Muon Solenoid Experiment

The Large Hadron Collider (LHC) [30] is an accelerator located at the European Laboratory for Particle Physics Research (CERN) in Geneva. It has been conceived to collide proton beams at a center-of-mass energy of $\sqrt{s} = 14$ TeV and a nominal instantaneous luminosity of $\mathcal{L} = 10^{34}$ cm^{-2} s^{-1}, representing a seven-fold increase in energy and a hundred-fold increase in integrated luminosity over the previous hadron collider experiments. Its main purpose is to search for rare processes like the production of Higgs or new particles with mass of 1 TeV and beyond. Two experiments have been installed around the LHC to pursue these results: ATLAS [31] and CMS [32]. Furthermore, the LHCb [33] experiment studies the properties of charm and beauty hadrons produced with large cross sections in asymmetric collisions at the LHC, and the ALICE [34] experiment will analize the data from relativistic heavy ion collisions to study the hadronic matter in extreme temperature and density conditions (i.e. high quark-gluon density).

3.1 The Large Hadron Collider

The LHC has been installed in the same tunnel which hosted the e^+e^- collider LEP (Large Electron Positron). Accelerated electrons and positrons suffer large energy loss due to the synchrotron radiation, which is proportional to $E^4/(Rm^4)$, where E is the electron energy, m its mass and R the accelerator radius. To obtain energies of the order of TeV, at the fixed accelerator radius, only massive charged particles could have been used: protons and heavy nuclei. The energy loss is reduced by a factor $(2000)^4$ for a given fixed energy E if we consider protons.
Another important aspect of the LHC is the collision rate. To produce a sufficient number of rare processes, the collision rate needs to be very high. Beam protons are collected in packets called bunches. The collision rate is proportional to the

instantaneous luminosity of the accelerator, defined as:

$$\mathcal{L} = \frac{f k n_p^2}{4\pi\sigma_x\sigma_y}, \tag{3.1}$$

where f is the bunch revolution frequency, k the number of bunches, n_p the number of protons per bunch and σ_x, σ_y their transverse dispersion along the x and y axis. At the nominal 14 TeV LHC conditions ($\mathcal{L} = 10^{34}$ cm^{-2}s^{-1}) the parameter values are: $k = 2808$, $n_p = 1.5 \times 10^{11}$ and $\sigma_x\sigma_y = 16.6$ μm (with $\sigma_z = 7.6$ cm along the beam). The integrated luminosity is defined as $L = \int \mathcal{L} dt$. For comparison we can consider the Tevatron accelerator at Fermilab, which produced proton-antiproton collisions since 1992. Its energy was 1.8 TeV up to 1998 and 1.96 TeV since 2001. To increase $\mathcal{L}$ by two orders of magnitude, protons are injected in both LHC beams instead of antiprotons. The latters, in fact, are obtained by steering proton beams onto a nickel target and represent only a small fraction of the wide range of secondary particles produced in this interactions.

The LHC is constituted by 1232 super-conducting dipole magnets each 15 m long, delivering a 8.3 T magnetic field to let the beams circulate inside their trajectories along the 27 km circumference. Two vacuum pipes are utilized to let beams circulate in opposite directions. A scheme representing the transverse dipole magnet section is represented in Fig. 3.1. More than 8000 other magnets are utilized

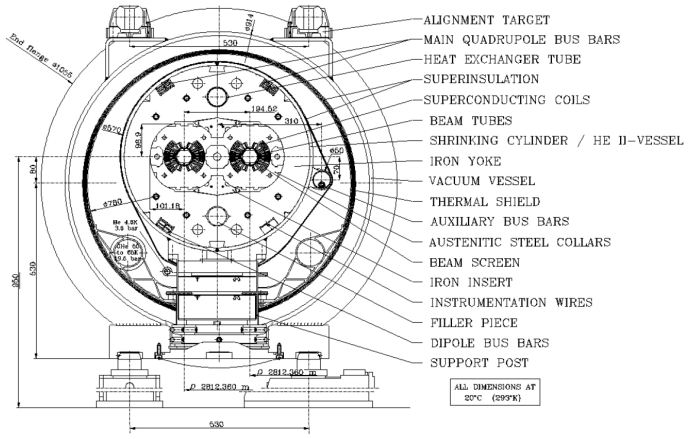

Figure 3.1: LHC dipole magnet section scheme. Figure from [30].

for the beam injection, their collimation, trajectory correction, crossing. All the magnets are kept cool by superfluid helium at 1.9 K temperature.
The beams are accelerated from 450 GeV (the injection energy from the SPS) to 7 TeV with 16 Radio Frequency cavities (8 per beam) which raise the beam energy by 16 MeV each round with an electric field of 5 MV/m oscillating at 400 MHz frequency.
Before the injection into the LHC, the beams are produced and accelerated by different components of the CERN accelerator complex. Being produced from ionized hydrogen atoms, protons are accelerated by the linear accelerator LINAC, Booster and the Proton Synchrotron (PS) up to 26 GeV energy, the bunches being

separated by 25 ns each. The beams are then injected into the Super Proton Synchrotron (SPS) where they are accelerated up to 450 GeV. They are then finally transferred to the LHC and accelerated up to 7 TeV energy per beam. The CERN accelerator complex is illustrated in Fig. 3.2.

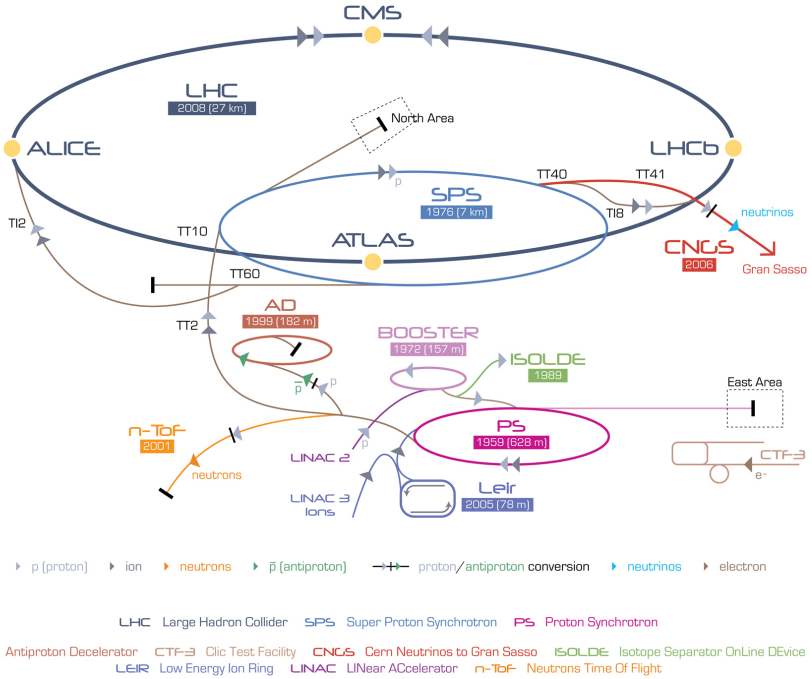

Figure 3.2: Scheme representing the CERN accelerator complex.

The LHC started its operations in December 2009 with center of mass energy $\sqrt{s} = 0.9$ TeV. The center of mass energy was set to $\sqrt{s} = 7$ TeV in 2010, and the performance during 2010 and 2011 raised impressively. In 2010 the peak luminosity reached $\mathcal{L} = 2 \times 10^{32}$ cm^{-2}s^{-1} (200 μb^{-1}s^{-1}, with 368 bunches) and during 2011 increased by a factor 10 in up to $\mathcal{L} = 3.5 \times 10^{33}$ cm^{-2}s^{-1} (3.5 nb^{-1}s^{-1}, with 1380 bunches). The integrated luminosity in 2010 has been $\mathcal{L} = 40$ pb^{-1}, while in 2011 it increased by a factor 100 up to ~ 5 fb^{-1}, as graphically summarized in Fig. 3.3. In 2012 the machine is operated at a center of mass energy $\sqrt{s} = 8$ TeV and increasing instant luminosity. So far ~ 7 fb^{-1} have been collected.

3.2 Constraints on the Design of the CMS Experiment

We can briefly summarize the aims of the CMS detector [36, 37]. They are mainly:

- search for SM and MSSM Higgs boson decaying into photons, b quarks, τ leptons, W and Z bosons,
- search for additional heavy neutral gauge bosons predicted in many superstring-inspired theories or Great Unification theories and decaying to muon pairs,
- search for $B_0 \to \mu^+\mu^-$ decays,

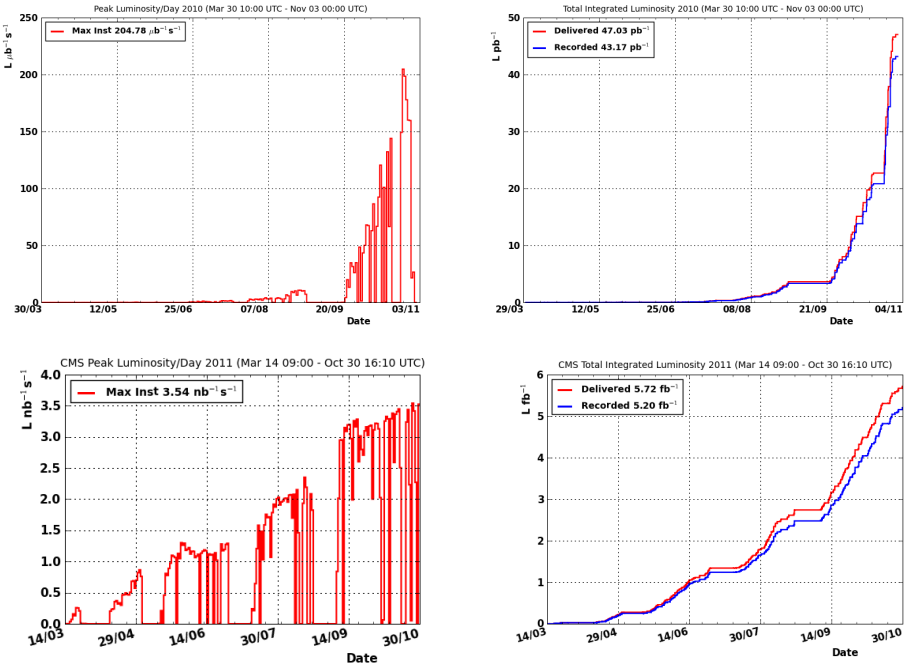

Figure 3.3: LHC performance in 2010 (top) and 2011 (bottom). Left: LHC peak luminosity; right: LHC integrated luminosity. Figures from [35].

- search for new Physics in various topologies: multilepton events, multijet events, events with missing transverse energy or momentum, any combination of the three above [1],
- study of the violation of the CP symmetry in the decay of the B_s^0 meson into $J/\psi\ \phi \to \mu^+\mu^+K^+K^-$,
- study of QCD and jet physics at the TeV scale,
- study of top quark and EW physics.

CMS has been therefore designed as a multipurpose experiment, with particular focus on muon ($H \to ZZ \to 4\mu$), photon ($H \to \gamma\gamma$), and displaced tracks reconstruction. Superb performances have been achieved overall, in particular in:

1. primary and secondary vertex localization
2. charged particle momentum resolution and reconstruction efficiency in the tracking volume
3. electromagnetic energy resolution
4. isolation of leptons and photons at high luminosities

[1] Missing transverse energy $\not\!\!E_T$ is the amount of energy which must be added to balance the modulus of the vector sum of the projections of the track momenta and calorimeter clusters in the plane perpendicular to beam axis.

5. measurement of the direction of photons, rejection of $\pi^0 \to \gamma\gamma$
6. diphoton and dielectron mass resolution $\sim 1\%$ at 100 GeV
7. measurement of the missing transverse energy $\not{E}_T$ and dijet mass with high resolution
8. muon identification over a wide range of momenta
9. dimuon mass resolution $\sim 1\%$ at 100 GeV
10. unambiguously determining the charge of muons with p_T up to 1 TeV
11. triggering and offline tagging of τ leptons and b jets

3.3 The CMS Experiment

The Compact Muon Solenoid [32] is a general purpose detector situated at interaction region 5 of the CERN Large Hadron Collider. It is designed around a 4 T solenoidal magnetic field provided by the largest superconducting solenoid ever built. The structure of CMS is shown in Fig. 3.4, where particular emphasis is put on the volumes of the different subsystems: the Silicon Pixel Detector, the Silicon Strip Tracker, the Electromagnetic and Hadronic Calorimeters, and Muon Detectors.

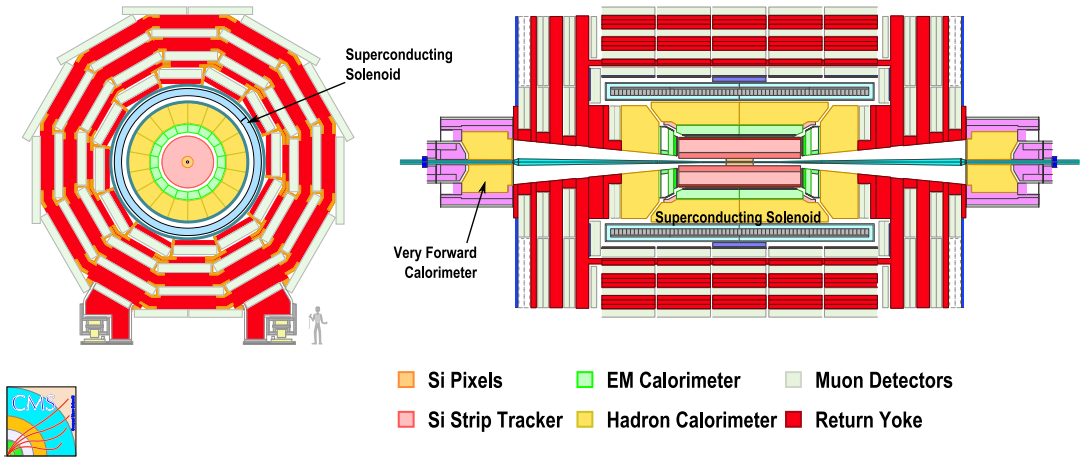

Figure 3.4: Transverse (left) and longitudinal (right) cross sections of the Compact Muon Solenoid detector showing the volumes of the different detector subsystems. The transverse cross section is drawn for the central barrel, coaxial with the beam line, while complementary end-caps are shown in the longitudinal view.

The reference frame used to describe the CMS detector and the collected events has its origin in the geometrical center of the solenoid. It is embedded with different types of global coordinates measured with respect to the origin[2]:

[2]Global coordinates are measured in the CMS reference frame while local coordinates are measured in the reference frame of a specific sub-detector or sensitive element.

- Cartesian coordinate system – $\hat{x}$ axis points towards the center of the LHC, $\hat{y}$ points upwards, perpendicular to the LHC plane, while $\hat{z}$ completes the right-handed reference, pointing along the beamline directed towards the Jura mountains
- polar coordinate system – directions are defined with an azimuthal angle $\tan\phi = y/x$ and a polar angle $\tan\theta = \rho/z$, where $\rho^2 = x^2 + y^2$
- from hte polar angle the rapidity y and pseudorapidity η are obtained for any particle

$$y = \frac{1}{2}\ln\left(\frac{E + p_z}{E - p_z}\right) \tag{3.2}$$

$$\eta = -\ln\left(\tan\frac{\theta}{2}\right) \tag{3.3}$$

where E is the particle energy and p_z the component of its momentum along the beam direction.

3.3.1 Magnet

The whole CMS detector is designed around a ~ 4 T superconducting solenoid [38] 12.5 m long and with inner radius of 3 m. The solenoid thickness is 3.9 radiation lengths and it can store up to 2.6 GJ of energy.

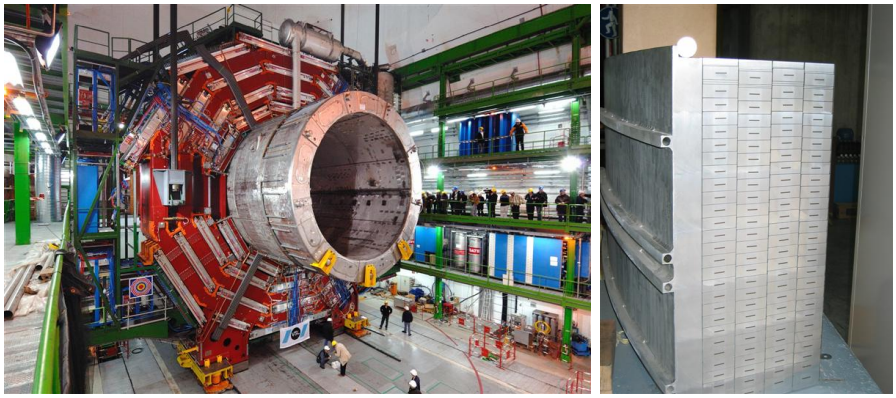

Figure 3.5: Left: CMS superconducting solenoid during assembly: the barrel return yokes are painted red. Muon detectors are already mounted and visible between return yoke layers. Right: cross section of the CMS magnet cables. Figures from [39].

The field is closed by a 10 000 t iron return yoke made of five barrels and two end-caps, composed of three layers each. The yoke is instrumented with four layers of muon stations. The coil is cooled down to 4.8 K by a helium refrigeration plant, while insulation is given by two pumping stations providing vacuum on the 40 m^3 of the cryostat volume.
The magnet was designed in order to reach precise measurement of muon momenta. A high magnetic field is required to keep a compact spectrometer capable

to measure 100 GeV track momentum with percent precision . A solenoidal field was chosen because it keeps the bending in the transverse plane, where an accuracy better than 20 μm is achieved in vertex position measurements. The size of the solenoid allows efficient track reconstruction up to a pseudorapidity of 2.4. The inner radius is large enough to accommodate both the Silicon Tracking System and the calorimeters. The magnet is currently operated at 3.8 T.

3.3.2 Tracking System

The core of CMS is a Silicon Tracking System [40, 41] with 2.5 m diameter and 5.8 m length, designed to provide a precise and efficient measurement of the trajectories of charged particles emerging from LHC collisions and reconstruction of secondary vertices.

The CMS Tracking System is composed of both silicon Pixel and Strip Detectors, as shown in Fig. 3.6. The Pixel Detector consists of 1440 pixel modules arranged in three barrel layers and two disks in each end-cap as in Fig. 3.7. The Strip detector consists of an inner tracker with four barrel layers and three end-cap disks and an outer tracker with six barrel layers and nine end-cap disks, housing a total amount of 15,148 strip modules of both single-sided and double-sided types. Its active silicon surface of about 200 m^2 makes the CMS tracker the largest silicon tracker ever built.

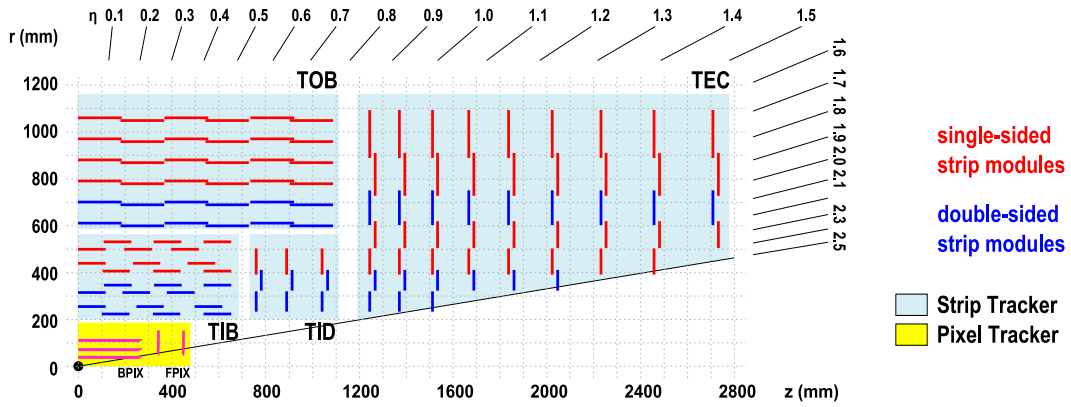

Figure 3.6: Layout of the CMS silicon tracker showing the relative position of hybrid pixels, single-sided strips and double-sided strips. Figure from [32].

The LHC physics programme requires high reliability, efficiency and precision in reconstructing the trajectories of charged particles with transverse momentum larger than 1 GeV in the pseudorapidity range $|\eta| < 2.5$. Heavy quark flavours can be produced in many of the interesting channels and a precise measurement of secondary vertices is therefore needed. The tracker completes the functionalities of ECAL and Muon System to identify electrons and muons. Also hadronic decays of tau leptons need robust tracking to be identified in both the one-prong and three-prongs topologies. Tracker information is heavily used in the High Level Trigger of CMS to help reducing the event collection rate from the 40 MHz of

bunch crossing to the 100 Hz of mass storage.

Silicon Pixel Detector

The large number of particles produced in 25 piled-up events, at nominal LHC luminosity, results into a hit rate density of 1 MHz/mm^2 at 4 cm from the beamline, decreasing down to 3 kHz/mm^2 at a radius of 115 cm. Pixel detectors are used at radii below 10 cm to keep the occupancy below 1%. The chosen size for pixels, 0.100×0.150 mm^2 in the transverse and longitudinal directions respectively, leads to an occupancy of the order of 10^{-4}. The layout of the Pixel Detector consists of a barrel region (BPIX), with three barrels at radii of 4.4, 7.3 and 10.2 cm, complemented by two disks on each side (FPIX), at 34.5 and 46.5 cm from the nominal interaction point. This layout provides about 66 million pixels covering a total area of about 1 m^2 and measuring three high precision points on each charged particle trajectory up to $|\eta| = 2.5$. Detectors in FPIX disks are tilted by 20° in a turbine-like geometry to induce charge sharing and achieve a spatial resolution of about 20 μm.

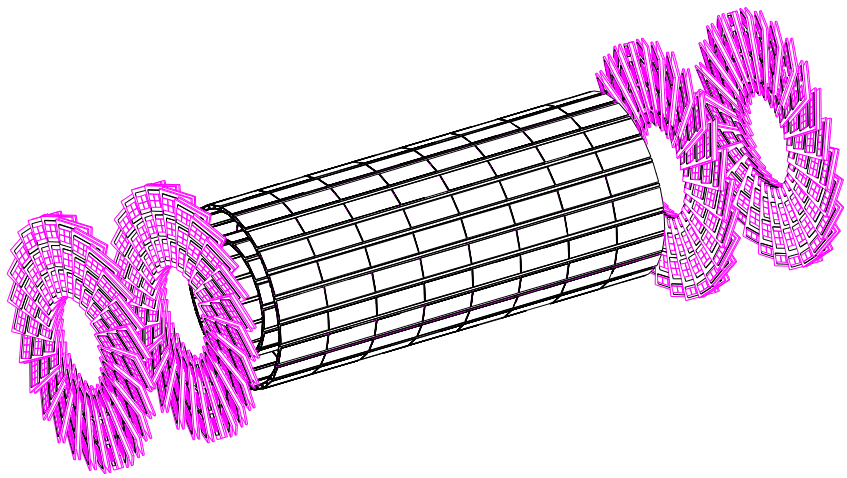

Figure 3.7: Layout of the current CMS Pixel Detector. Figure from [40].

Silicon Strip Tracker

In the inner Strip Tracker, which is housed between radii of 20 and 55 cm, the reduced particle flux allows a typical cell size of 0.080×100 mm^2, resulting in a 2% occupancy per strip at design luminosity. In the outer region, the strip pitch is increased to 0.180×250 mm^2 together with the sensor thickness which scales from 0.320 mm to 0.500 mm. This choice compensates the larger capacitance of the strip and the corresponding larger noise with the possibility to achieve a larger depletion of the sensitive volume and a higher charge signal.

The Tracker Inner Barrel and Disks (TIB and TID) deliver up to 4 r-ϕ measurements on a trajectory using 0.320 mm thick silicon strip sensors with strips parallel to the beamline. The strip pitch is 0.080 mm in the first two layers and 0.120 mm in the other two layers, while in the TID the mean pitch varies from 0.100 mm to 0.141 mm. Single point resolution in the TIB is 0.023 mm with the finer pitch and 0.035 mm with the coarser one. The Tracker Outer Barrel (TOB) surrounds the TIB/TID and provides up to 6 r-ϕ measurements on a trajectory using 0.500 mm thick sensors. The strip pitch varies from 0.183 mm in the four innermost layers to 0.122 mm in the outermost two layers, corresponding to a resolution of 0.053 mm and 0.035 mm respectively. Tracker End-Caps (TEC) enclose the previous sub-detectors at 124 cm $< |z| <$ 282 cm with 9 disks carrying 7 rings of microstrips, 4 of them are 0.320 mm thick while the remaining 3 are 0.500 mm thick. TEC strips are radially oriented and their pitch varies from 0.097 mm to 0.184 mm.

As shown in Fig. 3.6, the first two layers and rings of TIB, TID and TOB, as well as three out of the TEC rings, carry strips on both sides with a stereo angle of 100 milliradians to measure the other coordinate: z in barrels and r in rings. This layout ensures 9 hits in the silicon Strip Tracker in the full acceptance range $|\eta| < 2.4$, and at least four of them are two-dimensional. The total area of Strip Tracker is about 198 m^2 read out by 9.3 million channels.

Trajectory Reconstruction

Due to the magnetic field charged particles travel through the tracking detectors on a helical trajectory which is described by 5 parameters: the curvature κ, the track azimuthal angle ϕ and polar angle η, the signed transverse impact parameter d_0 and the longitudinal impact parameter z_0. The transverse (longitudinal) impact parameter of a track is defined as the transverse (longitudinal) distance of closest approach of the track to the primary vertex, as explained in Section **??**. The main standard algorithm used in CMS for track reconstruction is the Combinatorial Track Finder (CFT) algorithm [42] which uses the reconstructed positions of the passage of charged particles in the silicon detectors to determine the track parameters. The CFT algorithm proceeds in three stages: track seeding, track finding and track fitting. Track candidates are best seeded from hits in the pixel detector because of the low occupancy, the high efficiency and the unambiguous two-dimensional position information. The track finding stage is based on a standard Kalman filter pattern recognition approach [43] which starts with the seed parameters. The trajectory is extrapolated to the next tracker layer and compatible hits are assigned to the track on the basis of the χ^2 between the predicted and measured positions. At each stage the Kalman filter updates the track parameters with the new hits. In order to take into account possible inefficiencies one further candidate is created without including any hit information.

The tracks are assigned a quality based on the χ^2 and the number of missing hits and only the best quality tracks are kept for further propagation. Ambiguities between tracks are resolved during and after track finding. In case two tracks share

more than 50% of their hits, the lower quality track is discarded. For each trajectory the finding stage results in an estimate of the track parameters. However, since the full information is only available at the last hit and constraints applied during trajectory building can bias the estimate of the track parameters, all valid tracks are refitted with a standard Kalman filter and a second filter (smoother) running from the exterior towards the beam line. The expected performance of the track reconstruction is shown in Fig. 3.9 for muons, pions and hadrons. The track reconstruction efficiency for high energy muons is about 99% and drops at $|\eta| > 2.1$ due to the reduced coverage of the forward pixel detector. For pions and hadrons the efficiency is in general lower because of interactions with the material in the tracker.

The material budget is shown in Fig. 3.8 as a function of both pseudorapidity and different contributions of sub-detectors and services.

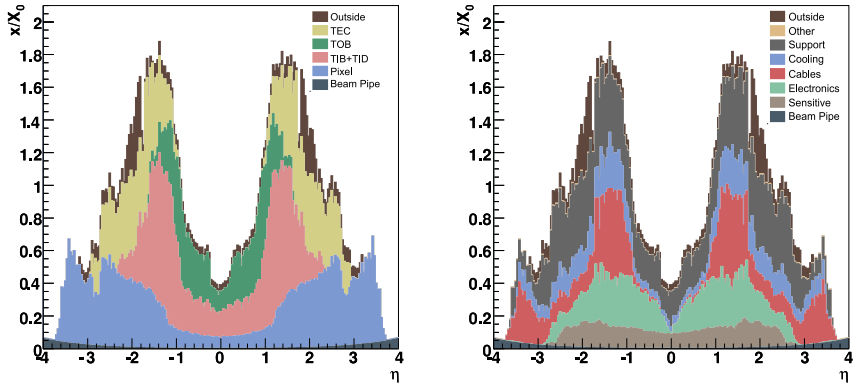

Figure 3.8: Material budget of the current CMS Tracker in units of radiation length X_0 as a function of the pseudorapidity, showing the different contribution of sub-detectors (left) and functionalities (right). Figures from [32].

The performance of the Silicon Tracker in terms of track reconstruction efficiency and resolution, of vertex and momentum measurement, are shown in Fig. 3.9 and 3.10 respectively. The first one, in particular, shows the difference in reconstruction efficiency for muons and pions, due to the larger interaction cross section of pions, which cannot be assumed to be minimum-ionizing particles and therefore are much more degraded by the amount of material.

Vertex Reconstruction The reconstruction of interaction vertices allows CMS to reject tracks coming from pile-up events. The primary vertex reconstruction is a two-step process. Firstly the reconstructed tracks are grouped in vertex candidates and their z coordinates at the beam closest approach point are evaluated, retaining only tracks with impact parameter less than 3 cm. Vertices are then reconstructed through a recursive method for parameter estimation through a Kalman filter [44] algorithm. For a given event, the primary vertices are ordered according to the total transverse momentum of the associated tracks, $\sum p_T$. The vertex reconstruction efficiency is very close to 100% and the position resolution is of the order of

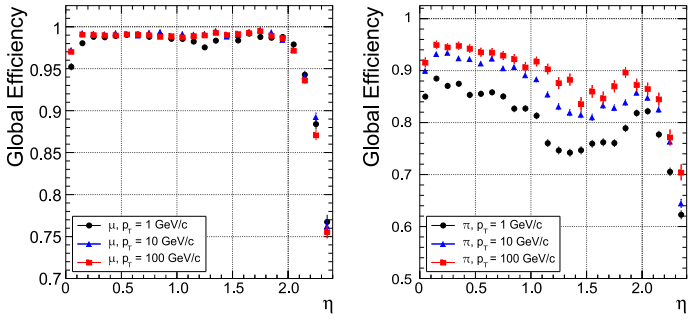

Figure 3.9: Global track reconstruction efficiency as a function of track pseudorapidity for muons (left) and pions (right) of transverse momenta of 1, 10 and 100 GeV. Figures from [32].

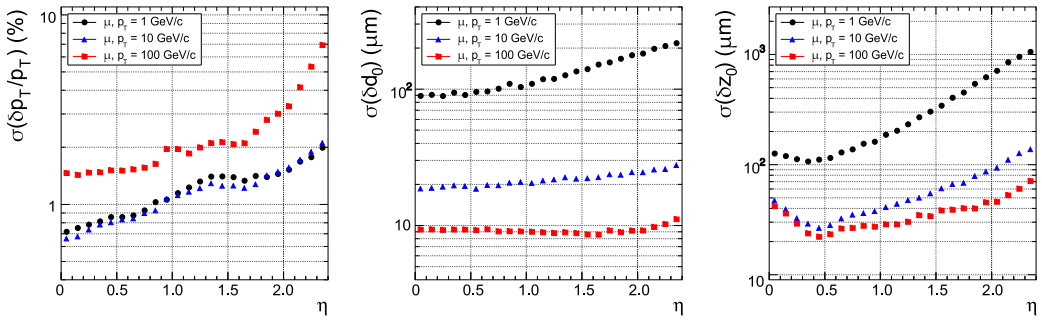

Figure 3.10: Resolution of several track parameters as a function of track pseudorapidity for single muons with transverse momenta of 1, 10 and 100 GeV: transverse momentum (left), transverse impact parameter (middle) and longitudinal impact parameter (right). Figures from [32].

$\mathcal{O}(10)$ μm in all directions.

It is also possible to reconstruct the secondary vertices, for example those from b-quark decays. The secondary vertex reconstruction uses tracks associated to jets applying further selection cuts: the transverse impact parameter of the tracks must be greater than 100 μm to avoid tracks coming from the primary vertex and below 2 cm to avoid tracks from pileup events.

3.3.3 Muon Spectrometer

Detection of muons at CMS exploits different technologies and is performed by a "Muon System" rather than a single detector [45]. Muons are the only particles able to reach the external muon chambers with a minimal energy loss when traversing the calorimeters, the solenoid and the B-field return yoke. Muons can provide strong indication of interesting signal events and are natural candidates for triggering purposes. The CMS Muon System was designed to cope with three major functions: robust and fast identification of muons, good resolution of mo-

mentum measurement and triggering.
The Muon System is composed of three types of gaseous detectors, located inside the empty volumes of the iron yoke, and therefore arranged in barrel and end-cap sections. The coverage of Muon System is shown in Fig. 3.11.

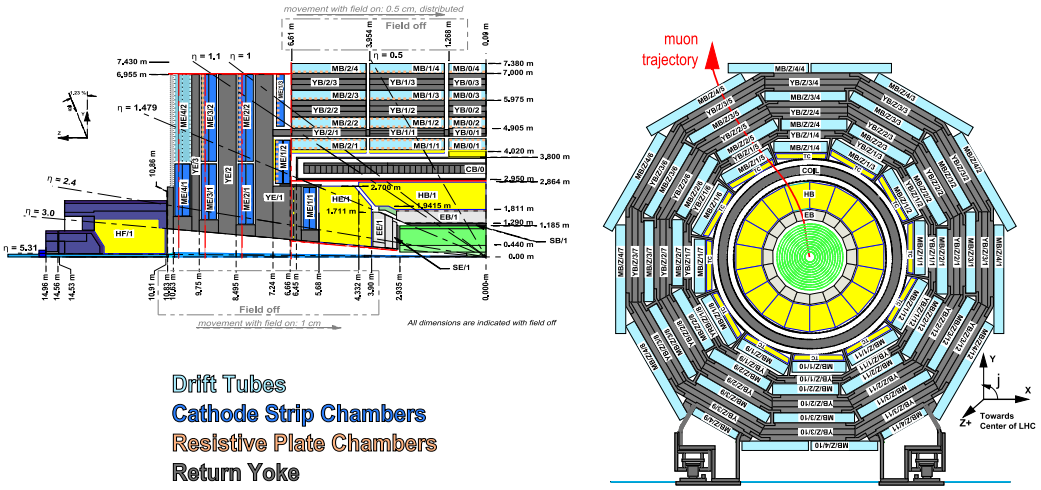

Figure 3.11: Transverse and longitudinal cross sections of the CMS detector showing the Muon System with particular emphasis on the different technologies used for detectors; the ME/4/2 CSC layers in the end-cap were included in the design but are not currently installed. Figures from [32].

In the barrel region the neutron-induced background is small and the muon rate is low; moreover, the field is uniform and contained in the yoke. For these reasons, standard drift chambers with rectangular cells are used. The barrel drift tubes (DT) cover the $|\eta| < 1.2$ region and are organized in four stations housed among the yoke layers. The first three stations contain 12 chambers, arranged in two layers providing measurement in the transverse plane and one layer measuring along z, each of them containing four chambers. The fourth station provides measurement only in the transverse plane. To eliminate dead spots in the efficiency and any left-right ambiguity, cells in consecutive layers are shifted by half of their width.

Both the muon rates and backgrounds are high in the forward region, where the magnetic field is large and non uniform. The choice for muon detectors fell upon cathode strip chambers (CSC) because of their fast response time, fine segmentation and radiation tolerance. Each end-cap is equipped with four stations of CSC's. The CSC's cover the $0.9 < |\eta| < 2.4$ pseudorapidity range. The cathode strips are oriented radially and provide precise measurement in the bending plane, the anode wires run approximately perpendicular to the strips and are read out to measure the pseudorapidity and the beam-crossing time of a muon. The muon reconstruction efficiency is typically 95-99% except for the regions between two barrel DT wheels or at the transition between DT's and CSC's, where the

efficiency drops.

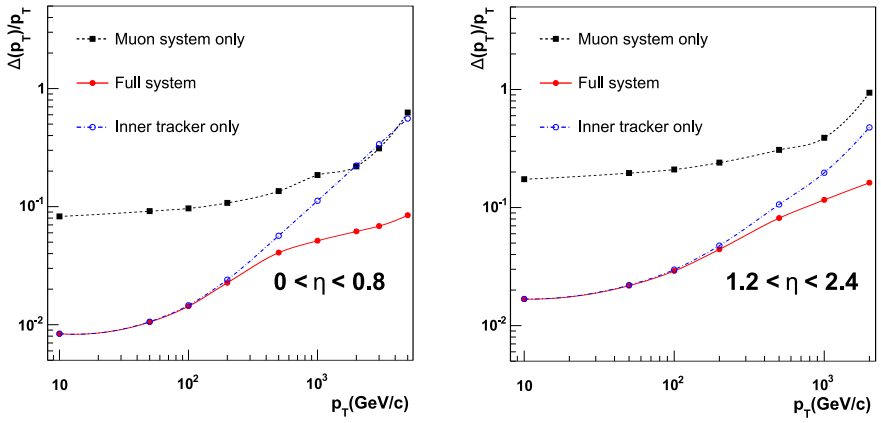

Figure 3.12: Resolution on p_T measurement of muons with the Muon System, the Silicon Tracker or both, in the barrel (left) and end-caps (right). Figures from [32].

Both the DT's and CSC's can trigger on muons with a Level 1 p_T resolution of 15% and 25%, respectively. Additional trigger-dedicated muon detectors were added to help measured the correct beam-crossing time. These are Resistive Plate Chambers (RPC), gaseous detector operated in the avalanche mode, which can provide independent and fast trigger with high segmentation and sharp p_T threshold over a large portion of the pseudorapidity range. The overall p_T resolution on muons is shown in Fig. 3.12, with emphasis on the different contribution from the Muon System and the Silicon Tracker.

Muon Reconstruction

Muon detection and reconstruction play a key role in the CMS physics program, both for the discovery of New Physics and for precision measurements of SM processes. CMS has been designed for a robust detection of muons over the entire kinematic range of the LHC and in a condition of very high background. The muon system allows an efficient and pure identification of muons, while the inner tracker provides a very precise measurement of their properties. An excellent muon momentum resolution is made possible by the high-field solenoidal magnet. The steel flux return yoke provides additional bending power in the spectrometer, and serves as hadron absorber to facilitate the muon identification. Several muon reconstruction strategies are available in CMS, in order to fulfill the specific needs of different analyses. The muon reconstruction consists of three main stages:

1. local reconstruction: in each muon chamber, the raw data from the detector read-out are reconstructed as individual points in space; in CSC and DT chambers, such points are then fitted to track stubs (*segments*);

2. stand-alone reconstruction: points and segments in the muon spectrometer are collected and fitted to tracks, referred to as "stand-alone muon tracks";

3. global reconstruction: stand-alone tracks are matched to compatible tracks in the inner tracker and a global fit is performed using the whole set of available measurements: the resulting tracks are called "global muon tracks".

Muon identification represents a complementary approach with respect to global reconstruction: it starts from the inner tracker tracks and flags them as muons by searching for matching segments in the muon spectrometer. The muon candidates produced with this strategy are referred to as "tracker muons".
After the completion of both algorithms, the reconstructed stand-alone, global and tracker muons are merged into a single software object, with the addition of further information, like the energy collected in the matching calorimeter towers. This information can be used for further identification, in order to achieve a balance between efficiency and purity of the muon sample.

3.3.4 Calorimetry

Identification of electrons, photons, and hadrons relies on accurate calorimetry, which is a destructive measurement of the energy of a particle. As in most of the particle physics experiments, a distinction is made between electromagnetic calorimetry and hadron calorimetry. Electromagnetic calorimetry is based on the production of EM showers inside a high-Z absorber, while hadron calorimetry measures the effects of inelastic scattering off heavy nuclei of hadrons, including production of photons from neutral pions and muons, and neutrinos from weak decays. Calorimetry must be precise and hermetic also to measure any imbalance of momenta in the transverse plane which can signal the presence of undetected particles such as high-p_T neutrinos.

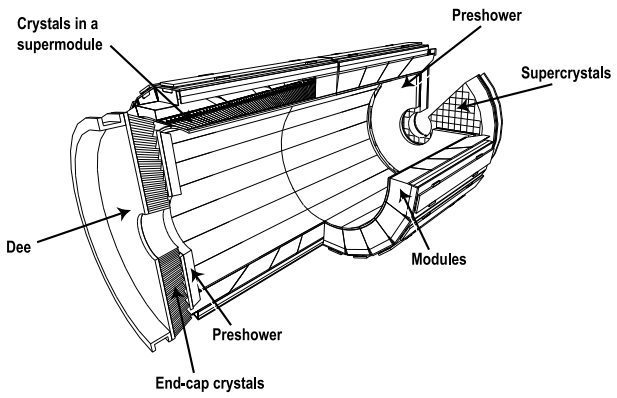

Figure 3.13: Cut-away view of the CMS ECAL showing the hierarchical structure of crystals arranged in supercystals and modules and the orientation of crystals whose major axis is always directed to the origin of the reference frame. Figure from [46].

The electromagnetic calorimeter of CMS, ECAL, is a homogeneous calorimeter, where the absorber material is the same as the sensitive one [46]. ECAL is composed of 61,200 lead tungstate ($PbWO_4$) crystals in the barrel region and

7,324 crystals in the end-caps, as shown in Fig. 3.13. The crystal cross-section is 22×22 mm^2 at the front face, while the length is 230 mm. End-caps are equipped with a preshower detector. $PbWO_4$ was chosen because of its high density, 8.28 g/cm^3, short radiation length, 0.89 cm, small Molière radius, 2.2 cm. This way, the calorimeter can be kept compact with fine granularity, while scintillation and optical properties of $PbWO_4$ make it fast and radiation tolerant. Signal transmission exploits total internal reflection. Scintillation light detection relies on two different technologies. Avalanche photodiodes (APD) are used in the barrel region, mounted in pairs on each crystals, while vacuum phototriodes (VPT) are used in the end-caps. The preshower detector is a sampling calorimeter composed of lead radiators and silicon strips detectors, and it is used to identify neutral pions in the forward region. The nominal energy resolution, measured with electron beams having momenta between 20 and 250 GeV, is

$$\left(\frac{\sigma_E}{E}\right)^2 = \left(\frac{2.8\%}{\sqrt{E}}\right)^2 + \left(\frac{0.12}{E}\right)^2 + (0.30\%)^2 \tag{3.4}$$

where the different contributions are respectively: the stochastic one, due to fluctuations in the lateral shower containment and in the energy released in the preshower, that due to electronics, digitization and pile-up, and the constant term, due to intercalibration errors, energy leakage from the back of the crystal and non-uniformity in light collection.

The hadron calorimeter of CMS, HCAL, is a sampling calorimeter employed for the measurement of hadron jets and neutrinos or exotic particles resulting in apparent missing transverse energy [47]. A longitudinal view of HCAL is shown in Fig. 3.14. The hadron calorimeter size is constrained in the barrel region, $|\eta| < 1.3$, by the maximum radius of ECAL and the inner radius of the solenoid coil. Because of this, the total amount of the absorber material is limited and an outer calorimeter layer is located outside of the solenoid to collect the tail of the showers. The pseudorapidity coverage is extended in the $3 < |\eta| < 5.2$ by forward Cherenkov-based calorimeters. The barrel part, HB, consists of 36 wedges, segmented into 4 azimuthal sectors each, and made out of flat brass absorber layers, enclosed between two steel plates and bolted together without any dead material on the full radial extent. There are 17 active plastic scintillator tiles interspersed between the stainless steel and brass absorber plates, segmented in pseudorapidity to provides an overall granularity of $\Delta\phi \times \Delta\eta = 0.087 \times 0.087$. The same segmentation is maintained in end-cap calorimeters, HE, up to $|\eta| < 1.6$, while it becomes two times larger in the complementary region. The maximum material amount in both HB and HE corresponds to approximately 10 interaction lengths λ_I. The energy resolution on single electron and hadron jets is shown in Fig. 3.15.

3.3.5 Trigger and Data Acquisition

High bunch crossing rates and design luminosity at LHC correspond to approximately 20-25 superimposed events every 25 ns, for a total of 10^9 events per second.

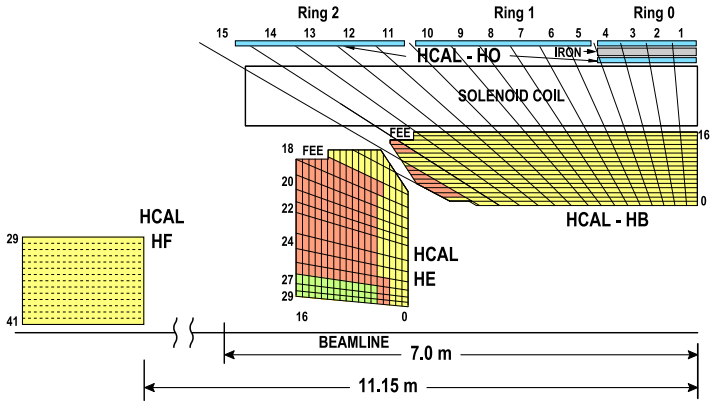

Figure 3.14: Cross section of the CMS HCAL showing the tower segmentation. Figure from [47].

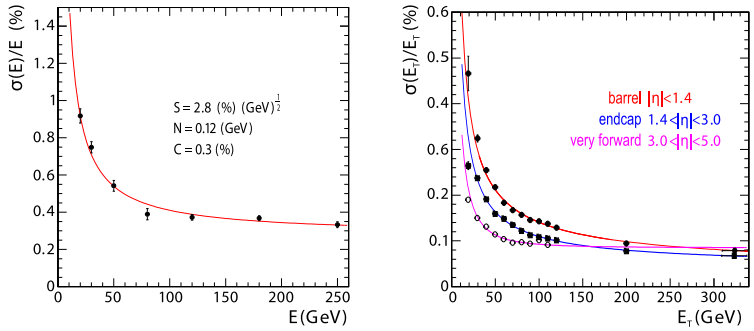

Figure 3.15: Left: ECAL energy resolution as a function of the electron energy as measured from a beam test. The energy was measured in a 3×3 crystals array with the electron impacting the central one. The stochastic, noise and constant terms are given. Right: the jet transverse energy resolution as a function of the transverse energy for barrel jets, end-cap jets and very forward jets reconstructed with an iterative cone algorithm with cone radius $R = 0.5$. Figures from [32].

The large amount of data associated to them is impossible to store and process, therefore a dramatic rate reduction has to be achieved. This is obtained with two steps: the Level 1 Trigger [48] and the High Level Trigger, HLT [49].

The Level 1 Trigger is based on custom and programmable electronics, while HLT is a software system implemented on a $\sim$ 1000 commercial processors farm. The maximum allowed output rate for Level 1 Trigger is 100 kHz, which should be even kept lower, about 30 kHz, for safe operation. Level 1 Trigger uses rough information from coarse segmentation of calorimeters and Muon Detectors and holds the high-resolution data in a pipeline until acceptance/rejection decision is made. HLT exploits the full amount of collected data for each bunch crossing accepted by Level 1 Trigger and is capable of complex calculations such as the off-line ones. HLT algorithms are those expected to undergo major changes in time, particularly with increasing luminosity. Configuration and operation of the trigger components are handled by a software system called Trigger Supervisor.

The Level 1 Trigger relies on local, regional and global components. The Global Calorimeter and Global Muon Triggers determine the highest-rank calorimeter and muon objects across the entire experiment and transfer them to the Global Trigger, the top entity of the Level 1 hierarchy. The latter takes the decision to reject an event or to accept it for further evaluation by the HLT. The total allowed latency time for the Level 1 Trigger is 3.2 μs. A schematic representation of the Level 1 Trigger data flow is presented in Fig. 3.16.

Muon Trigger

All Muon Detectors – DT, CSC and RPC – contribute to the Trigger. Barrel DT's provide Local Trigger in the form of track segments in ϕ and hit patterns in η. End-cap CSC's provide 3-dimensional track segments. Both CSC's and DT's provide also timing information to identify the bunch crossing corresponding to candidate muons. The Local DT Trigger is implemented in custom electronics. BTI's, Bunch and Track Identifiers, search for coincidences of aligned hits in the four equidistant planes of staggered drift tubes in each chamber superlayer. From the associated hits, track segments defined by position and angular direction are determined. TRACO's, Track Correlators, attempt to correlate track segments measured in DT ϕ superlayers, enhancing the angular resolution and producing a quality hierarchy.

The requirement of robustness implies redundancy, which introduces, however, a certain amount of noise or duplicate tracks giving rise to false Triggers. Therefore the BTI's, the TRACO's and the different parts of the Local Trigger contain complex noise and ghost reduction mechanisms. The position, transverse momentum and quality of tracks are coded and transmitted to the DT regional Trigger, called the Drift Tube Trigger Track Finder (DTTF), through high-speed optical links.

The Global Muon Trigger combines the information from DT's, CSC's and

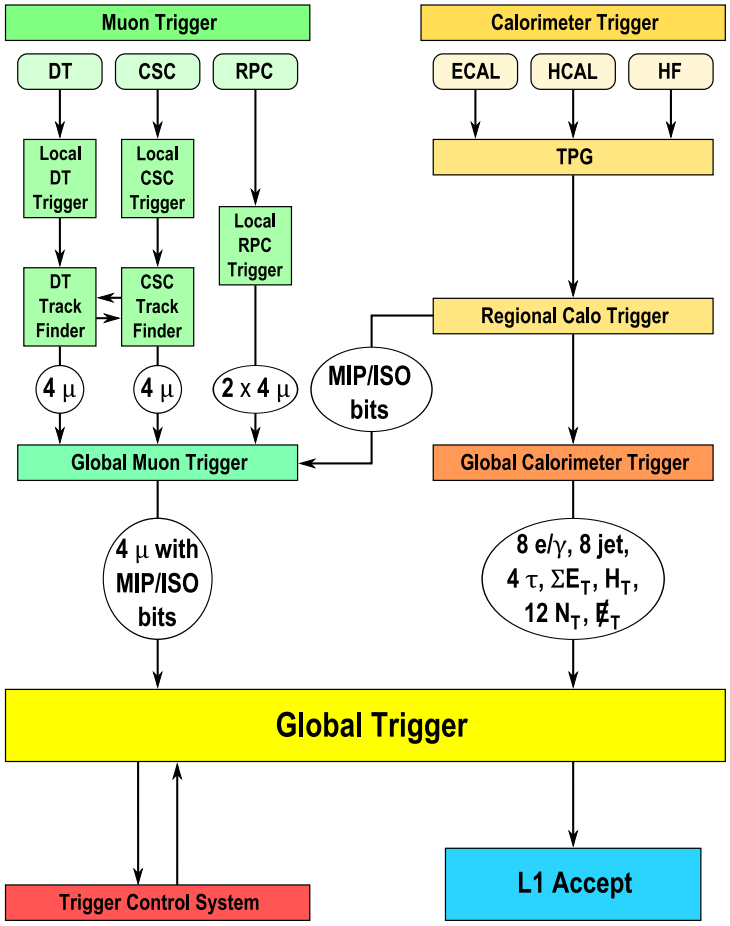

Figure 3.16: Schematic representation of the Level 1 Trigger data flow.

RPC's, achieving an improved momentum resolution and efficiency compared to the stand-alone systems. It also reduces the Trigger rate and suppresses backgrounds by making use of the complementarity and redundancy of the three Muon Systems. The Global Muon Trigger also exploits MIP/ISO bits from the Regional Calorimeter Trigger. A muon is considered isolated if its energy deposit in the calorimeter region from which it emerged is below a defined threshold. DT and CSC candidates are first matched with barrel and forward RPC candidates based on their spatial coordinates. If a match is possible, the kinematic parameters are merged. Several merging options are possible and can be selected individually for all track parameters, taking into account the strengths of the individual Muon Systems. Muons are back-extrapolated through the calorimeter regions to the vertex, in order to retrieve the corresponding MIP and ISO bits, which are then added to the GMT output and can be taken into account by the Global Trigger. Finally, the muons are sorted by transverse momentum and quality to deliver four final candidates to the GT. The Muon Trigger is designed to cover up to $|\eta| < 2.4$.

Global Trigger

The Global Trigger takes the decision to accept or reject an event at Level 1, based on candidate e/γ, muons, jets, as well as global quantities such as the sums of

transverse energies (defined as $E_T = E \sin\theta$), the missing transverse energy vector $\not{E}_T$, the scalar transverse energy sum of all jets above a chosen threshold (usually identified by the symbol H_T), and several threshold-dependent jet multiplicities. Objects representing particles and jets are ranked and sorted. Up to four objects are available and characterized by their p_T or E_T, direction and quality. Charge, MIP and ISO bits are also available for muons. The Global Trigger has five basic stages implemented in FPGAs: input, logic, decision, distribution and read-out. If the Level 1 Accept decision is positive, the event is sent to the Data Acquisition stage.

High Level Trigger and Data Acquisition

The CMS Trigger and DAQ system is designed to collect and analyze the detector information at the LHC bunch crossing frequency of 40 MHz. The rate of events to be recorded for offline processing and analysis is of the order of a few 10^2 Hz. The first level Trigger is designed to reduce the incoming average data rate to a maximum of 100 kHz, by processing fast Trigger information coming from the Calorimeters and the Muon System, and selecting events with interesting signatures. Therefore, the DAQ system must sustain a maximum input rate of 100 kHz, and must provide enough computing power for a software filter system, the High Level Trigger (HLT), to reduce the rate of stored events by a factor of 1000. In CMS all events that pass the Level 1 Trigger are sent to a computer farm (Event Filter) that performs physics selections, using faster versions of the offline reconstruction software, to filter events and achieve the required output rate. The various subdetector front-end systems store data continuously in 40-MHz pipelined buffers. Upon arrival of a synchronous Level 1 Trigger Accept via the Timing, Trigger and Control System (TTCS) the corresponding data are extracted from the front-end buffers and pushed into the DAQ system by the Front-End Drivers (FED's). The event builder assembles the event fragments belonging to the same Level 1 Trigger from all FED's into a complete event, and transmits it to one Filter Unit (FU) in the Event Filter for further processing. The DAQ system includes back-pressure from the filter farm through the event builder to the FED's. During operation, Trigger thresholds and pre-scales will be optimized in order to fully utilize the available DAQ and HLT throughput capacity.

3.4 Monte Carlo Event Generator and Data selection

3.4.1 Monte Carlo Event Generator

Monte Carlo (MC) event generators provide an event-by-event prediction of complete hadronic final states based on QCD calculation. They allow to study the topology of events generated in hadronic interactions and are used as input for detector simulation programs to investigate detector effects. The event simulation is divided into different stages as illustrated in figure 3.17. First, the partonic cross section is evaluated by calculating the matrix element in fixed order pQCD.

The event generators presently available for the simulation of proton-proton collisions provide perturbative calculations for beauty production up to NLO. Higher order corrections due to initial and final state radiation are approximated by running a parton shower algorithm. The parton shower generates a set of secondary partons originating from subsequent gluon emission of the initial partons. It is followed by the hadronization algorithm which clusters the individual partons into color-singlet hadrons. In a final step, the short lived hadrons are decayed. In the framework of the analysis presented here, the MC event generator PYTHIA 6.4 [rif.] is used to compute effciencies, kinematic distributions, and for comparisons with the experimental results. This programs were run with its default parameter settings, except when mentioned otherwise.

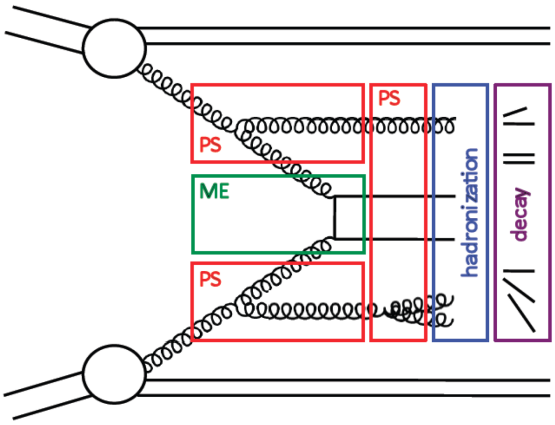

Figure 3.17: Schematic view of the subsequent steps of a MC event generator: matrix element (ME), parton shower (PS), hadronization and decay.

PYTHIA

In the PYTHIA program, the matrix elements are calculated in LO pQCD and convoluted with the proton PDF, chosen herein to be CTEQ6L1. The mass of the b-quark is set to $m_b = 4.8$ GeV. The underlying event is simulated with the D6T tune [rif.]. Pile-up events were not included in the simulation. The parton shower algorithm is based on a leading-logarithmic approximation for QCD radiation and a string fragmentation model (implemented in JET-SET [rif.]) is applied. The longitudinal fragmentation is described by the Lund symmetric fragmentation function [rif.] for light quarks and by the Peterson fragmentation function for charm and beauty quarks. The parameters of the Peterson fragmentation function are set to $\epsilon_c = 0.05$ and $\epsilon_b = 0.005$. In order to estimate the systematic uncertainty introduced by the choice of the fragmentation function, samples generated with different values of ϵ_b are studied. The hadronic decay chain used in PYTHIA is also implemented by the JETSET program. For comparison, additional event samples are generated where the EvtGen [rif.] program is used to decay the b-hadrons. EvtGen is an event generator designed for the simulation of the physics of b-hadron decays, and in particular provides a framework to handle complex sequential decays and CP violating decays.

3.4.2 Data selection

Here we briefly summarize the general slections on muons and jets in the data. As we have seen a track is associated to a muon. The quality of this track is associated with the number of hits in the detector and and the goodness of the fit that adapts the trajectory. Now we elencate the features of the track associated with a muon to pass the selection:

- at least 12 hits in the inner silicon tracker,
- $|\eta^{\mu}| < 2.1$
- $p_T^{\mu} > 3$ GeV
- the χ^2/ndf of the fit of the trajectory in the inner tracker is at least 2,
- the χ^2/ndf of the fit of the global track of the muon is at least 10,
- the number of muon chambers with matched segments is at least 2.

For jets instead the general selection is:

- $p_T^{jet} > 10$ GeV,
- $|\eta^{jet}| < 2.6$.

These are the general selections for muons and jets. They can be modified in the analysis, when it happen it will be specified.

Chapter 4

Pile Up analysis

4.1 Introduction

At LHC the expected luminosity at the nominal centre of mass energy of $\sqrt{s} = 14$ TeV is about 10^{34} cm^{-2} s^{-1} ; this involves a great number of primary vertices for every collision of the beams, this is the pile up problem. Even at smaller luminosities pile up effect are sizeable. It's clear that if we are interested to a particular channel, like in this analysis on dimuon pairs from $pp \to \mu\mu X$, we need that the muons arrive from the same vertex. In this section we want to evaluate the pile up effect and then subtract it for the dimuonic analysis.

Pile up (PU) was rejected in the measurement of $b\bar{b}$ cross section [riferimento] by requiring that the pair of muons arrived from the same reconstructed vertex. However, for our analysis we initially consider all the couples of muons for each even: if there are more than two muons in the event, we consider all the possible combinations.

In the analysis algorithm every muon is associated with a track, and the track is associated with the nearest vertex, chosing that with the smallest impact parameter.

We take only muons with $p_T > 4$ GeV, to masimize our statistics moving as much as possible from the turn on curve of the trigger (trigger cuts at 3 GeV). Muon tracks are associated with a vertex only if the impact parameter along the transverse plane is less then 1 cm. This is because it's very diffcult that a muon with a track with an impact parameter grater than 1 cm may come from that vertex, even taking into account that the algorythm has an inherent error in the valutation of the vertex position and of the track. In presence of jets, we take events with $p_T^{jet} > 5$ GeV. It's a very low theresholds for jets transverse momentum, so to have maximal statistic for our analysis.

In this analysis we have initially three samples of data linked to three periods. In particular we have the follow dataset:

- November 2010, with about 6 millions of events ($\mathcal{L} \sim 0.2 \cdot 10^{32}$ cm^{-2} s^{-1});
- May 2011, with about 5.5 millions of events ($\mathcal{L} \sim 10^{32}$ cm^{-2} s^{-1});
- August 2011, with about 1.5 millions of events ($\mathcal{L} \sim 2 \cdot 10^{32}$ cm^{-2} s^{-1}).

Because the luminosity increases with time, we expect that the effect of PU is more important in the late 2011 data. In particular we are interested to the difference between the impact parameters for two muons along z axis, Δz. If we call V_1 and V_2 the positions of vertices along z axis, and z_1, z_2 the positions of the intersections, along z axis, of the muon tracks and the beam line (see figure 4.1a), we can define

$$\Delta z = (z_1 - V_1) - (z_2 - V_2) = z_1 - z_2 - (V_1 - V_2). \tag{4.1}$$

Note that in the n-tuples are present $z_i - V_i$ and V_i, not z_i.

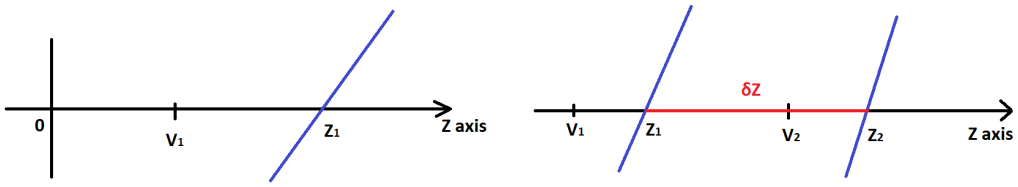

(a) Definition of V_i and z_i.

(b) Definition of δz.

Figure 4.1: Muon tracks are shown in blue. The zero comes from the geometry of the detector.

We can plot the Δz distributions for each pairs of muons for all the dataset; in particular we plot three cases that we are able to distinguish:

1. Δz for all the pairs of muons;
2. Δz for the case in which the muons arrive from same vertex ;
3. Δz for the case in which the muons arrive from different vertices.

We show all in Figure 4.2. From these figures we can see that there are no particular differences between the three datasets, the shape of distributions is always the same, with a peak on the mean at $\Delta z = 0$. Now, from definition (4.1), it's evident that the distributions of Δz for the case same and different vertices can't be different. This is because the distributions of the impact parameters $z_i - V_i$ are the same for $i = 1, 2$, so it's indifferent if the vertex is the same or not.

4.1.1 New variable : δz

To understand the pile-up effect, it's necessary to define a new variable that can distinguish the cases of muons coming from same and different vertices. A possible candidate is the distance, projected along z-axis, between the tracks associated with the muons (figure 4.1b):

$$\delta z = \Delta z + V_1 - V_2 = z_1 - z_2. \tag{4.2}$$

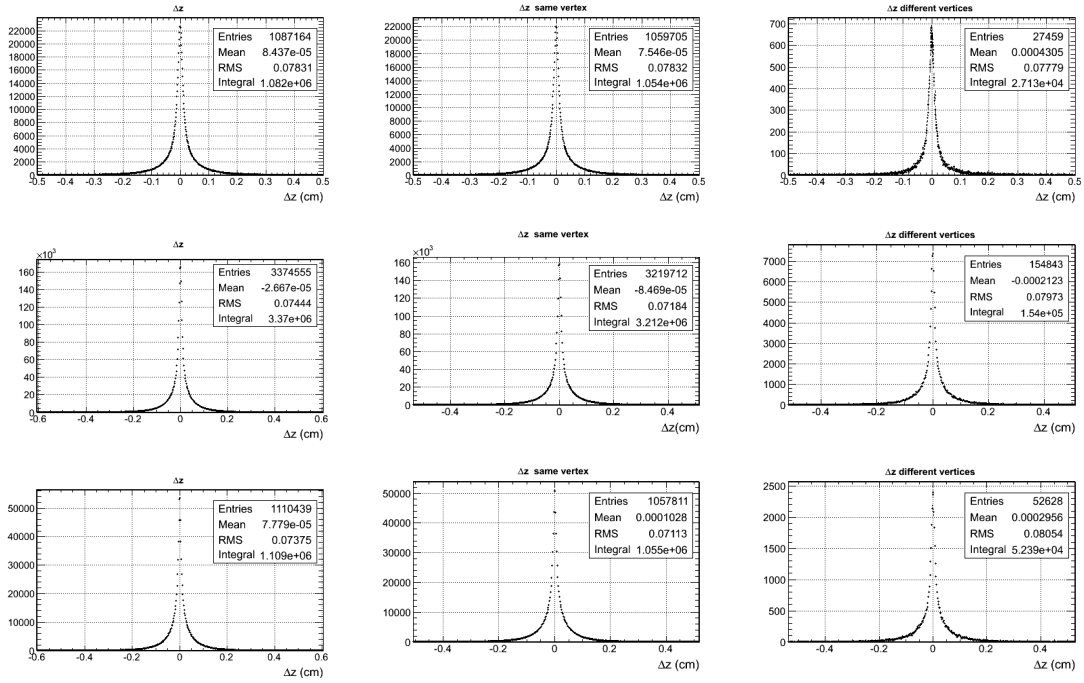

Figure 4.2: Distribution of Δz. First row are data from November 2010, the second from May 2011 and the third from August 2011. First column is for all the pairs of muons, the second for muons from same vertex, the third for muons from different vertices.

If the muons come from same vertex $\delta z = \Delta z$. We plot this variable as previous by Δz in figure 4.3.

As anticipated, there are no differences with Δz for the case of muons from the *same vertex*. Instead for the case of muons from *different vertices* we have a new shape (third column in figure 4.3). The peculiar shapes of the different vertex case can be explained as follows. First, there is an increase of the number of events until this number falls close to the mean. To explain this increase we remember that if there are many primary vertices (PV), it's easier to find closer pairs of vertices. But in this case muons from the same vertex could be associated with different vertices, causing the increase similar to same vertex case.

To explain the dip close to zero we note, first of all, that the dip is like a reversed peak similar to same vertex case. This fact leads us to believe that the fall is due to the resolution of our analysis algorithm: it doesn't distinguish vertices very close together, reducing them to only one vertex. An important observation is that the reconstruction algorithm of the vertices is different between data 2010 and 2011. That's the principal cause for the differences between plots in the third column in figure 4.3. In particular, plot of the 2010 has a larger hole in the centre of distribution.

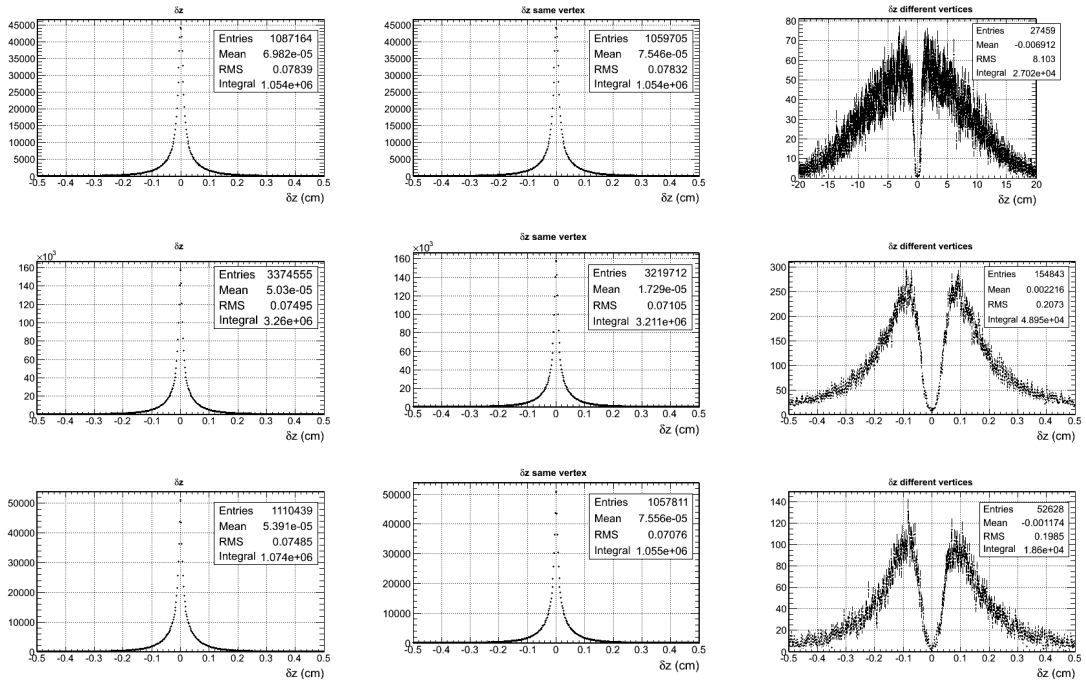

Figure 4.3: Distribution of δz. First row are data from November 2010, the second from May 2011 and the third from August 2011. First column is for all the pairs of muons, the second for muons from same vertex, the third for muons from different vertices.

4.2 Checks

4.2.1 PV number VS run number.

First we can analize in 2-dimensional plots the number of primary vertices (*PVnumber*) in the samples as a function of the run numbers (*runNumber*). The run determines the period of data taking, it is increasing with time and accordingly with luminosity. We can do this control for all the samples; we expect that the *PVnumber* increase with *runNumber* and that there are more events for higher *runNumber* (because of luminosity).

As we can see from figures 4.4, 4.5 and 4.6, the number of PV increases with time, as we expected, in particular *PVnumber* is about 15 for November 2010 (Figure 4.4), instead for the other two is about 20. Within the same period there is a tendence of increase of the number of PV as a funcion of runNumber.

Finally we note that the case with all the pairs of muons are very similar with the case of muons from same vertex, because the number of pairs of muons from different vertices is significantly lower. Nevertheless also the cases of muons from different vertices have a similar behavior. Maybe we could expect to observe a greater number of PV in this last case; to better understand the behavior of the case of different vertices we refer to next check.

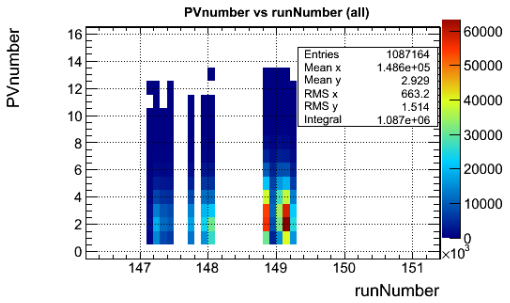

(a) All pairs of muons.

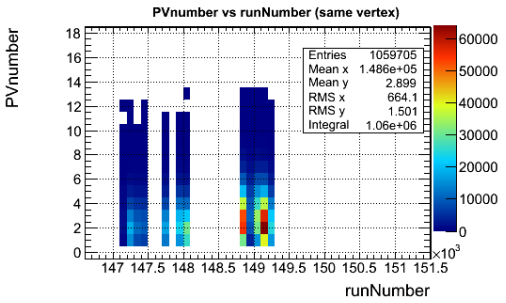

(b) Muons from same vertex.

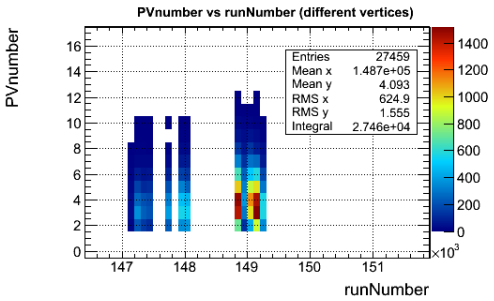

(c) Muons from different vertices.

Figure 4.4: Distributions *PVnumber* VS *runNumber* from November2010.

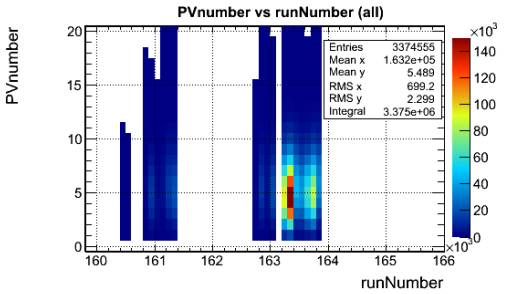

(a) All pairs of muons.

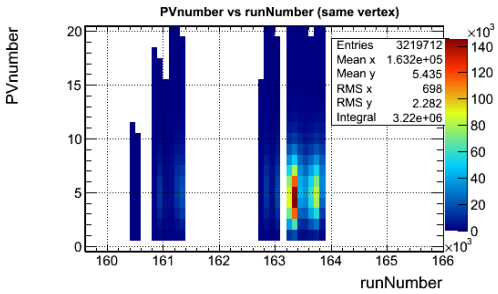

(b) Muons from same vertex.

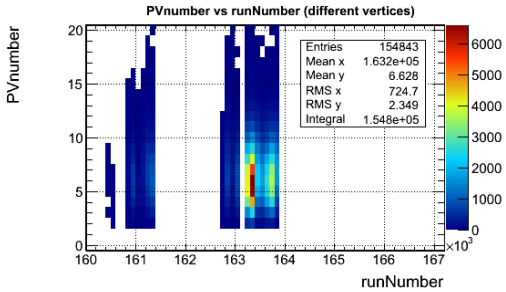

(c) Muons from different vertices.

Figure 4.5: Distributions *PVnumber* VS *runNumber* from May 2011.

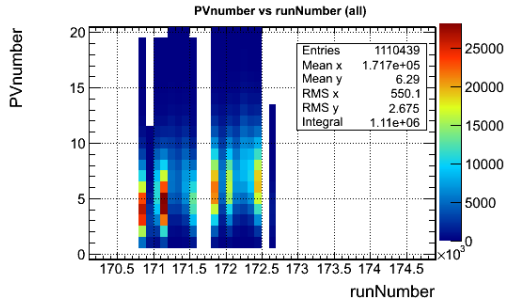

(a) All pairs of muons.

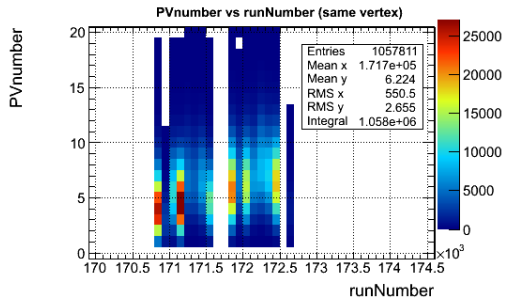

(b) Muons from same vertex.

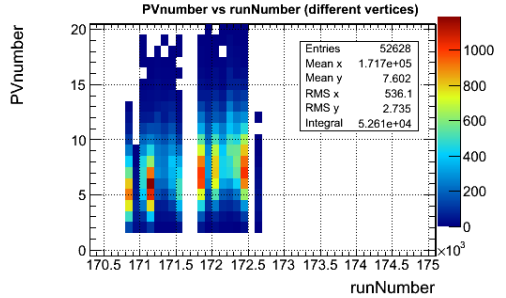

(c) Muons from different vertices.

Figure 4.6: Distributions *PVnumber* VS *runNumber* from August 2011.

4.2.2 Checks on muons from different vertices.

In this section we consider the cases of muons from different vertices, in particular we are interested to examine the relation between the percentage of events of couple of muons from different vertices with the number of PV or the run number. From the previous plots (figures 4.4, 4.5 and 4.6), we can calculate the percentage of events from different vertices as a function of *PVnumber* or *runNumber*, for all the samples; see figure 4.7

From the plots a dependence on *PVnumber* is evident, in particular the percentage of events from different vertices increases with the presence of an high number of PV. That's reasonable because if there are more vertices, it's more likely that muons come from different vertices. A similar behavior is not observed for the dependence on the run number, where the percentage remains fairly constant. We will expect that the percentage increase with run number but into the same period of data taking there is no this behaviour. However the means of percentage grow between 2010 and 2011. We have in effect a mean 2.5 % for 2010, and for 2011 it's about 4.9 %. This is in agreement with the increase of the luminosity between 2010 and 2011.

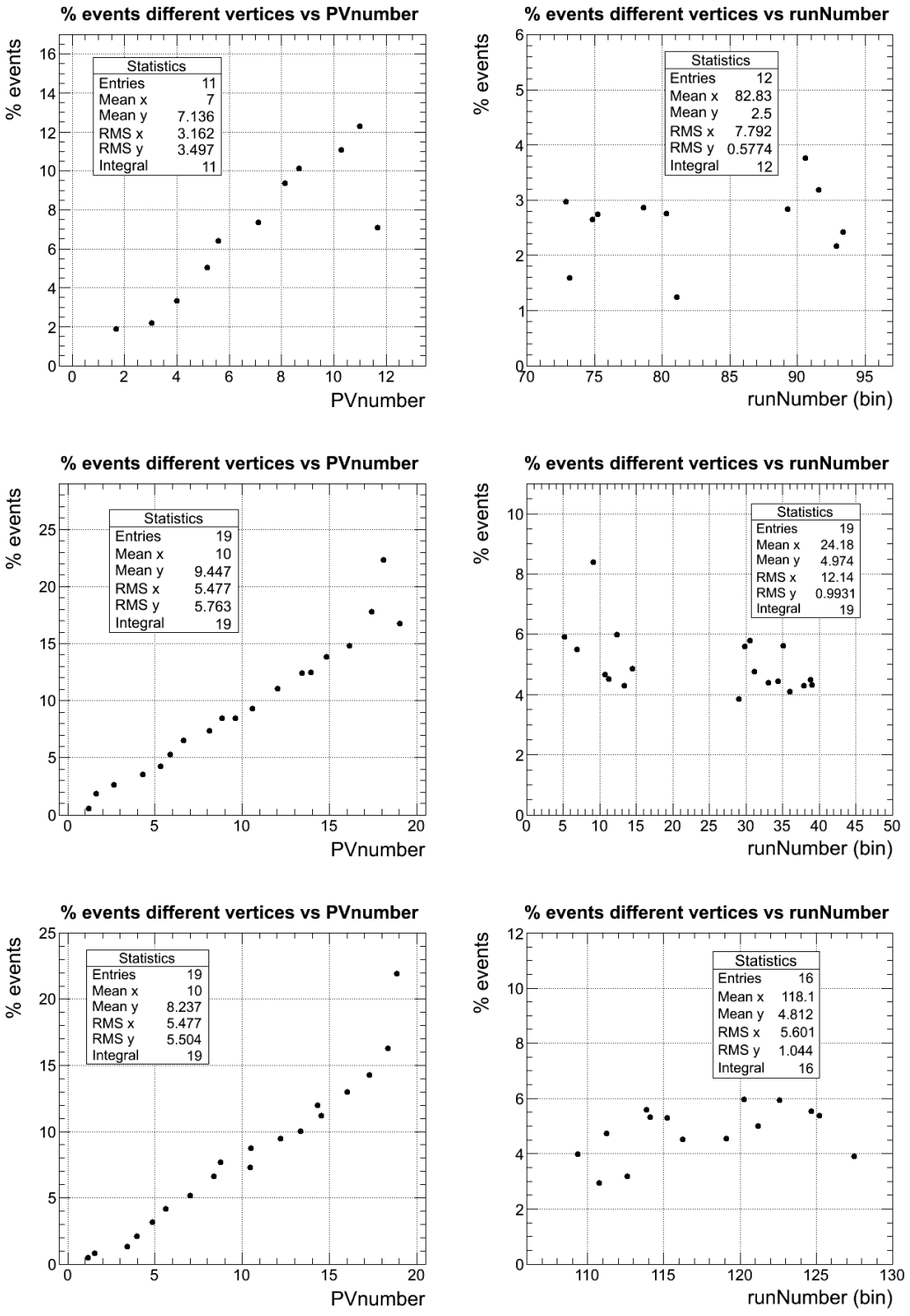

Figure 4.7: The percentages of events of muons from different vertices as a function of the *PVnumber* (on the left) and as a function of the *runNumber* (on the right). First row is for November 2010, the second for May 2011, the third for August 2011.

4.2.3 δz VS PVnumber

Now we can evaluate the consistency of previous check. We take the distributions of δz as a function of *PVnumber* for the period of August 2011, figure 4.8, other periods are similar.

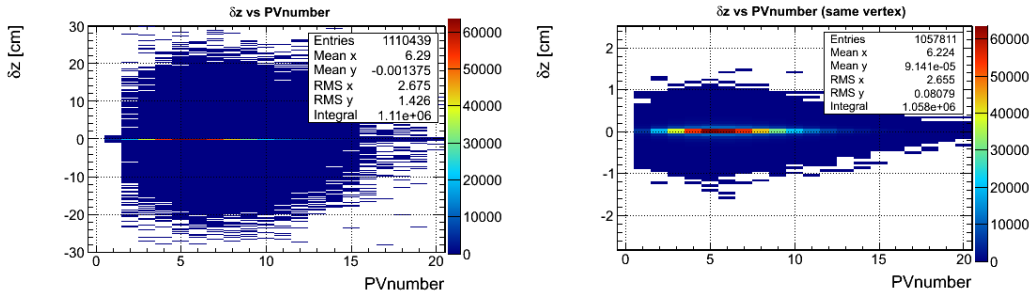

(a) All pairs of muons.

(b) Muons from same vertex.

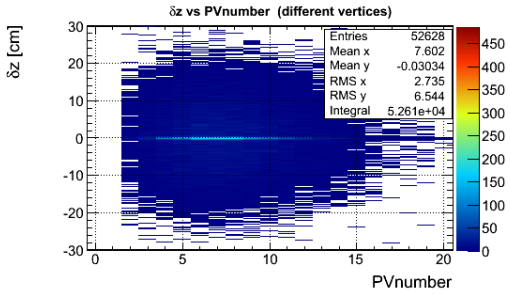

(c) Muons from different vertices.

Figure 4.8: Distributions of δz VS *PVnumber* for data from August 2011.

Note that the δz distribution is wider in the case with all the events because of the contribution from muons from different vertices, and it has a concentration of events for $\delta z = 0$ due to the muon from same vertex. At this point we can cut this plots for each PVnumber and evaluate the RMS of the distributions. In this way we have an idea of the effect of the presence of muons from different vertices on the distribution. We plot, for the three periods, all the distributions in figure 4.9.

From the plots we can see that the RMS are very large for the case of different vertices; this fact, summed with the increase of the percentage of muons from different vertices with the increase of PVnumber, discussed in the previous section, involves an increase of the RMS at the same way for the case of all the pairs of muons (first column of plots in figure 4.9), as its logical conseguence.

4.3 Estimate of events from Pile Up.

Now we are ready to estimate the PU effect on our datasets. In paticular we can evaluate the number of PU events in each periods of data taking. We are able to distinguish the charge of the muons, so we can estimate the PU effect for these cases:

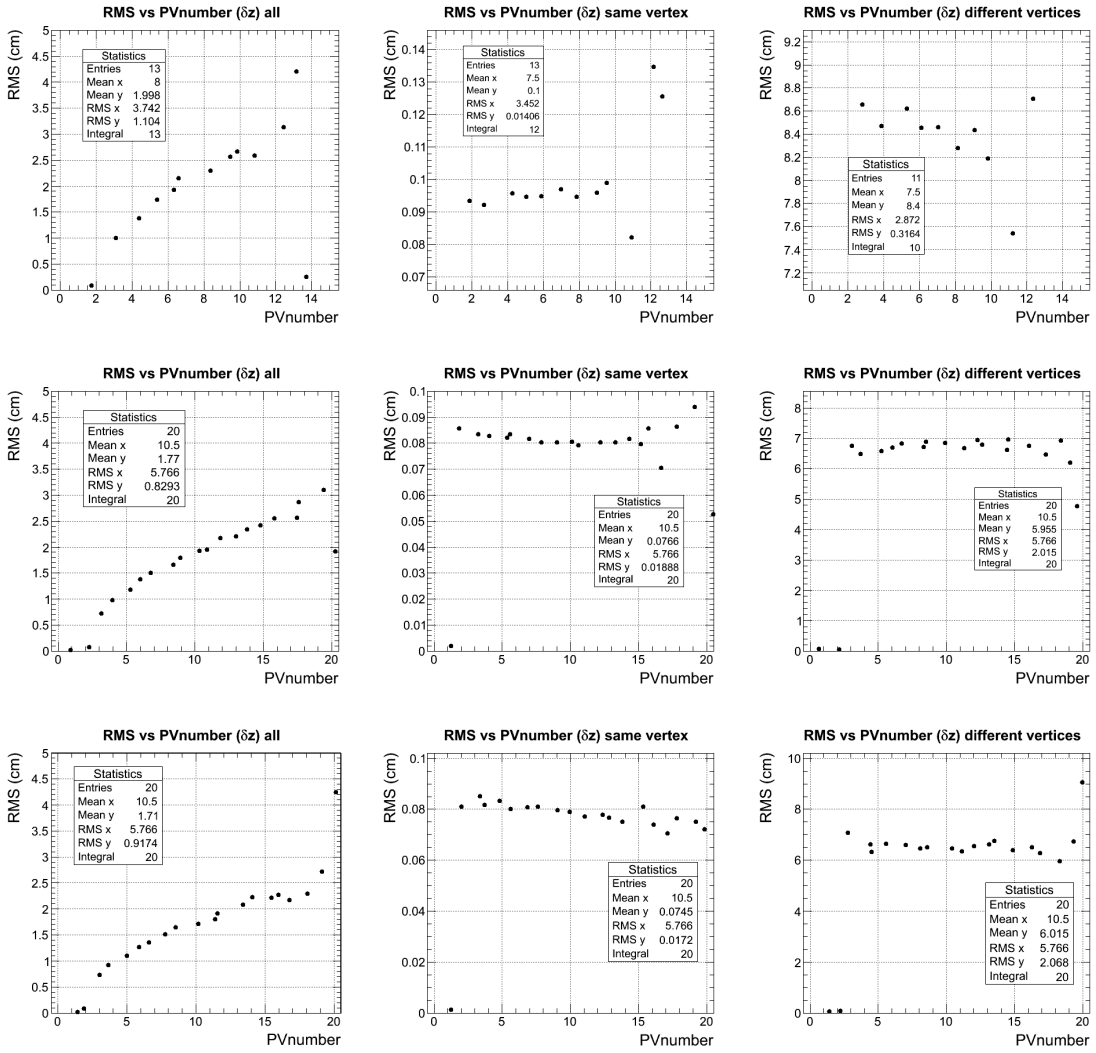

Figure 4.9: Distribution of RMS. First row are data from November 2010, the second from May 2011 and the third from August 2011. First column is for all the pairs of muons, the second for muons from same vertex, the third for muons from different vertices.

- All pairs of muons;
- Two muons of opposite charge sign (OS);
- Two muons of same sign, both positive or negative ($SS+$ or $SS-$).

We take these distributions and fit them to evaluate the PU effect. The fits are performed using the sum of a relativistic Breit-Wigner function, a Gaussian function, two exponential functions and a zero-order polynomial function (a constant):

$$f(x) = \frac{k}{(x^2-\mu^2)^2 + x^2\gamma^2} + A\ e^{-\frac{1}{2}\left(\frac{x-\mu}{\sigma}\right)^2} + k_1\ e^{-\alpha_1|x|} + k_2\ e^{-\alpha_2|x|} + B. \qquad (4.3)$$

This is a fit with 10 parameters:

- k, A, k_1, k_2 are the constants for the amplitude of the functions;
- μ is the mean for Gaussian and Breit-Wigner functions;
- γ is the resonance width of the Breit-Wigner function;
- σ is the standard deviation of the Gaussian function;
- α_1, α_2 are the coeffcients on the exponents for the exponential functions;
- B is the zero-order polynomial function.

We plot the histograms of the distributions of δz in the various cases with the resulting fit functions: first all the pairs of muons (figure 4.10), then separating by the charge relation (figure 4.11). Note that plots are in logarithmic scale.

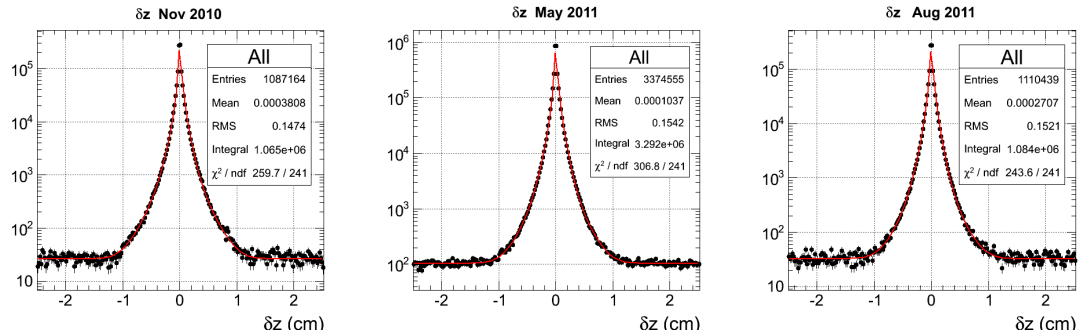

(a) Fit for November 2010. (b) Fit for May 2011. (c) Fit for August 2011.

Figure 4.10: In red fits for the case of all the pairs of muons in the three periods of data taking.

To evaluate the goodness of the fits we use the χ^2/ndf criterion; as we can see in the tables included in the plots, it assumes values in the range $1.01 \div 1.36$.
We consider these results good for our purposes. We can use the parameter B to evaluate the fraction of PU events in the range (in centimeters) $-1 \leq \delta z \leq 1$, where most of the correlated muon events take place. The parameter B measures the level of flat " background" because it is a straight line parallel to the axis of abscissas. Multiplyng B for the width of the range, 2 cm, we have a estimation of the number of PU events. As we are interested in the percent fraction of PU events, we need to determine the total number of events in the same interval, as given by the integral of the histogram in that range.

At this point we can summarize the fractions of PU events in our samples, in the case of all the pairs of muons taken indiscriminately or for each period, or by separating charge; see Table 4.1.

From this table we see that the case $SS+$ has a fraction of PU always greater then the case $SS-$, in all the periods. In Table 4.2 we report these differences.

Note that the errors for August 2011 are greater because of a lower dataset size. From Table 1 we confirm that in 2010 we have less PU events respect to 2011, as we expected because of the increases of luminosity. Another consideration is that the fraction of PU events for the OS case is always less then the others. To explain it,

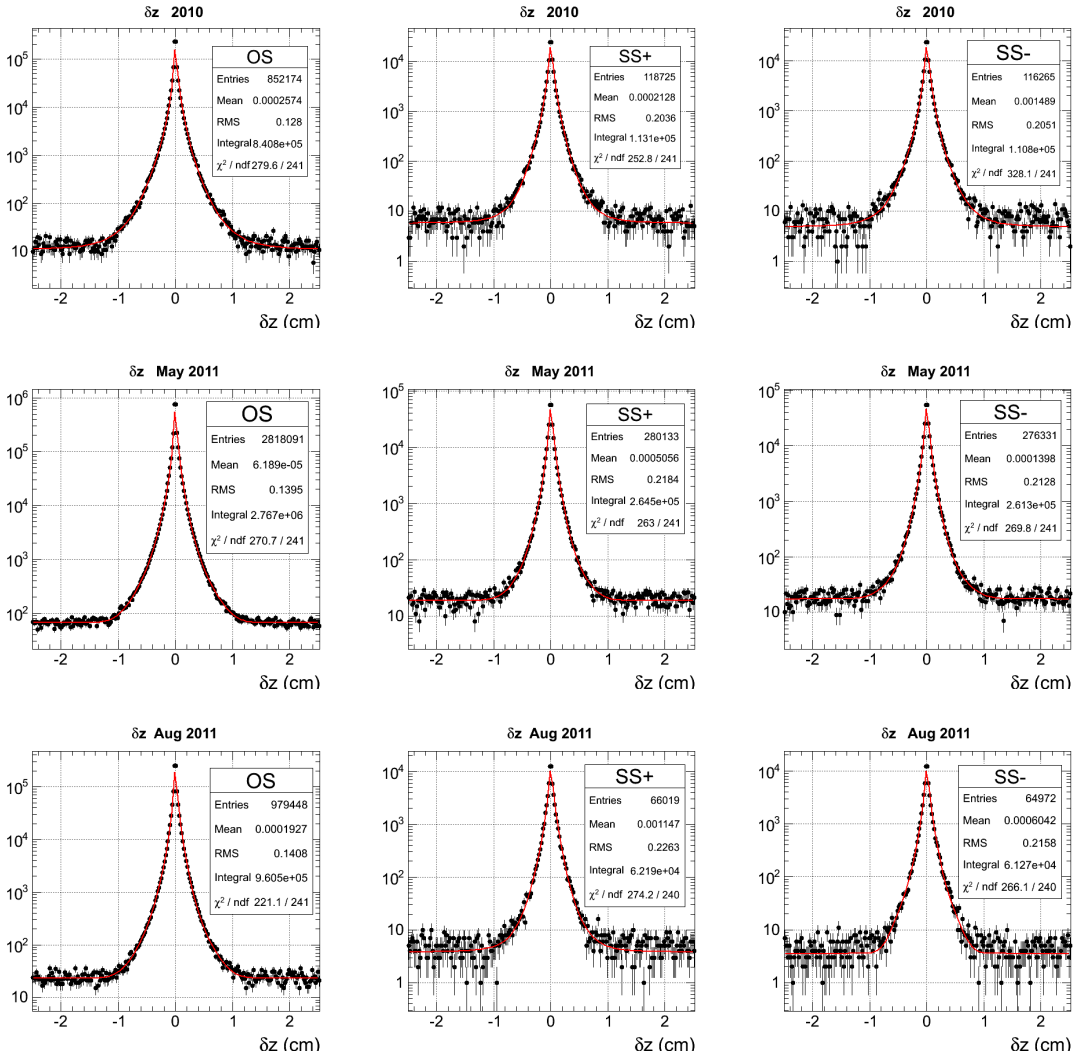

Figure 4.11: Fits for the trhee periods of data taking. In this case we have divided by muon charge: muons of opposite sign charge OS ($\mu^+\mu^-$), muons of same positive sign $SS+$ ($\mu^+\mu^+$), muons of same negative sign $SS-$ ($\mu^-\mu^-$) .

we remember that the PU events are accidentally distribuited for the case $SS+$, $SS-$ and OS , but the correlated OS events are much more frequent than the cases SS, because we are in presence of the signal of $pp \to b\bar{b}X$ that has evidently an high presence of opposite sign muons (b and $\bar{b}$ decay tipically in OS muons).

		Fraction of PU events (%)	percent error
ALL	Nov. 2010	0.2497±0.0048	1.94
	May 2011	0.3184±0.0031	0.98
	Aug. 2011	0.3014±0.0053	1.75
Nov. 2010	OS	0.1316±0.0040	3.01
	$SS+$	0.5156±0.0214	4.15
	$SS-$	0.4406±0.0200	4.54
May 2011	OS	0.2393±0.0029	1.23
	$SS+$	0.7165±0.0165	2.30
	$SS-$	0.6694±0.0160	2.40
Aug. 2011	OS	0.2428±0.0050	2.07
	$SS+$	0.6208±0.0317	5.10
	$SS-$	0.5893±0.0311	5.28

Table 4.1: Percentages of PU events and their errors.

Period	Absolute difference	Relative difference (%)
Nov. 2010	(7.51±2.93) 10^{-4}	14.56±5.25
May 2011	(4.71±2.30) 10^{-4}	6.57±3.10
Aug. 2011	(3.14±4.44) 10^{-4}	5.07±6.97

Table 4.2: Differences between $SS+$ and $SS-$ cases.

4.4 Further Checks

To overcome the PU problem usually is imposed (by algorithms in the analysis stage) that muons come from same vertex. In this case we take events with two muons and no more. Both muons have to pass our selections, the same as the previous analysis. As we have seen if muons come from the same vertex then $\Delta z = \delta z$. So we plot the variable Δz for our samples (Figure 4.12). We compare with a Montecarlo (MC) simulation sample of about 800 000 events generated without PU. As we can see the distributions are really similar to the previous, as we expected because they are a subsample of them. MC has the same shape.

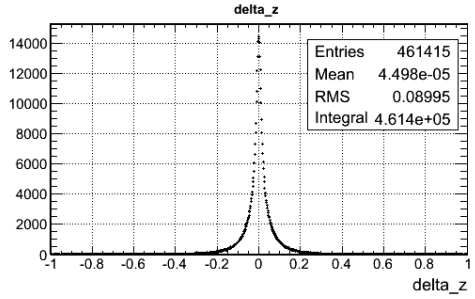

(a) November 2010.

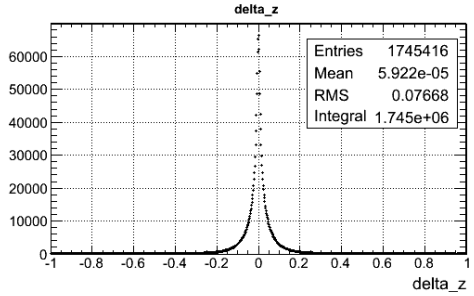

(b) May 2011.

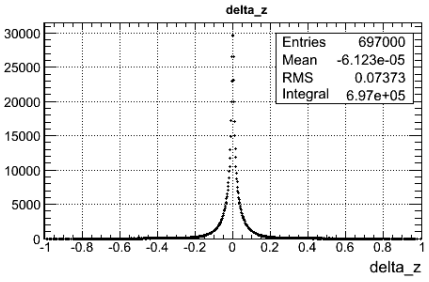

(c) August 2011.

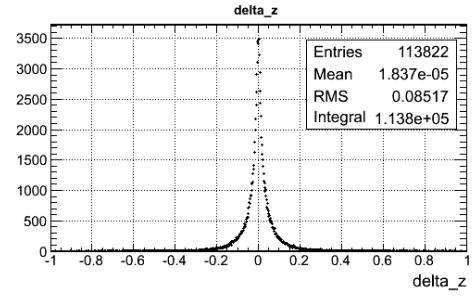

(d) Simulated events by MC.

Figure 4.12: Distributions of Δz for events with only two muons from the same vertex.

To better understand this distributions we can study their dependence on the *PVnumber*. In fact we have two muons from same vertex but the number of primary vertices in the event is independent. We report the distributions in figure 4.13.

To make considerations more appropriate we divide these histograms in some ranges in number of primary vertices. In particular the ranges are choosen to have an approximately equal number of entries. Therefore we use this convention: the first range is in black, the second in red , the third in green and the fourth in blue. In figure 4.14 these plots are represented in logarithmic scale; for the MC sample there are only two ranges because the first is very populated respect the rest. In table 4.3 we report the ranges for our samples divided for number of primary vertices.

Analyzing the plots in figure 4.14 we can see that the distributions of the range are overlapped, and this is consistent with the fact that the distribution of Δz

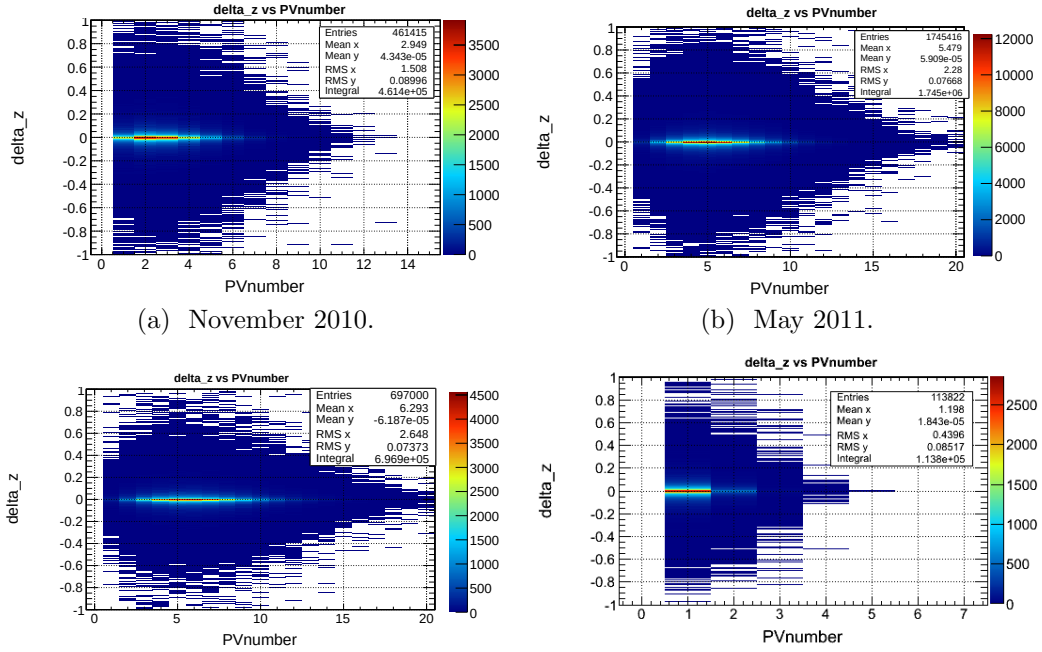

(a) November 2010. (b) May 2011.

(c) August 2011. (d) Simulated events by MC.

Figure 4.13: Distributions of Δz VS PVnumber for events with only two muons from the same vertex.

Sample	range black	range red	range green	range blu
November 2010	[1; 1]	[2; 2]	[3; 3]	[4; 11]
May 2011	[1; 2]	[3; 4]	[5; 6]	[7; 18]
August 2010	[1; 3]	[4; 5]	[6; 7]	[8; 18]
MC	[1; 1]	[2; 5]	-	-

Table 4.3: The ranges for each sample; here the colors for each range are specified.

does not depend on the number of primary vertices. Moreover the distributions of real data are well represented by MC simulation, in fact the shapes are very similar. As anticipated MC simulation doesn't present pile up effect, almost all entries are in effect in the case of only one primary vertex.

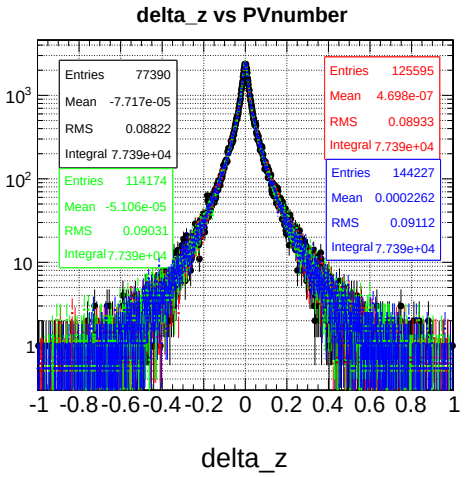

(a) November 2010.

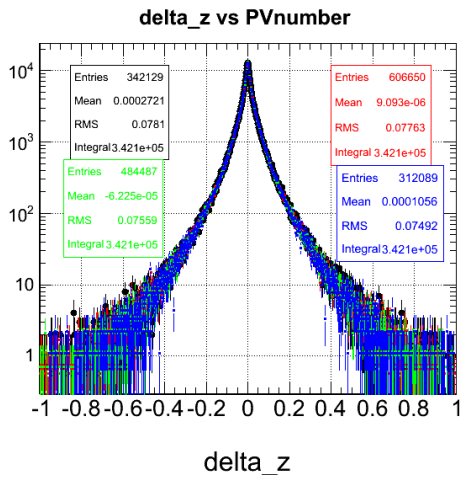

(b) May 2011.

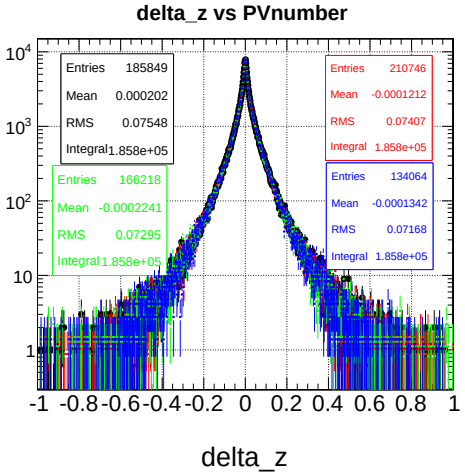

(c) August 2011.

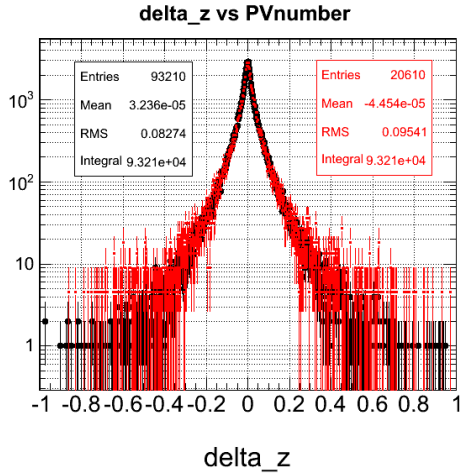

(d) Simulated events by MC.

Figure 4.14: Projections of the plots in figure 4.13.

Chapter 5

Angular resolution of the B-direction

5.1 Introduction

As explained before [2.3.2] we deduce the flavour of the B-hadron at its decay time from the charge of the muon produced in the direct decay process $\mathrm{B} \to \mu\nu_\mu X$. A positive (negative) charge muon tags a B ($\bar{\mathrm{B}}$) particle. With a sample of events consisting only of couples of muons from direct B decays we would compute $\bar{\chi}$ from the rate of equal charge pairs in the overall sample:

$$\bar{\chi} = \frac{N(\mu^+\mu^+) + N(\mu^-\mu^-)}{N(\mu\mu)}.$$

Muons however are often produced from background processes: this makes the measurement more complicated and dilutes the precision of the result. In analyzing a sample of 281 342 simulated MonteCarlo events, we tag muons in several different classes according to the mechanism of their production:

1. primary B decays ($\mathrm{B} \to \mu\nu_\mu X$), corresponding to muons produced in the semileptonic decay of a B hadron,

2. primary C decays ($\mathrm{C} \to \mu\nu_\mu X$), where the muon comes from the semileptonic decay of a charm hadron produced in the pp collision,

3. prompt muons, either charged hadrons punching through the detector up to the muon chambers, or muons from charmonium or bottomonium decays,

4. muons from the decay in flight of a charged pion or kaon

5. sequential B decays, where the muon comes from the semileptonic decay of a charm hadron or the leptonic decay of a tau lepton produced in the B-hadron decay,

6. fake, where there is no relation between the track reconstructed and the particle produced at the generation stage.

Muons from class 5 are the most dangerous, because in most of the cases the relation between the charge of the muon and the flavour of the original B. We can distinguish the backgrounds (classes 2 to 5) from the signal (class 1) by analysing the kinematic properties of the observed particles.

Due to the larger mass, B hadrons inherit a more sizeable fraction of the energy of the parton they come from, which is described by a harder fragmentation function as compared to that of the other quarks. As a consequence, the momentum of the muons produced in the primary B-decay is on average larger than for background events. The cut on the lepton p_T therefore naturally enhances the signal.

In addition we exploit jet information to improve background rejection as done for instance in the LEP experiments. In the rest frame of the decaying hadron, the lepton momentum can be as large as half of the mass of the decaying particle. Therefore, the momentum of signal muon in the parent rest frame can be as large as about 2.5 GeV, to be compared to about 0.9 GeV for muons from charm or tau decays (Class 2 and 5). However we observe the event in the laboratory frame, where the parent hadron has a considerable Lorentz boost. To disentangle signal from background, therefore, we need to compare projection of the lepton momentum in the direction ortogonal to the parent hadron boost. As we do not fully reconstruct the parent hadron, we consider instead the jet connected to it.

When a hard parton is produced at LHC the observable particles produced in the fragmentation and decays of the original parton are emitted within a narrow cone centered around the original parton direction. This flow of collimated particle is referred to as a jet. Jets are reconstructed with high efficiency in CMS with a particle flow algorithm which exploits at best the detector information. The jet momentum is obtained from the vector sum of the momenta of the particles assigned to it. Its direction represents the direction of the original parton. Therefore, to separate signal muon from the background, one could use the variable p_T^{in} corresponding to the muon muomentum computed in the direction perpendicular to the jet main axis. It turns out that background rejection improves if the muon is first removed from the jet and the projection is computed with reference to the axis of the jet obatined without the muon contribution. This variable is called p_T^{out}.

Qui mettere e citare un paio di plot che mostrano ptrel e ptout per le varie categorie. fatto aiutare da Luca o Jacopo.

The spectra of p_T^{out} depend on several factor, as the decay and fragmentation proprties of the particles considered. The following sections describe the means by which we compare the resolution in the definition of the jet axis in the data and in the simulation.

In our analysis we consider the decay of a B hadron into a muon, $B \to \mu X$. We want to determine the angular resolution in the measurement of the B-direction; we compare the direction of the B-jet with that obteined from the line joining the primary to the secondary vertex (B-"flight" direction).

We consider initially a sample of MC simulated events, then we compare it with a sample of real data from 2010. From this analysis it's possible to obtain a systematic uncertainty for the analysis of time integrated mixing probability. The

number of MC simulated events is 281 342 events whilst the events in 2010 data sample are 1 182 197.

Due to efficiency of reconstruction of muons and jets and to the necessity to have a good statistic, we impose the following theresholds in p_T:

- $p_T^{\mu} > 4$ GeV,
- $p_T^{jet} > 10$ GeV.

5.2 Analysis of MC sample

5.2.1 Definitions

Now we define some quantities for the current analysis:

- η^{true} and ϕ^{true} : pseudorapidity and azimuthal angle of the particle generated by MC (this is the "MC truth");
- η^{jet} and ϕ^{jet} : pseudorapidity and azimuthal angle of the jet axis produced by the decay;
- η^{sv} and ϕ^{sv} : pseudorapidity and azimuthal angle of the primary vertex to secondary vertex direction .

Note that there are η^{sv} and ϕ^{sv} only if the secondary vertex (SV) is present, i.e. if we are able to reconstruct the SV. For the η^{jet} and ϕ^{jet} the definition is more general: a jet can be present also when there isn't a reconstructed SV.

From these definitions we can determine the resolutions as:

- $\Delta\eta^{jet} = \eta^{jet} - \eta^{true}$;
- $\Delta\phi^{jet} = \phi^{jet} - \phi^{true}$;
- $\Delta\eta^{sv} = \eta^{sv} - \eta^{true}$;
- $\Delta\phi^{sv} = \phi^{sv} - \phi^{true}$.

Also in this case $\Delta\eta^{sv}$ and $\Delta\phi^{sv}$ are determined only if SV is present.

There's an important consideration to do: jet axis direction can be defined in two cases. The first one is when muon momentum is included into the jet momentum (*jet with muon*). The second when the muon momentum is subtracted from the jet momentum (*jet without muon*). Obviously we expect that the resolution for the first case is better than the second because subtracting the muon from the jet we loose information. Nevertheless it's very interesting to study also the second case because it was seen (riferimento?) that an important discriminator between the various decay channels for the b quark is the p_{out}^t, i.e. the transverse momentum of the muon respect to the direction of the jet axis when muon momentum is subtracted.

5.2.2 MC distributions

Now we report the $\Delta\eta^{jet}$ and $\Delta\phi^{jet}$ distributions as a function of the jet energy (*Ejet*), in the two cases with or without muon momentum inside the jet momentum (Figure 5.1). From these plots it's evident that the resolution improves when the jet energy is high; this is because the jet is more collimates if its energy is higher, as we expect. We show the distribution of $\Delta\eta^{sv}$ and $\Delta\phi^{sv}$ as a function of the flight length (*Lflight*) of the hadron decaying (Figure 5.2), recalling that these can be defined only in SV presence, thence the smaller number of entries compared to the previous case. Resolutions in this case are better if the flight length is greater.

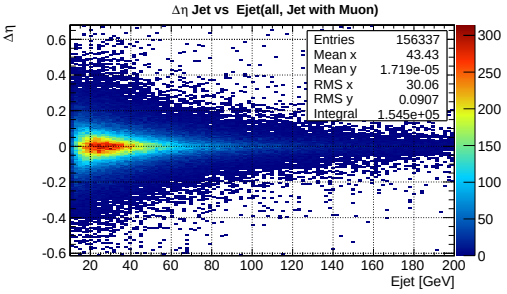

(a) $\Delta\eta^{jet}$ *vs Ejet, Jet with muon.*

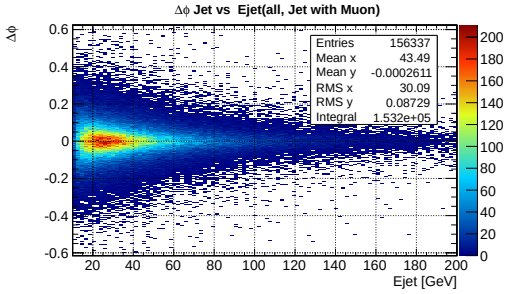

(b) $\Delta\phi^{jet}$ *vs Ejet, Jet with muon.*

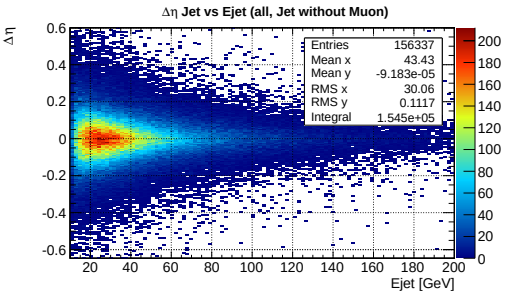

(c) $\Delta\eta^{jet}$ *vs Ejet, Jet without muon.*

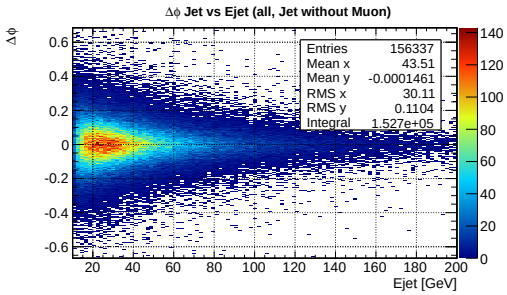

(d) $\Delta\phi^{jet}$ *vs Ejet, Jet without muon.*

Figure 5.1: $\Delta\eta^{jet}$ and $\Delta\phi^{jet}$ distributions for the case with all the events.

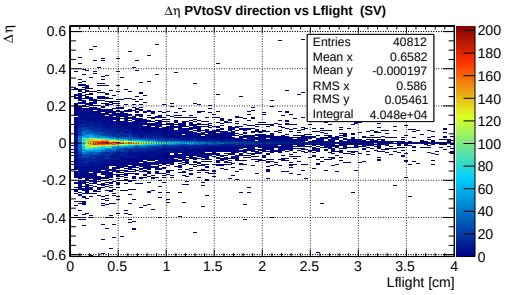

(a) $\Delta\eta^{sv}$ *vs Lflight.*

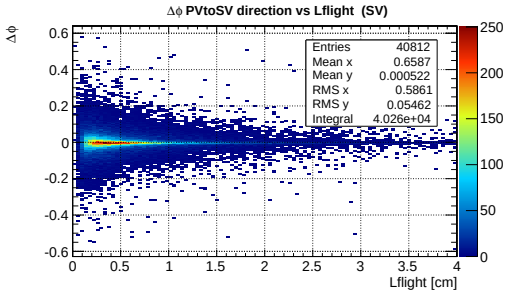

(b) $\Delta\phi^{sv}$ *vs Lflight.*

Figure 5.2: $\Delta\eta^{sv}$ and $\Delta\phi^{sv}$ distributions, they are only in presence of SV. They don't depend on the presence of the muon inside jet.

It's possible to select for $\Delta\eta^{jet}$ and $\Delta\phi^{jet}$ the cases in which the SV is present.

In this case we expect that the resolution is better than the case with all the events. We plot this case in Figure 5.3.

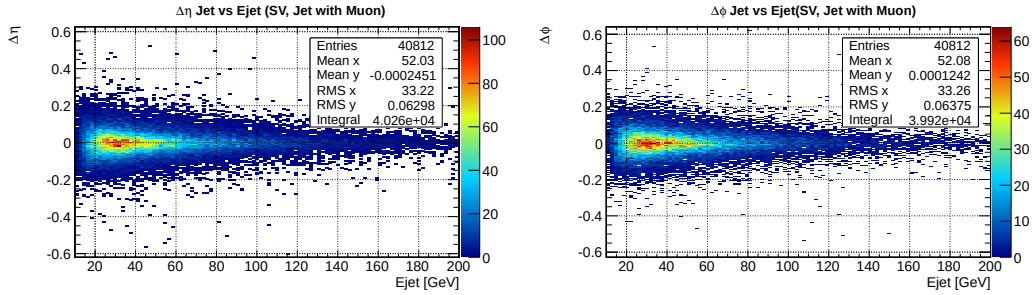

(a) $\Delta\eta^{jet}$ *vs Ejet, Jet with muon.* (b) $\Delta\phi^{jet}$ *vs Ejet, Jet with muon.*

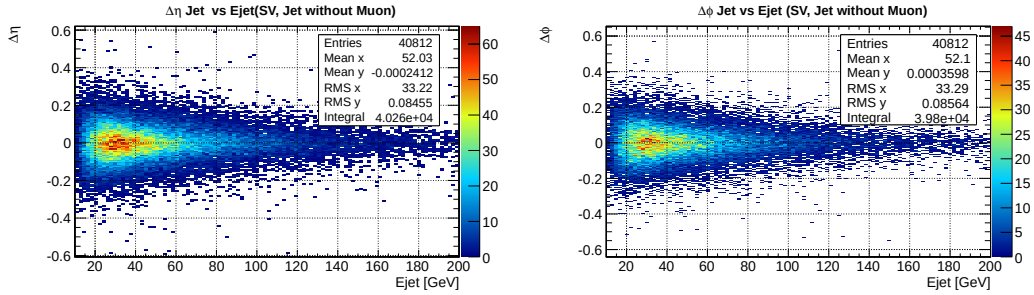

(c) $\Delta\eta^{jet}$ *vs Ejet, Jet without muon.* (d) $\Delta\phi^{jet}$ *vs Ejet, Jet without muon.*

Figure 5.3: $\Delta\eta^{jet}$ and $\Delta\phi^{jet}$ distributions for the case in presence of SV.

To get an idea of the value of the resolution in all these cases we can project the previous plots in one-dimensional plots, then we can take the RMS widths and compare them. It's only a rough estimation of the resolution but for our purposes it's sufficient because now we are only concerned that the distributions follow our predictions.

In Figure 5.4 and 5.5 we report the one-dimensional distributions. In Table 5.1 the RMS widths are reported.

	ALL		**SV**	
	RMS $\Delta\eta$	RMS $\Delta\phi$	RMS $\Delta\eta$	RMS $\Delta\phi$
Jet with muon	0.089	0.088	0.063	0.064
Jet without muon	0.109	0.104	0.084	0.086
Flight direction	-	-	0.054	0.055
Flight direction (cut at 0.75 cm)	-	-	0.043	0.045

Table 5.1: RMS widths for the case with all the event and in presence of SV.

As expected (table 5.1) the RMS values are smaller for jet with the muon momentum inside respect to outside. Another consideration is that resolutions are better if we consider the events in presence of SV, i.e. for events with a reconstructed SV (this is because efficiency reconstruction increases for larger jet energy).

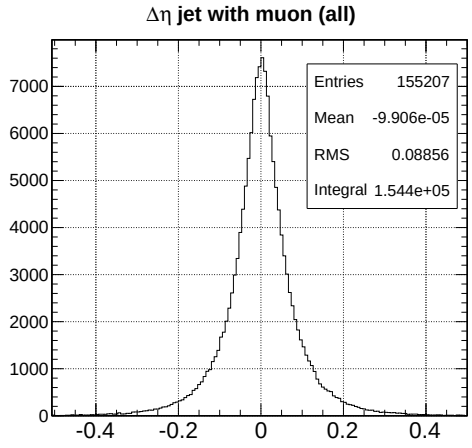

(a) $\Delta\eta^{jet}$, *Jet with muon.*

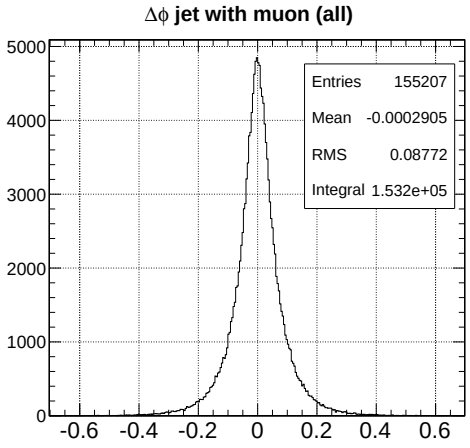

(b) $\Delta\phi^{jet}$, *Jet with muon.*

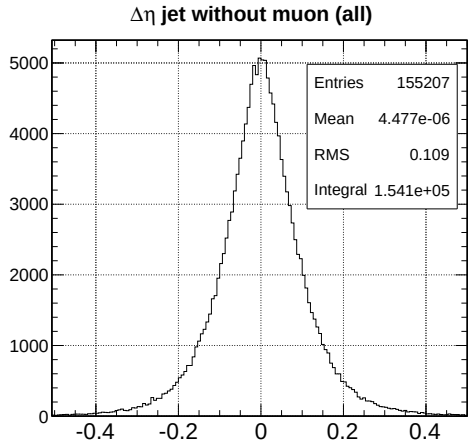

(c) $\Delta\eta^{jet}$, *Jet without muon.*

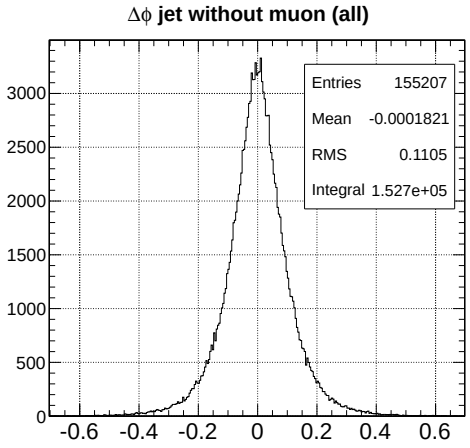

(d) $\Delta\phi^{jet}$, *Jet without muon.*

Figure 5.4: $\Delta\eta^{jet}$ and $\Delta\phi^{jet}$ one-dimensional distributions for the case with all the events.

Finally we can see that the resolutions for the PVtoSV direction (flight direction) are better then the others. In this case we have also applicated a cut, choosing events with $Lfligth > 0.75$ cm and reported it in the table 5.1. The resolution in this case is better, as we expect because the efficiency of SV reconstruction increases for larger flight lenght.

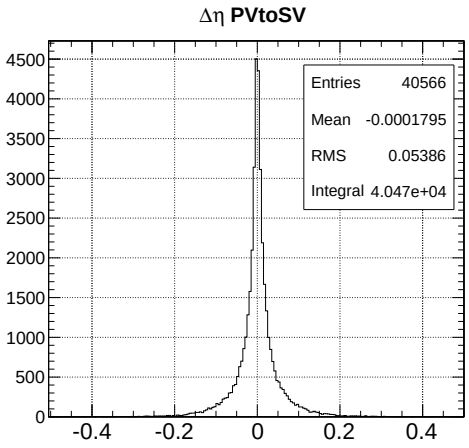

(a) $\Delta\eta^{sv}$, 1D distribution.

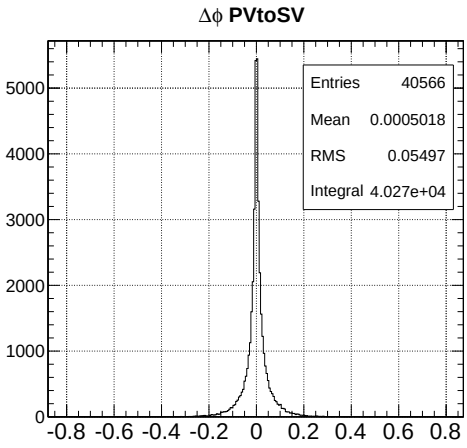

(b) $\Delta\phi^{sv}$, 1D distribution.

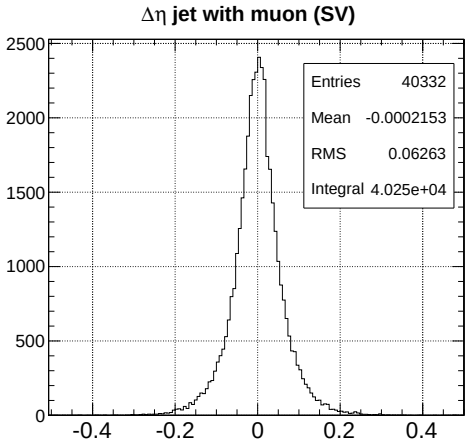

(c) $\Delta\eta^{jet}$, *Jet with muon.*

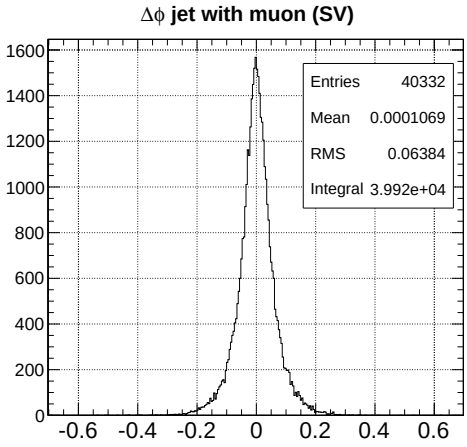

(d) $\Delta\phi^{jet}$, *Jet with muon.*

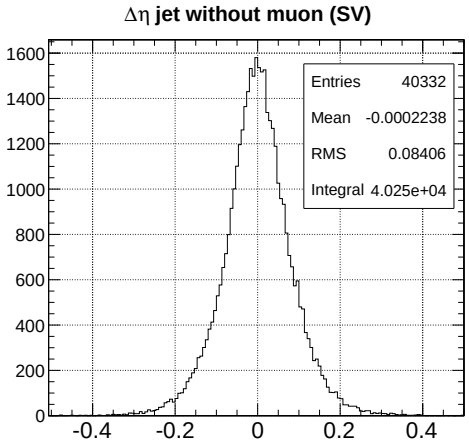

(e) $\Delta\eta^{jet}$, *Jet without muon.*

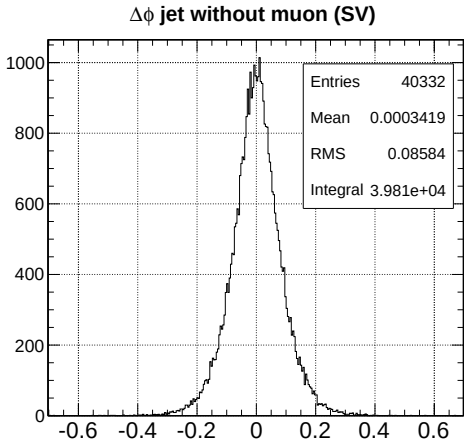

(f) $\Delta\phi^{jet}$, *Jet without muon.*

Figure 5.5: One-dimensional distributions for the case in presence of SV

5.2.3 New definitions for the analysis of real data.

The previous definitions of $\Delta\eta$ and $\Delta\phi$ were suitable only for a MC sample, because we don't know the real direction of the decaying hadron in a real data sample. However we can reconstruct the decay vertices and determine the flight direction (PVtoSV direction). We also know the jet momentum (and the muon momentum), so we know its axis. At this point we can define, in analogy with previous definitions, new $\Delta\eta$ and $\Delta\phi$, this time for MC and real data events:

$$\Delta\eta = \eta^{jet} - \eta^{sv}; \tag{5.1}$$

$$\Delta\phi = \phi^{jet} - \phi^{sv}. \tag{5.2}$$

Also in this case we consider jet direction with or without the muon momentum; the presence of SV is necessary in all the cases. In this section we analyze the MC distributions for $\Delta\eta$ and $\Delta\phi$, then we will proceed with data. This time we plot the distribution of $\Delta\eta$ and $\Delta\phi$ as a function of jet energy or length flight. We start in Figure 5.6 with the case of muon momentum inside the jet momentum.

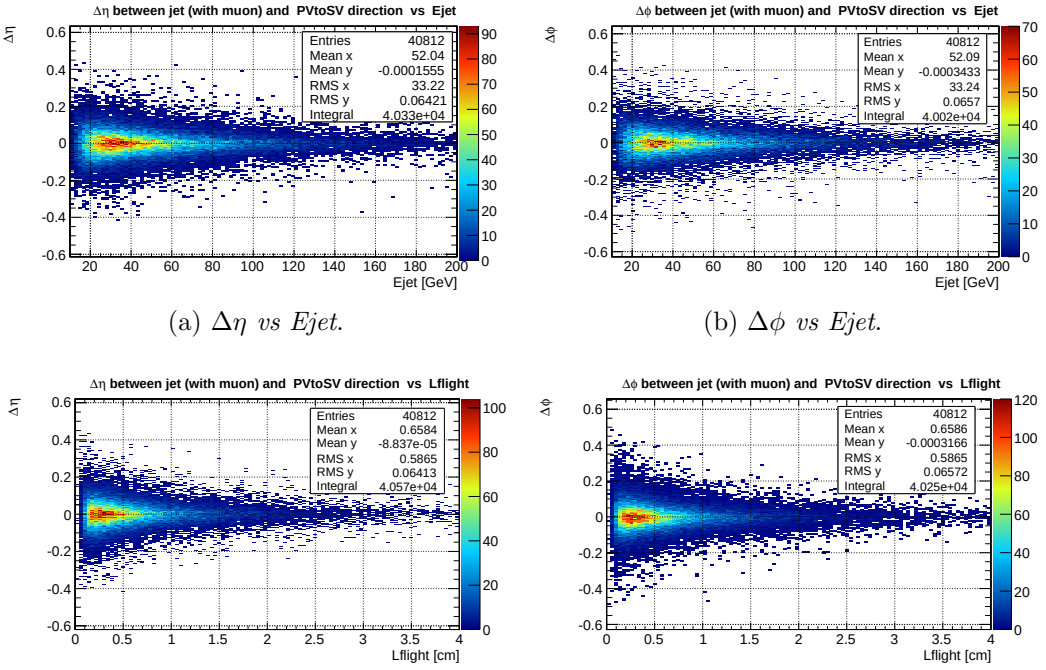

(a) $\Delta\eta$ *vs Ejet.* (b) $\Delta\phi$ *vs Ejet.*

(c) $\Delta\eta$ *vs Lflight.* (d) $\Delta\phi$ *vs Lflight.*

Figure 5.6: $\Delta\eta$ and $\Delta\phi$ distributions for jet with muon.

Plots are as expected, at high jet energy or length flight the resolution improves. We plot the 1D-distribution to evaluate the RMS (Figure 5.7).

For MC sample it's possible to separate muons from the decay $B \to \mu X$, that we define muons of class 1, from the other decays like $B \to C \to \mu X$ or $C \to \mu X$ and others that we have already defined. We can do the previous analysis for class 1 muons, see Figure 5.8 and Figure 5.9.

We repeat the same analysis for the case in which muon momentum is subtracted from jet momentum (case *jet without muon*). We begin with the distributions of $\Delta\eta$ and $\Delta\phi$ for all the events (always in presence of SV because the

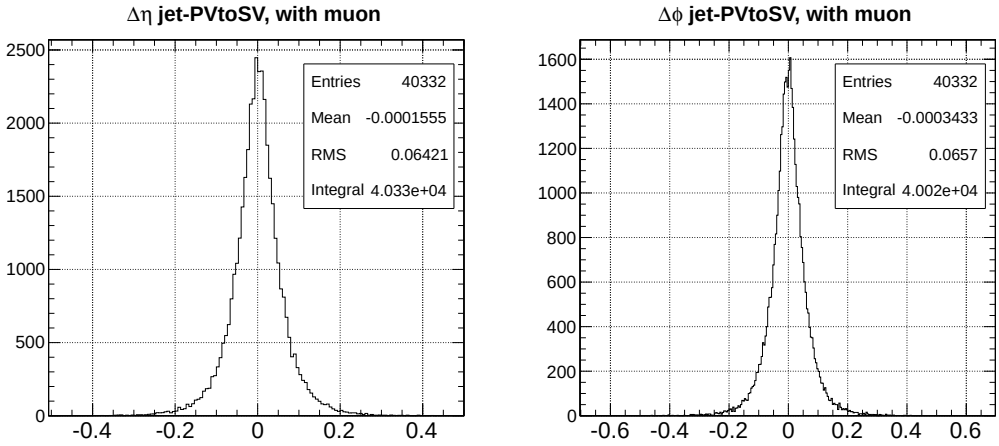

(a) $\Delta\eta$, *1D distribution.* (b) $\Delta\phi$, *1D distribution.*

Figure 5.7: $\Delta\eta$ and $\Delta\phi$ 1D distributions for jet with muon.

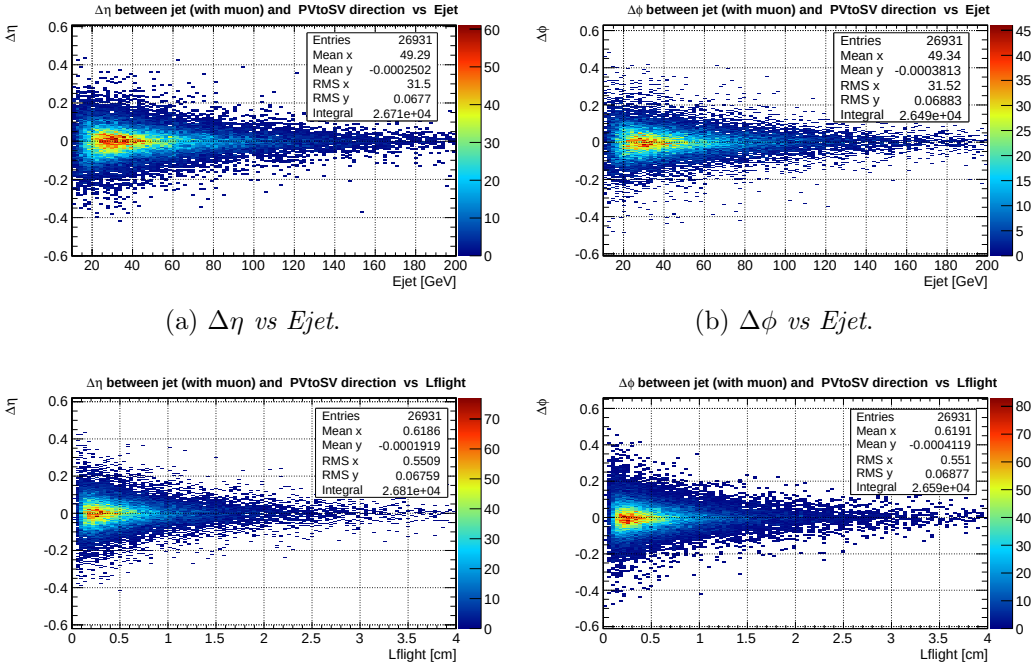

(a) $\Delta\eta$ *vs Ejet.* (b) $\Delta\phi$ *vs Ejet.*

(c) $\Delta\eta$ *vs Lflight.* (d) $\Delta\phi$ *vs Lflight.*

Figure 5.8: $\Delta\eta$ and $\Delta\phi$ distributions for jet with muon, **class 1 muons**.

definitions of $\Delta\eta$ and $\Delta\phi$) in Figure 5.10 and 5.11. Then we pass to the case of class 1 muons, Figure 5.12 and 5.13.

We summarize these results in the Table 5.2 .

Only one consideration about this table: the RMS widths are always greater in the case of muon from class 1.

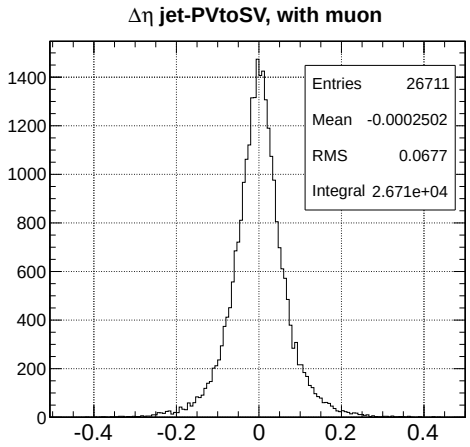

(a) $\Delta\eta$, *1D distribution.*

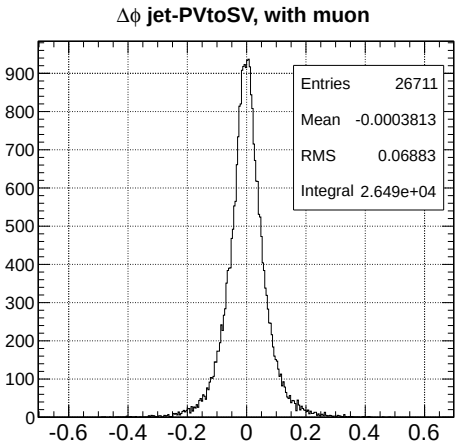

(b) $\Delta\phi$, *1D distribution.*

Figure 5.9: $\Delta\eta$ and $\Delta\phi$ 1D distributions for jet with muon, **class 1 muons**.

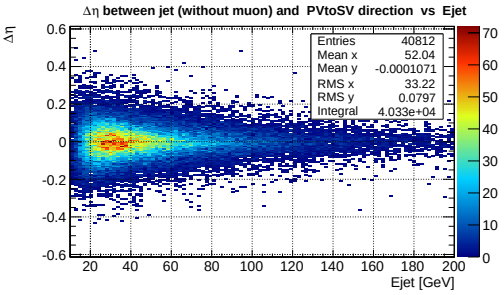

(a) $\Delta\eta$ *vs Ejet.*

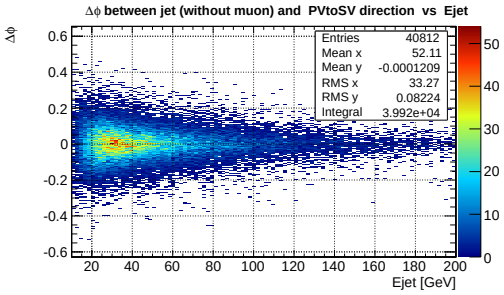

(b) $\Delta\phi$ *vs Ejet.*

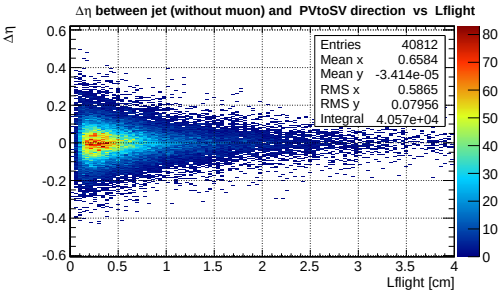

(c) $\Delta\eta$ *vs Lflight.*

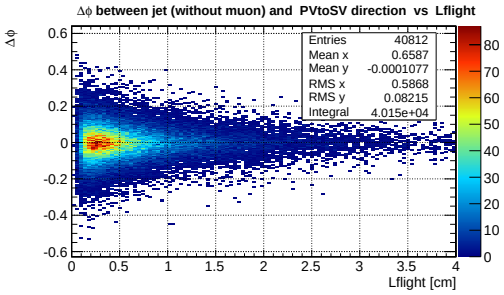

(d) $\Delta\phi$ *vs Lflight.*

Figure 5.10: $\Delta\eta$ and $\Delta\phi$ distributions for jet without muon.

	ALL		**Class 1**	
	RMS $\Delta\eta$	RMS $\Delta\phi$	RMS $\Delta\eta$	RMS $\Delta\phi$
Jet with muon	0.0642	0.0657	0.0677	0.0688
Jet without muon	0.0797	0.0822	0.0847	0.0872

Table 5.2: RMS values for $\Delta\eta$ and $\Delta\phi$ distributions.

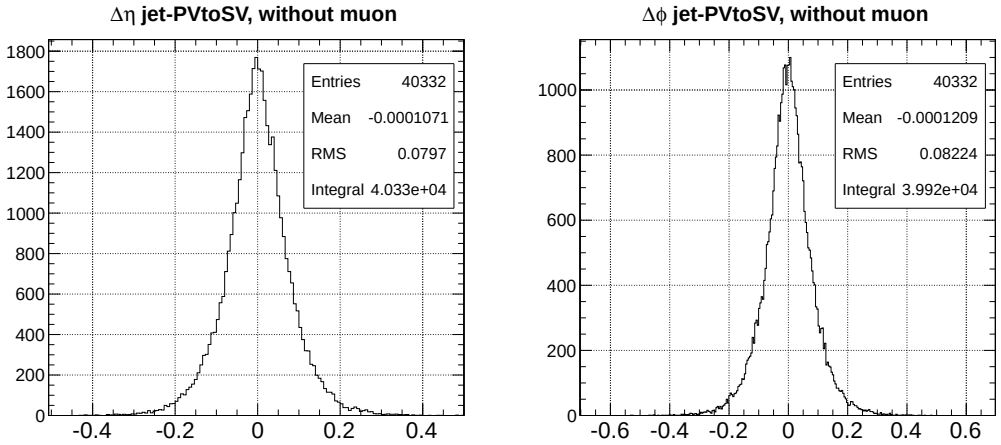

(a) $\Delta\eta$, *1D distribution.* (b) $\Delta\phi$, *1D distribution.*

Figure 5.11: $\Delta\eta$ and $\Delta\phi$ 1D distributions for jet without muon.

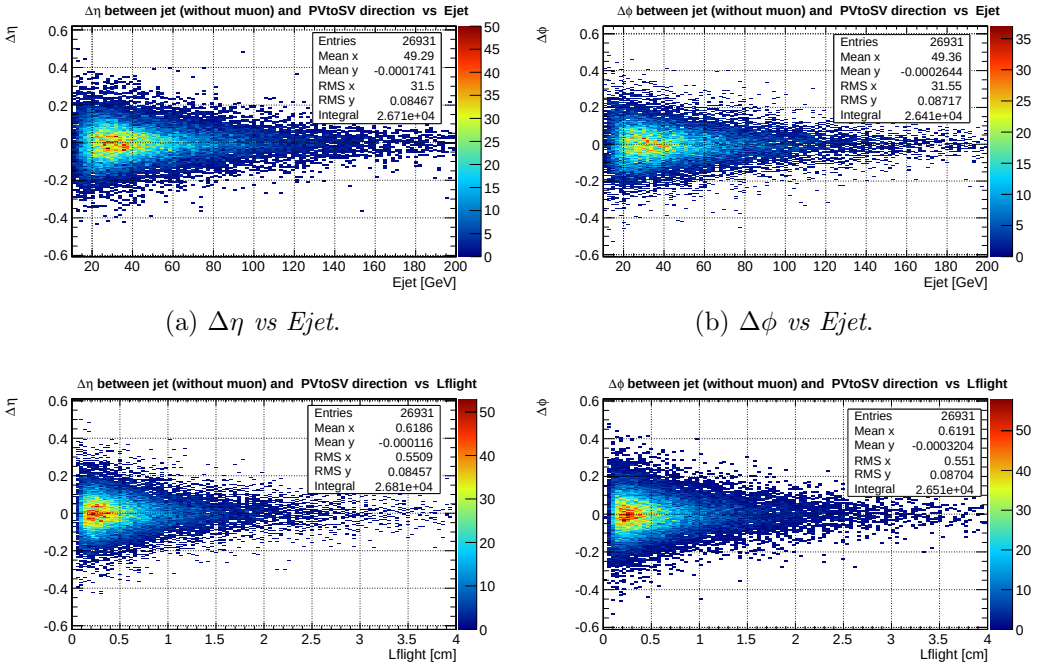

(a) $\Delta\eta$ *vs Ejet.* (b) $\Delta\phi$ *vs Ejet.*

(c) $\Delta\eta$ *vs Lflight.* (d) $\Delta\phi$ *vs Lflight.*

Figure 5.12: $\Delta\eta$ and $\Delta\phi$ distributions for jet without muon, **class 1 muons**.

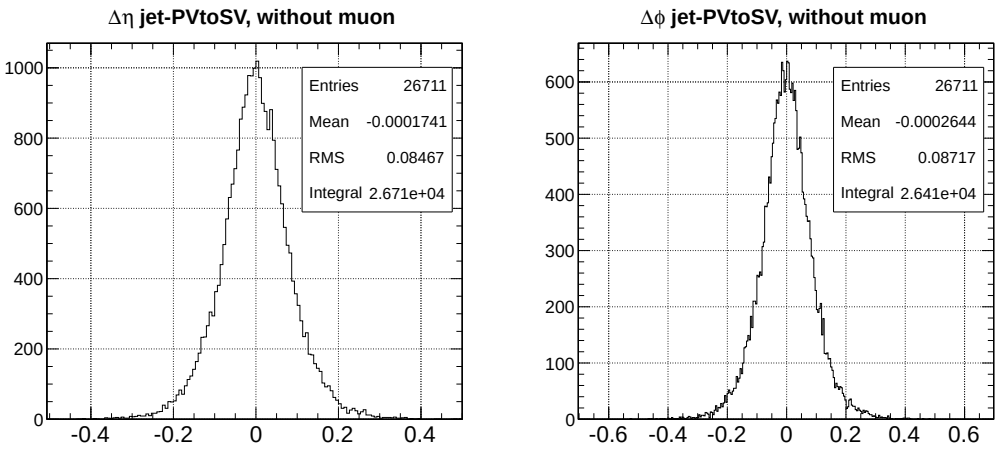

(a) $\Delta\eta$, *1D distribution.* (b) $\Delta\phi$, *1D distribution.*

Figure 5.13: $\Delta\eta$ and $\Delta\phi$ 1D distributions for jet without muon, **class 1 muons**.

5.2.4 Some checks

Now we are interested into the distributions of muons from class 1 in our MC sample, with the aim to verify the presence of any anomalies. We take the distributions in presence of SV and in the case of the class 1 muons, then we compare it and calculate the percentage of muon from class 1 as a function of *Lflight* (Figure 5.14).

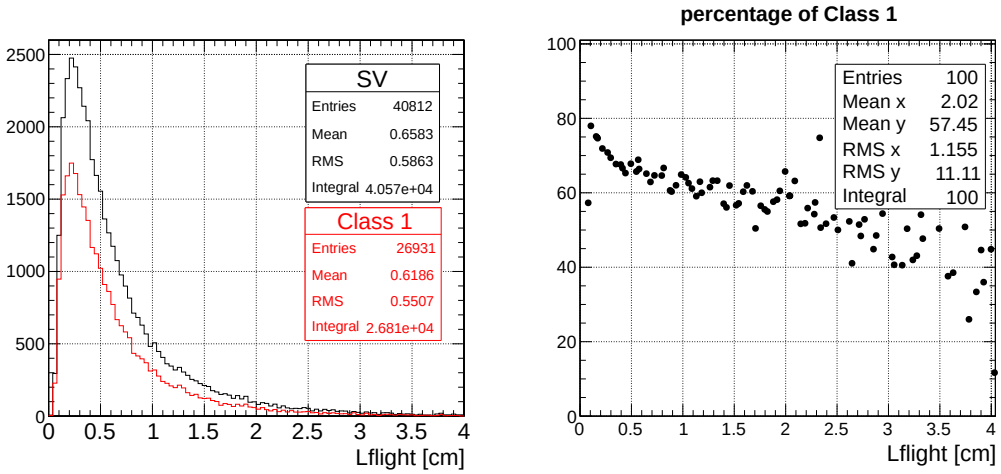

(a) Comparison between SV and class 1 distributions on Lflight.

(b) Percentage of class1 on Lflight.

Figure 5.14: Comparison SV-class1 for Lflight

The most interesting check is the p_T^{out} distribution. We can see it in Figure 5.15.

We now compare the case SV and class 1 in Figure 5.16. As we can see the class 1 distribution has a higher mean , this because muons from direct B hadron decay have a higher momentum. The percentage of class 1 muons is about 90 % from about 2 GeV forward.

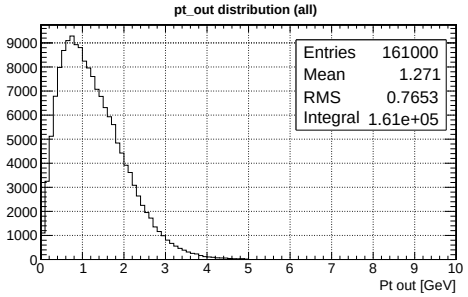

(a) Case with all the events.

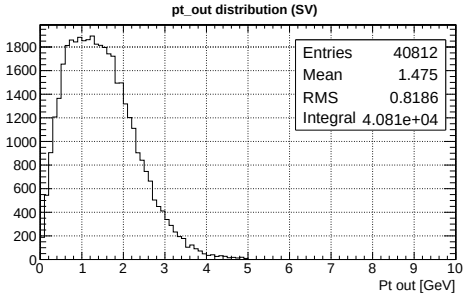

(b) Case in presence of SV.

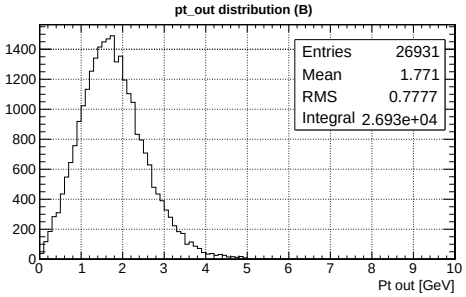

(c) Class 1 case.

Figure 5.15: Distribution of p_T^{out} for MC sample.

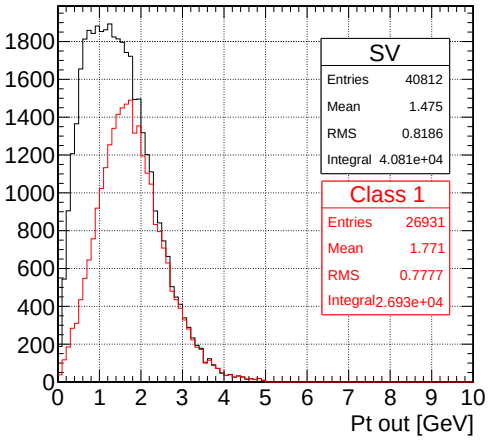

(a) Comparison between SV and class 1 distributions on p_{out}^t.

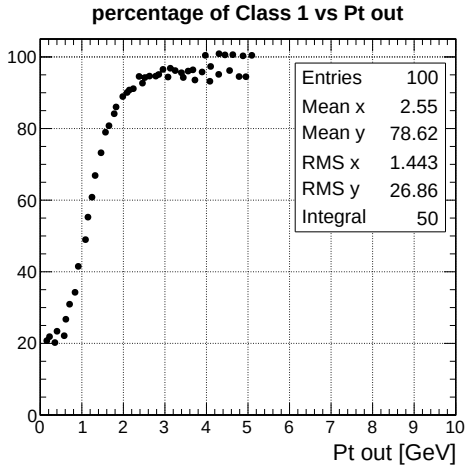

(b) Percentage of class1 on p_T^{out}.

Figure 5.16: Comparison SV-class1 for p_T^{out}

5.3 Real data analysis

Defined $\Delta\eta$ and $\Delta\phi$ as in (5.1) and (5.2), we can repeat the previous analysis for a sample of real data from November 2010. Initially we take the case with muon momentum inside jet momentum. In Figure 5.17 we plot the resolutions $\Delta\eta$ and $\Delta\phi$ and their 1D projections in Figure 5.18.

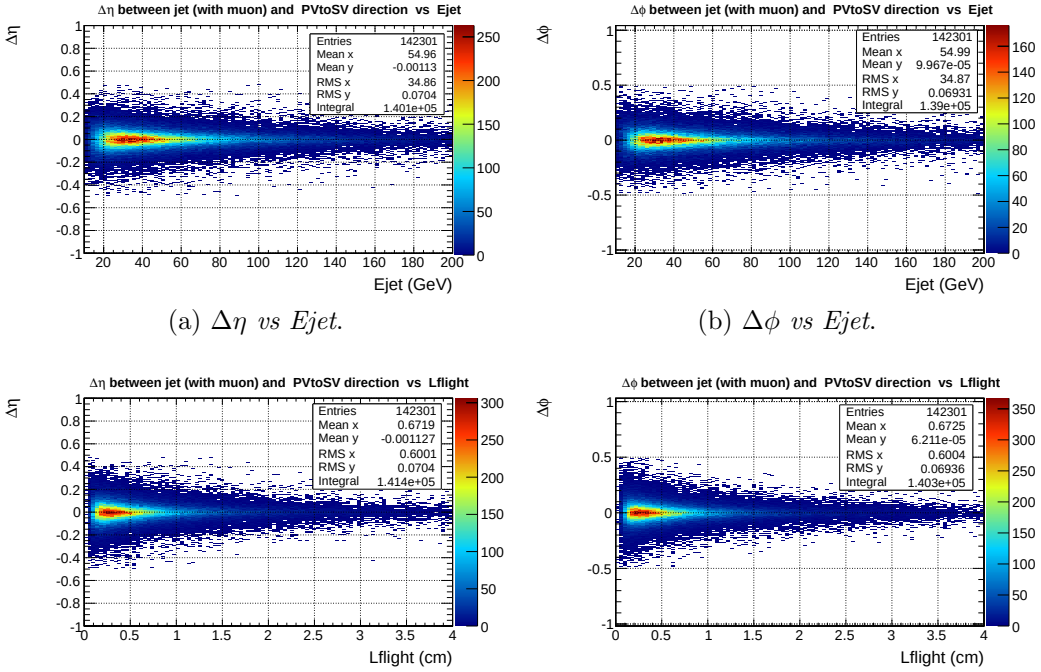

(a) $\Delta\eta$ *vs Ejet.* (b) $\Delta\phi$ *vs Ejet.*

(c) $\Delta\eta$ *vs Lflight.* (d) $\Delta\phi$ *vs Lflight.*

Figure 5.17: $\Delta\eta$ and $\Delta\phi$ distributions for jet with muon, **data 2010**.

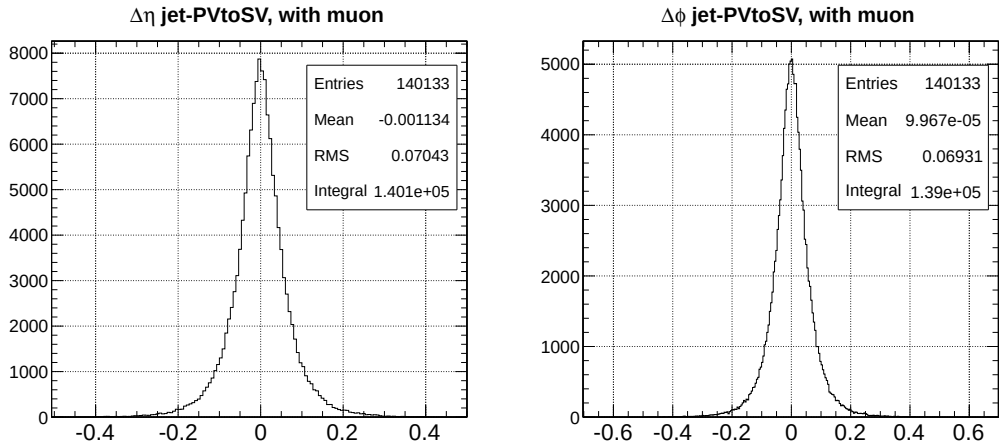

(a) $\Delta\eta$, *1D distribution.* (b) $\Delta\phi$, *1D distribution.*

Figure 5.18: $\Delta\eta$ and $\Delta\phi$ 1D distributions for jet with muon, **data 2010**.

Then we plot in Figure 5.19 and 5.20 the same variables but for the case of muon momentum subtracted from jet momentum. In Table 5.3 we can summarize

the RMS widths for MC and real data, obviously RMS values for class 1 in MC haven't a corrispondence with data.

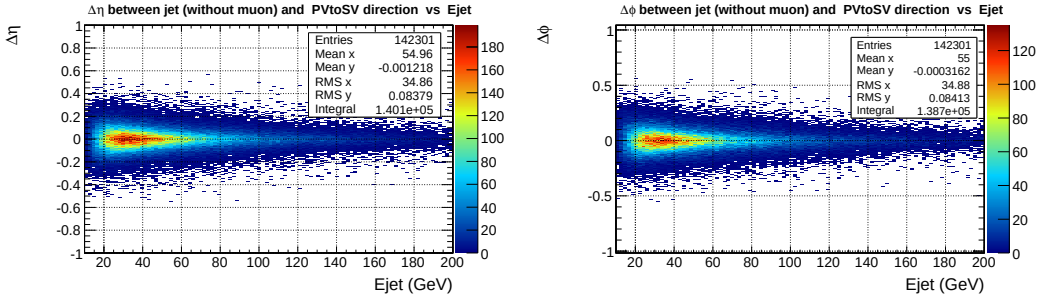

(a) $\Delta\eta$ *vs Ejet.* (b) $\Delta\phi$ *vs Ejet.*

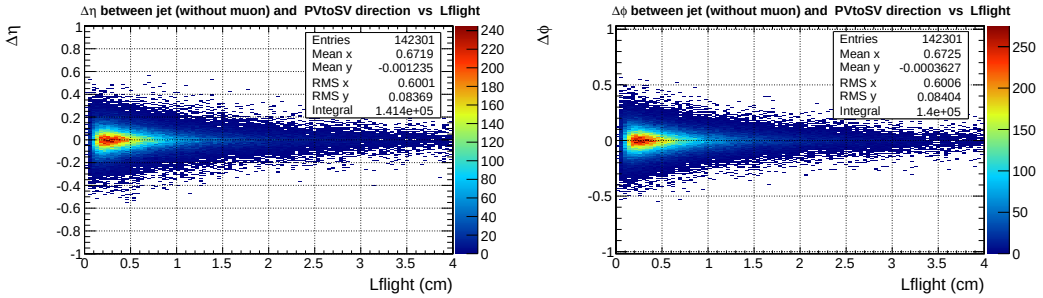

(c) $\Delta\eta$ *vs Lflight.* (d) $\Delta\phi$ *vs Lflight.*

Figure 5.19: $\Delta\eta$ and $\Delta\phi$ distributions for jet without muon, **data 2010**.

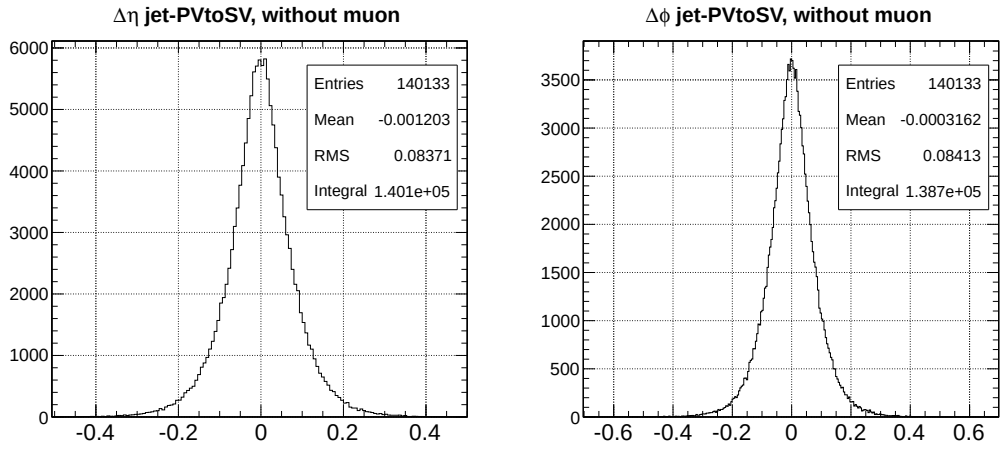

(a) $\Delta\eta$, *1D distribution.* (b) $\Delta\phi$, *1D distribution.*

Figure 5.20: $\Delta\eta$ and $\Delta\phi$ 1D distributions for jet without muon, **data 2010**.

Also in this case real data have a greater RMS, as we expected. As a control on our sample we can see the p_T^{out} distributions for all muons and for muons in presence of SV, see Figure 5.21.

Now we are interested to evaluate the smearing (i.e. the differences in resolutions) between data and MC. We take the plots of the resolution $\Delta\eta$ and $\Delta\phi$

	Jet with muon		Jet without muon	
	RMS $\Delta\eta$	RMS $\Delta\phi$	RMS$\Delta\eta$	RMS $\Delta\phi$
MC	0.0642	0.0657	0.0797	0.0822
DATA 2010	0.0704	0.0693	0.0837	0.0841
MC class 1	0.0677	0.0688	0.0847	0.0872

Table 5.3: RMS values for MC and Data 2010.

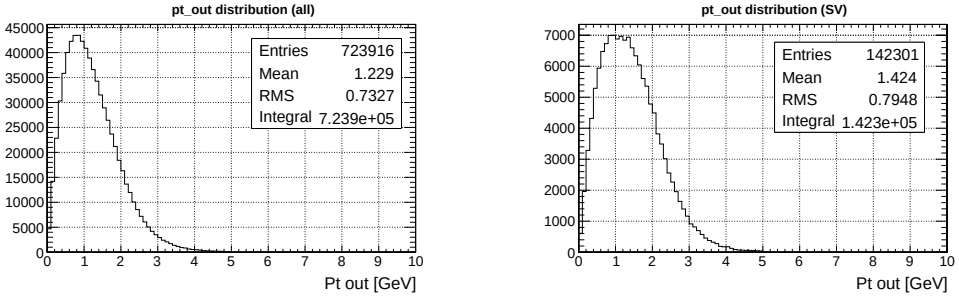

(a) *All muons.* (b) *Muons in presence of SV.*

Figure 5.21: The p_T^{out} distributions. As in the MC case p_T^{out} is larger for the second case.

as a function of the jet energy for MC and data in the case of *jet with muon*, Figure 5.6a, 5.6b, 5.17a and 5.17b. We separate the distributions in four regions of energy. The energy ranges are [10; 19.5] GeV, [19.5; 29] GeV, [29; 49.9] GeV and [49.9; 200] GeV. We fit the histograms with a sum of two Gaussian functions; in principle the fit function can be expressed by

$$f(x) = N\left[\frac{f}{\sigma_1\sqrt{2\pi}}\ e^{-\frac{1}{2}\left(\frac{x-\mu}{\sigma_1}\right)^2} + \frac{1-f}{\sigma_2\sqrt{2\pi}}\ e^{-\frac{1}{2}\left(\frac{x-\mu}{\sigma_2}\right)^2}\right]. \tag{5.3}$$

where f is the fraction of events under one Gaussian function. In this case we define an overall σ

$$\sigma = \sqrt{f\ {\sigma_1}^2 + (1-f)\ {\sigma_2}^2}. \tag{5.4}$$

That leads

$$f = \frac{\sigma^2 - {\sigma_2}^2}{{\sigma_1}^2 - {\sigma_2}^2}. \tag{5.5}$$

At this point we extract σ directly from the fit:

$$f(x) = N\left[\frac{\sigma^2 - {\sigma_2}^2}{{\sigma_1}^2 - {\sigma_2}^2}\frac{1}{\sigma_1\sqrt{2\pi}}\ e^{-\frac{1}{2}\left(\frac{x-\mu}{\sigma_1}\right)^2} + \frac{{\sigma_1}^2 - \sigma^2}{{\sigma_1}^2 - {\sigma_2}^2}\frac{1}{\sigma_2\sqrt{2\pi}}\ e^{-\frac{1}{2}\left(\frac{x-\mu}{\sigma_2}\right)^2}\right]. \tag{5.6}$$

It has 5 free parameters:

- N is the normalization,
- μ the mean of two Gaussian functions,

- ${\sigma_1}^2$ and ${\sigma_2}^2$ variances of the Gaussian functions,
- σ^2 is the overall variance of the sum of two Gaussian functions.

We use a likelihood fit for each region. From Figure 5.22 to Figure 5.25 we can see fit and residual plots for $\Delta\eta$ and $\Delta\phi$ in MC and data samples.

Similarly we can plot for the case of *jet without muon* (from Figure 5.26 to 5.29).

Fits are not bad for our purposes, there are some discrepancies only near the mean as we can see in residual plots. We can define the smearing as

$$s = \sqrt{{\sigma_{Data}}^2 - {\sigma_{MC}}^2}. \tag{5.7}$$

Now we summarize all in tables 5.4, 5.5, 5.6 and 5.7 for all the cases.

Energy range [GeV]	$\sigma_{Data} \cdot 10^{-4}$	$\sigma_{MC} \cdot 10^{-4}$	$\mathbf{s}\cdot 10^{-4}$
[10; 19.5]	1011 ±9	921 ±14	417 ±38
[19.5; 29]	795 ±5	714 ±9	350 ±22
[29; 49.9]	684 ±3	630 ±6	266 ±16
[49.9; 200]	616 ±3	537 ±5	302 ±11

Table 5.4: Case *jet with muon*, $\Delta\eta$.

Energy range [GeV]	$\sigma_{Data} \cdot 10^{-4}$	$\sigma_{MC} \cdot 10^{-4}$	$\mathbf{s}\cdot 10^{-4}$
[10; 19.5]	975 ±10	948 ±16	228 ±79
[19.5; 29]	776 ±6	730 ±9	263 ±31
[29; 49.9]	671 ±3	635 ±6	217 ±20
[49.9; 200]	616 ±3	559 ±5	259 ±13

Table 5.5: Case *jet with muon*, $\Delta\phi$.

Energy range [GeV]	$\sigma_{Data} \cdot 10^{-4}$	$\sigma_{MC} \cdot 10^{-4}$	$\mathbf{s}\cdot 10^{-4}$
[10; 19.5]	1165 ±10	1106 ±16	366 ±58
[19.5; 29]	961 ±5	907 ±9	318 ±30
[29; 49.9]	824 ±3	784 ±6	254 ±21
[49.9; 200]	723 ±3	664 ±5	286 ±14

Table 5.6: Case *jet without muon*, $\Delta\eta$.

We can see from tables that σ_{Data} is always larger than σ_{MC}, as we expected from definition (5.7).

Energy range [GeV]	$\sigma_{Data} \cdot 10^{-4}$	$\sigma_{MC} \cdot 10^{-4}$	$\mathbf{s} \cdot 10^{-4}$
[10; 19.5]	1158± 10	1147± 17	159± 142
[19.5; 29]	962± 5	944± 10	185± 57
[29; 49.9]	827± 3	794± 6	231± 23
[49.9; 200]	732± 3	694± 6	233± 20

Table 5.7: Case *jet without muon*, $\Delta\phi$.

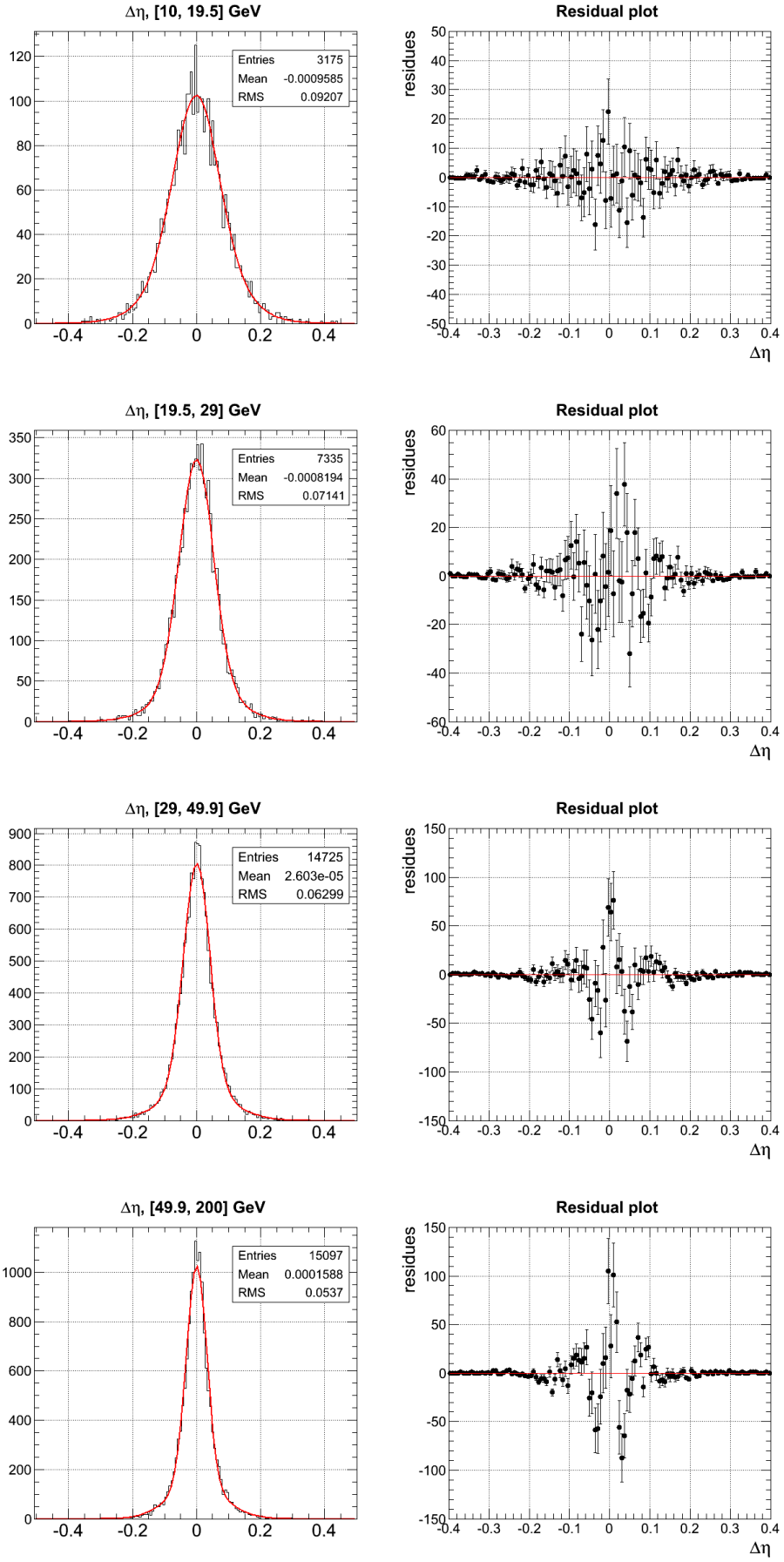

Figure 5.22: Fits and residual plots for $\Delta\eta$ for jet with muon, **MC**.

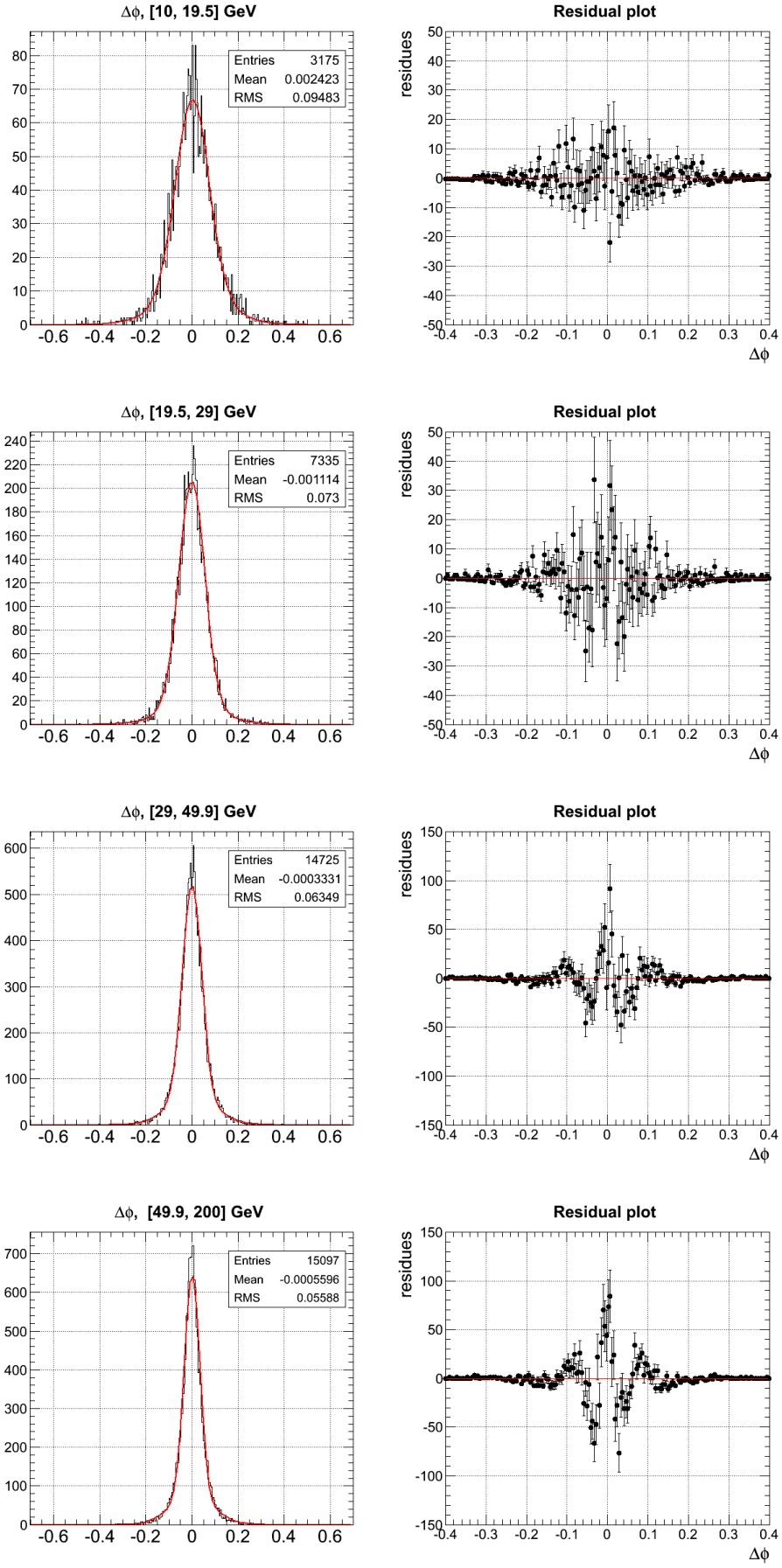

Figure 5.23: Fits and residual plots for $\Delta\phi$ for jet with muon, **MC**.

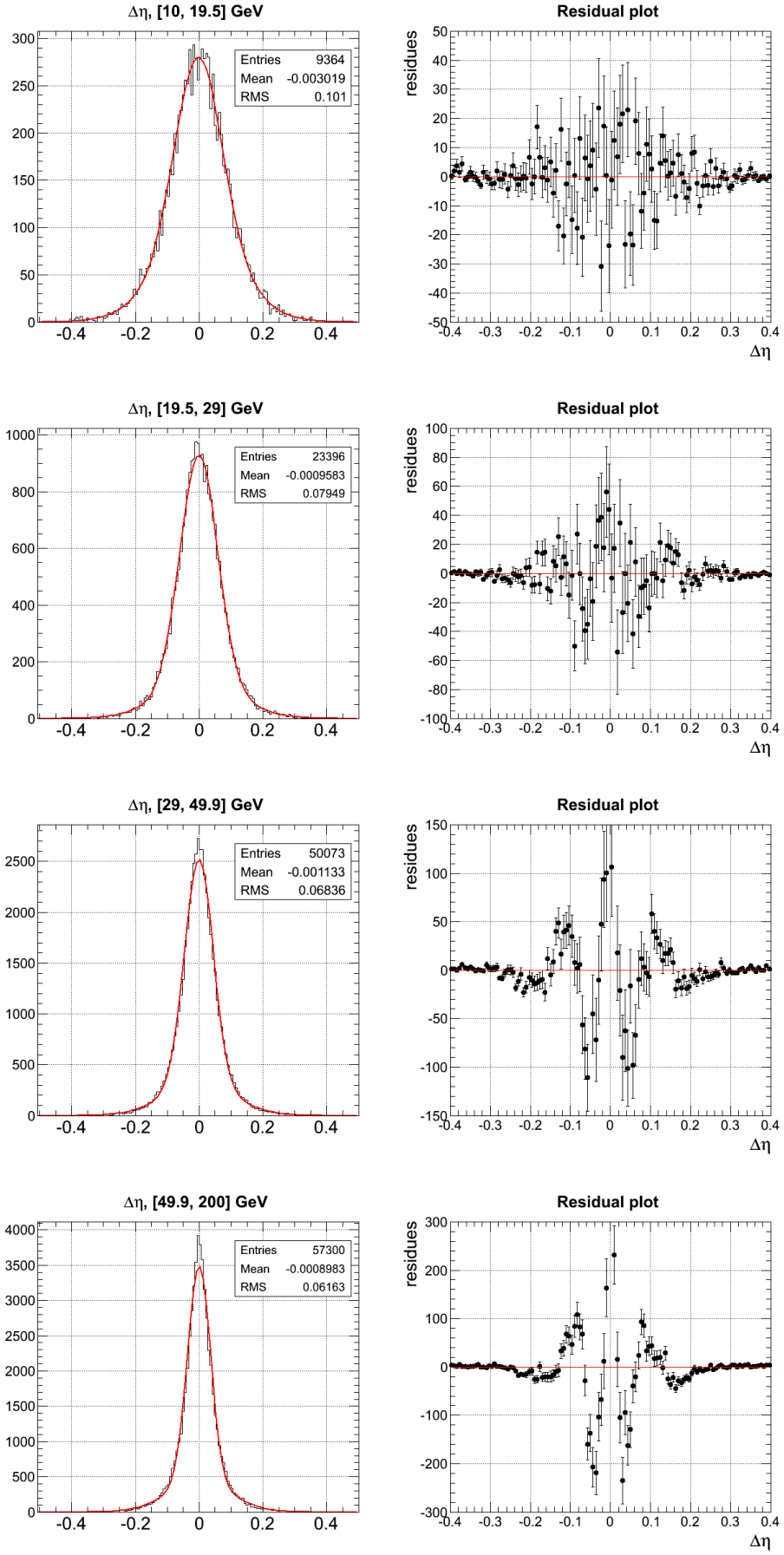

Figure 5.24: Fits and residual plots for $\Delta\eta$ for jet with muon, **Data 2010**.

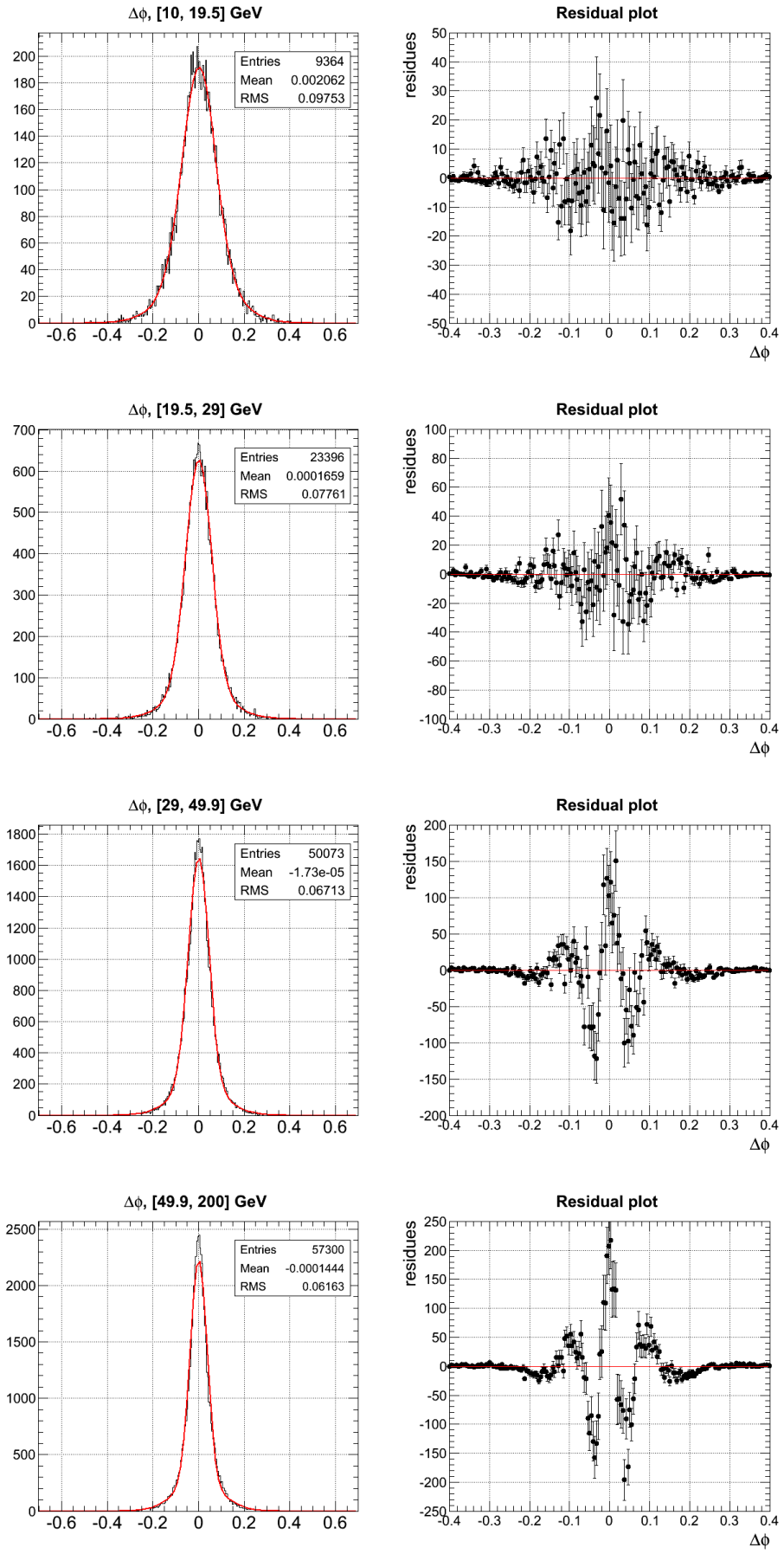

Figure 5.25: Fits and residual plots for $\Delta\phi$ for jet with muon, **Data 2010**.

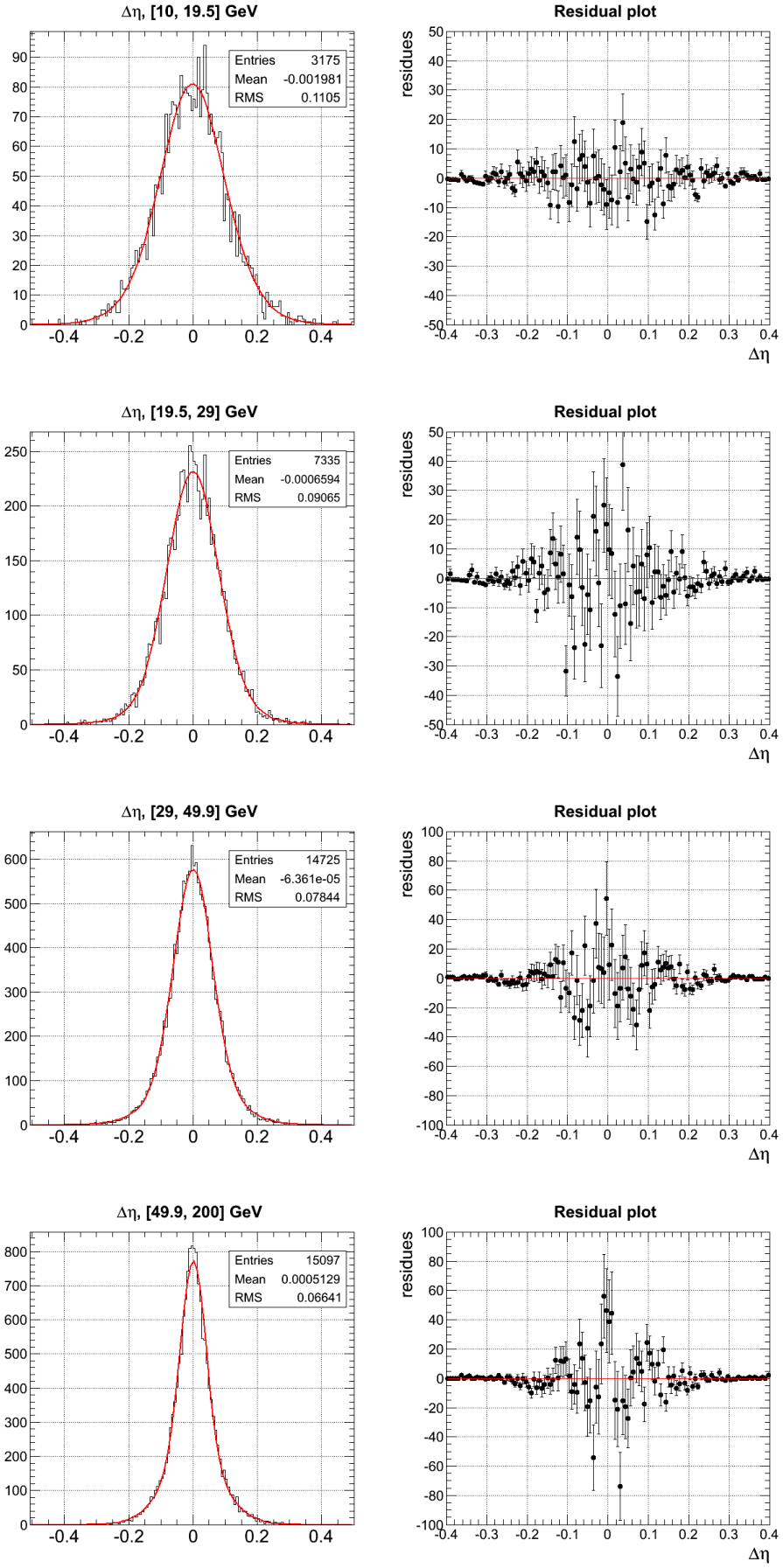

Figure 5.26: Fits and residual plots for $\Delta\eta$ for jet without muon, **MC**.

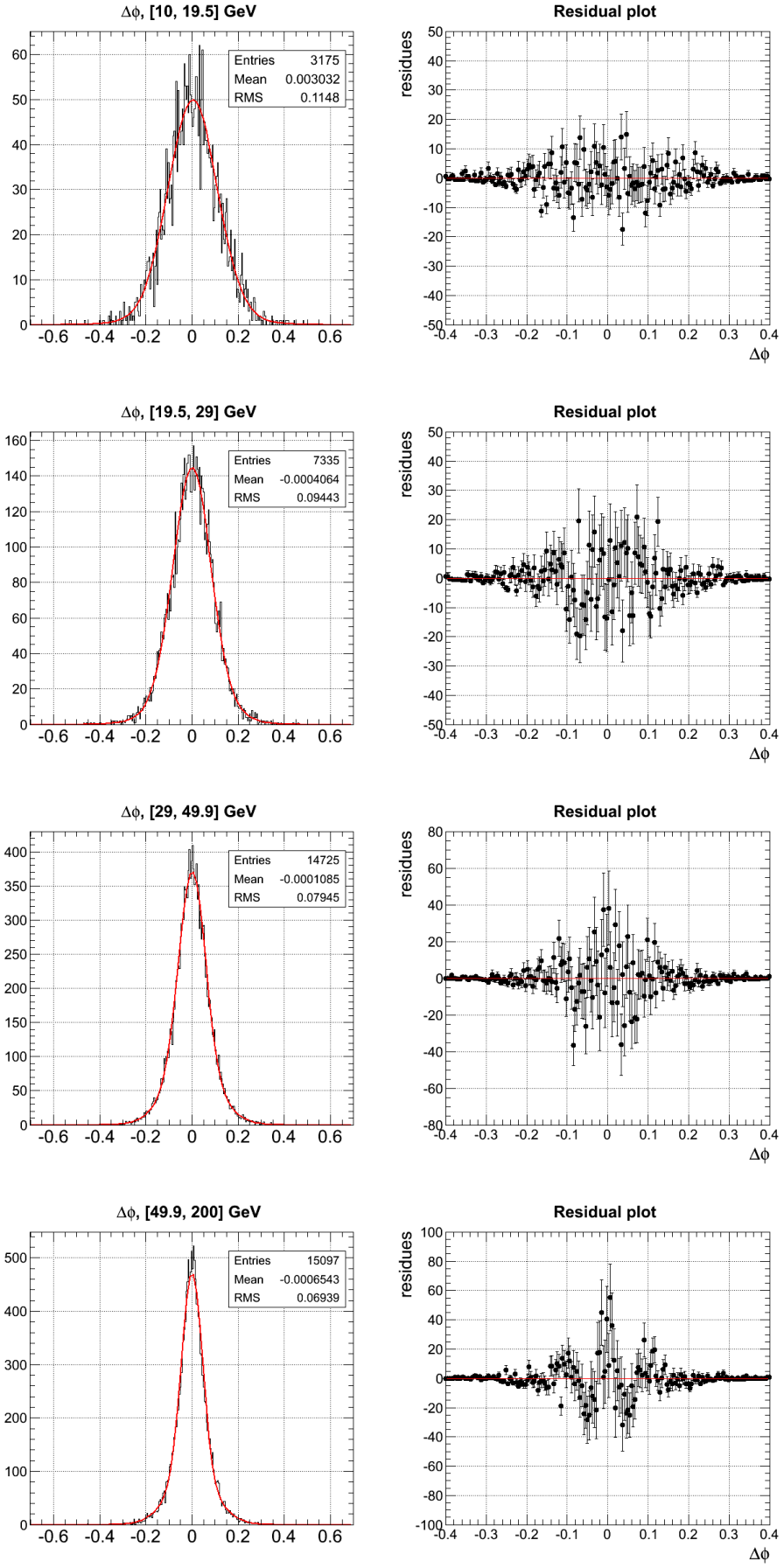

Figure 5.27: Fits and residual plots for $\Delta\phi$ for jet without muon, **MC**.

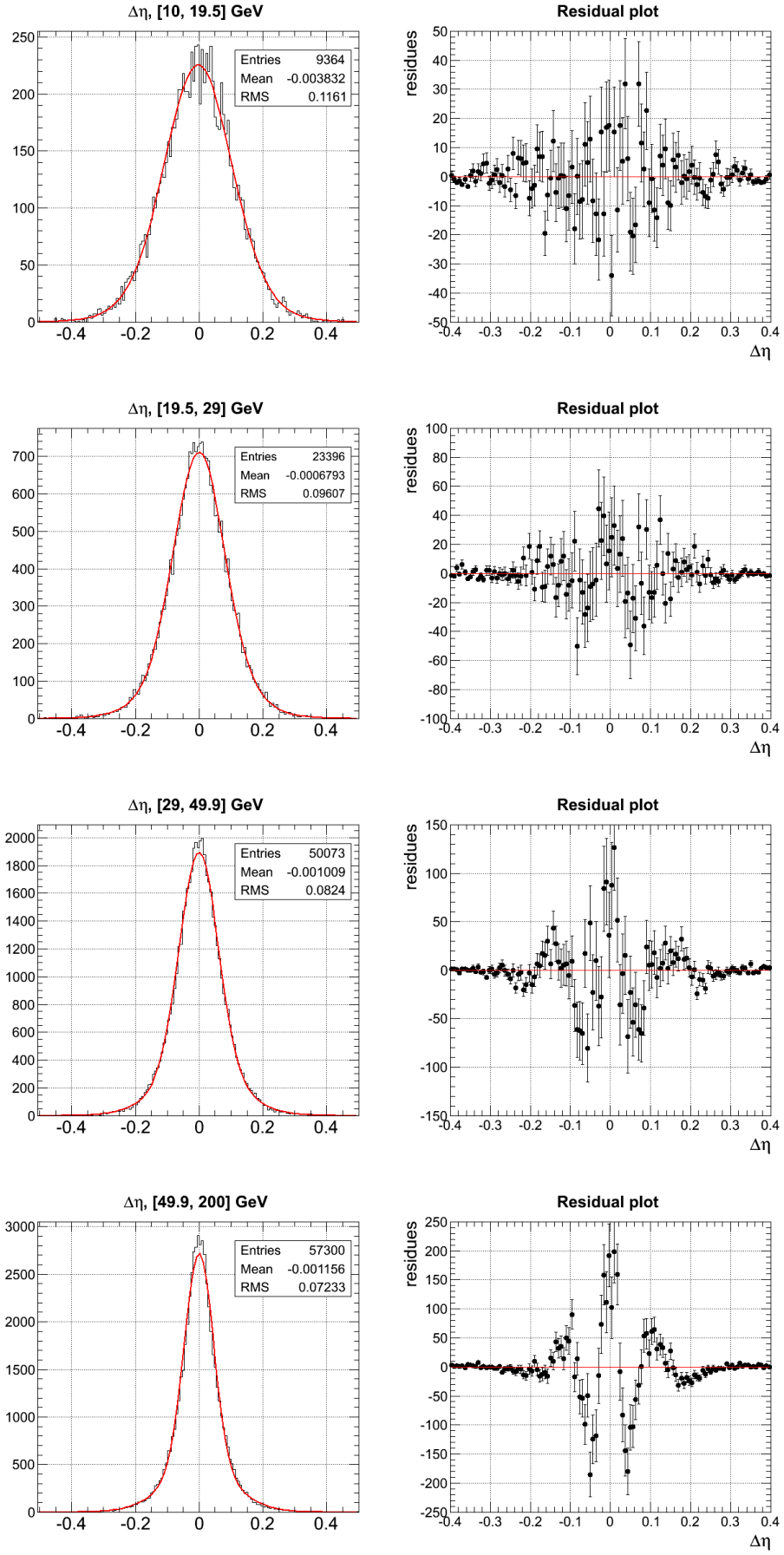

Figure 5.28: Fits and residual plots for $\Delta\eta$ for jet without muon, **Data 2010**.

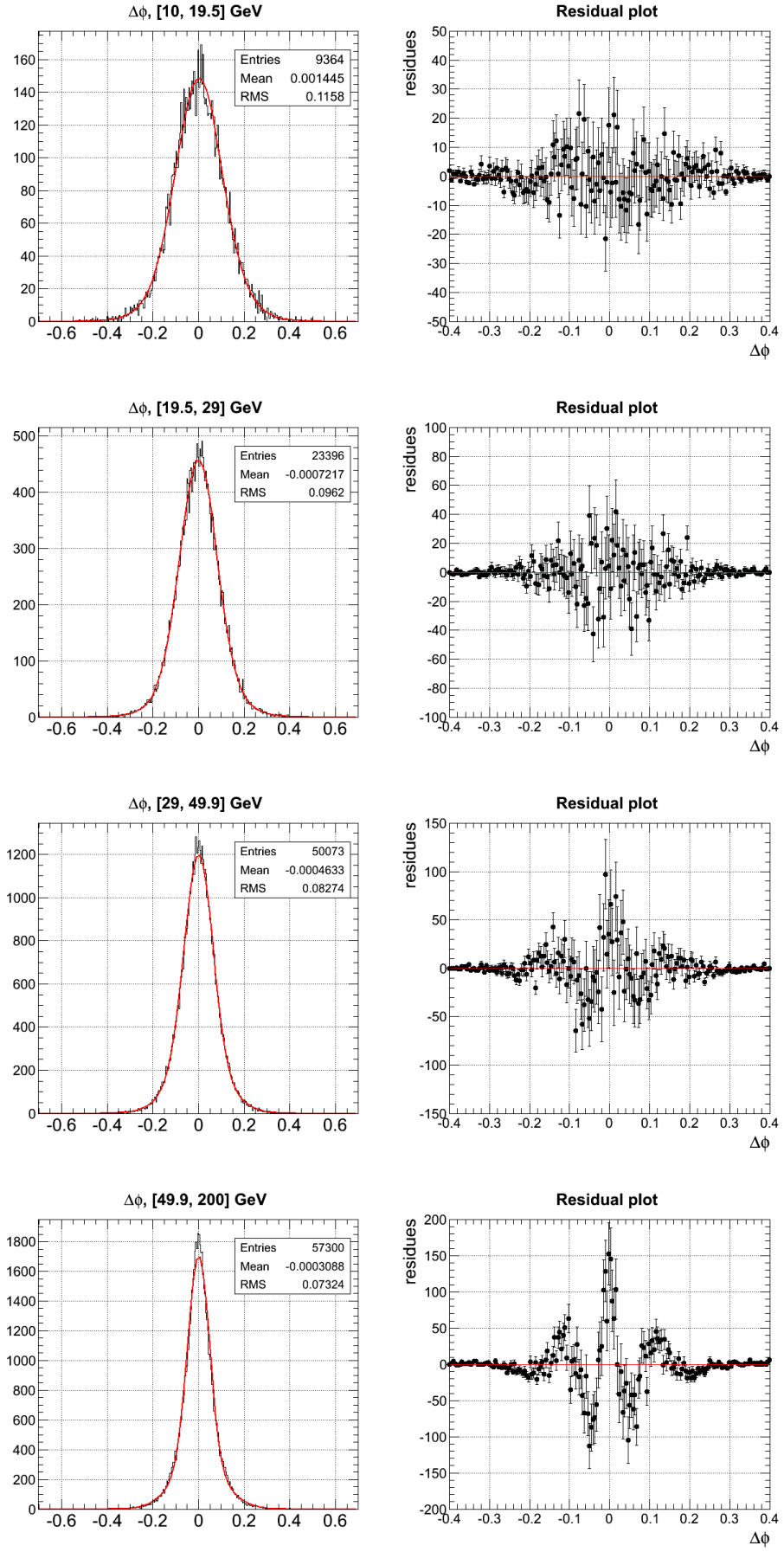

Figure 5.29: Fits and residual plots for $\Delta\phi$ for jet without muon, **Data 2010**.

5.4 Further checks

5.4.1 A comparison between Data and MC

Here we want to do some checks to compare the MC and Data distributions, in particular we are interested to understand if there are differences as a function of flight length (*Lflight*) of the decaying hadron. If we call L the *Lflight*, we can separate and plot the distributions for $L > 1$ cm or $L < 1$ cm. Then we compare Data with MC distributions, also in this case evaluating the RMS. In particular we expect two things:

1. RMS of Data are larger than MC, as always;
2. RMS in case of $L > 1$ cm are smaller then in case $L < 1$ cm, because the resolutions are better for $L > 1$ cm.

We plot $\Delta\eta$ and $\Delta\phi$ for all the cases, *jet with or without muon*, from Figure 5.30 to Figure 5.33.

In Table 5.8 and 5.9 we resume the RMS for the $\Delta\eta$ and $\Delta\phi$ distributions.

		$L < 1$ cm	$L > 1$ cm
RMS $\Delta\eta$	MC	0.0671	0.0493
	Data	0.0733	0.0572
RMS $\Delta\phi$	MC	0.0688	0.0505
	Data	0.0726	0.0541

Table 5.8: Case *jet with muon*.

		$L < 1$ cm	$L > 1$ cm
RMS $\Delta\eta$	MC	0.0830	0.0628
	Data	0.0866	0.0697
RMS $\Delta\phi$	MC	0.0856	0.0655
	Data	0.0876	0.0676

Table 5.9: Case *jet without muon*.

These tables show that our expectations are satisfied in all cases.

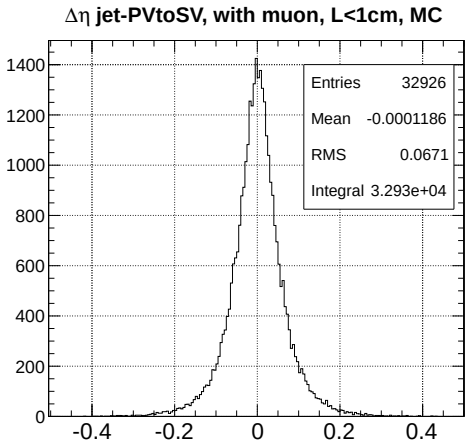

(a) $L < 1$ cm, MC.

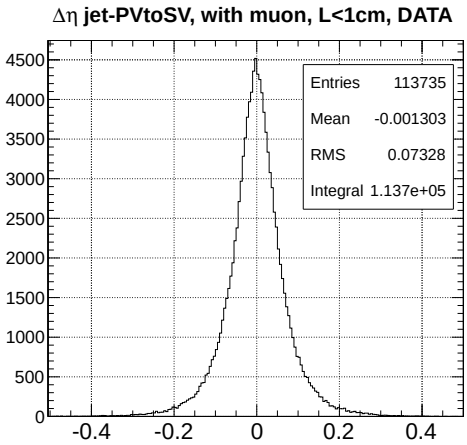

(b) $L < 1$ cm, Data.

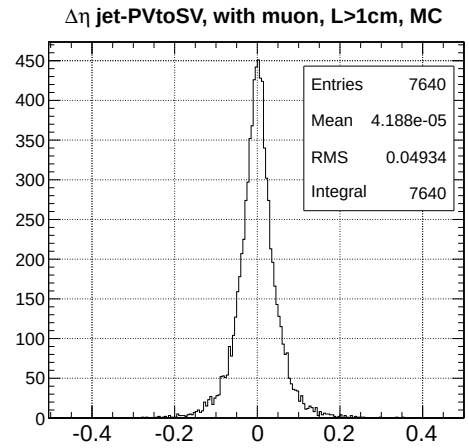

(c) $L > 1$ cm, MC.

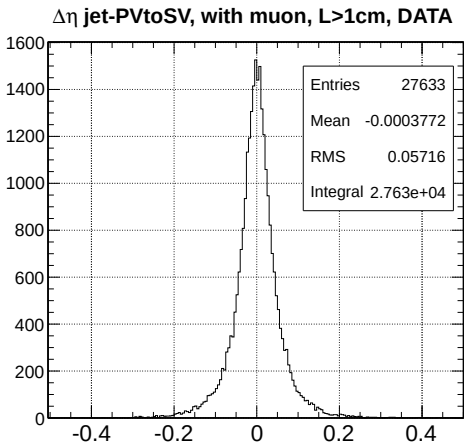

(d) $L > 1$ cm, Data.

Figure 5.30: $\Delta\eta$ distributions for jet with muon.

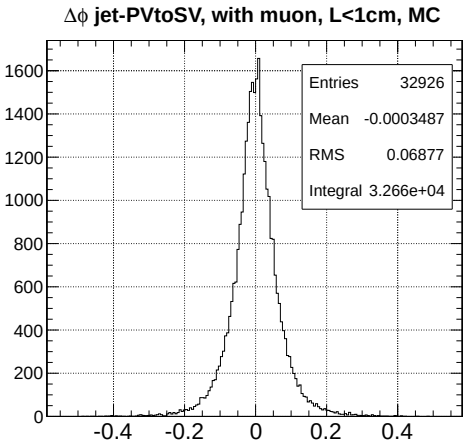

(a) $L < 1$ cm, MC.

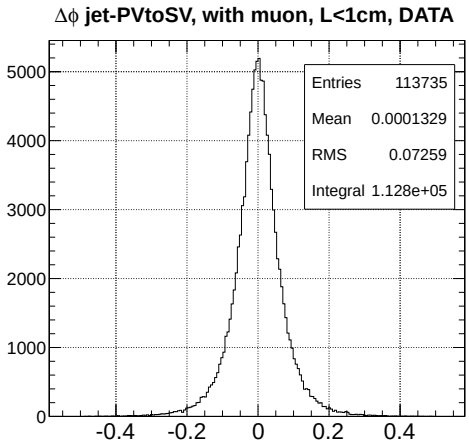

(b) $L < 1$ cm, Data.

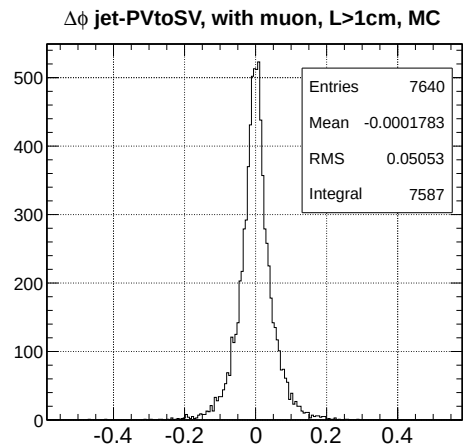

(c) $L > 1$ cm, MC.

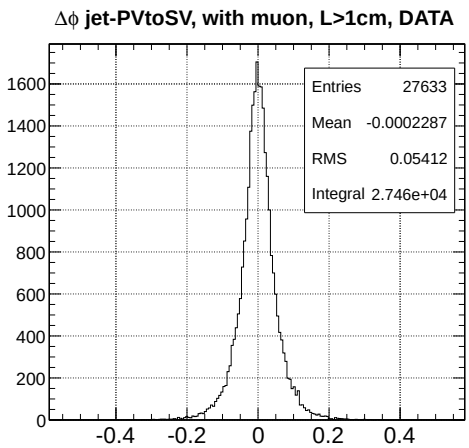

(d) $L > 1$ cm, Data.

Figure 5.31: $\Delta\phi$ distributions for jet with muon.

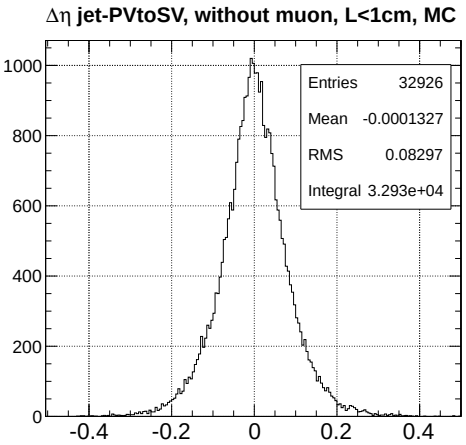

(a) $L < 1$ cm, MC.

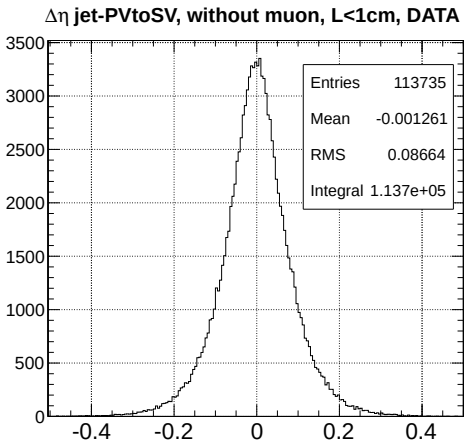

(b) $L < 1$ cm, Data.

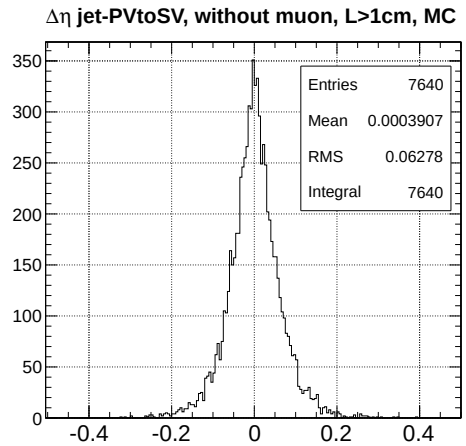

(c) $L > 1$ cm, MC.

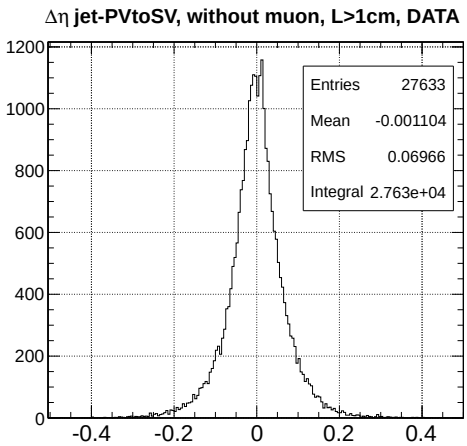

(d) $L > 1$ cm, Data.

Figure 5.32: $\Delta\eta$ distributions for jet without muon.

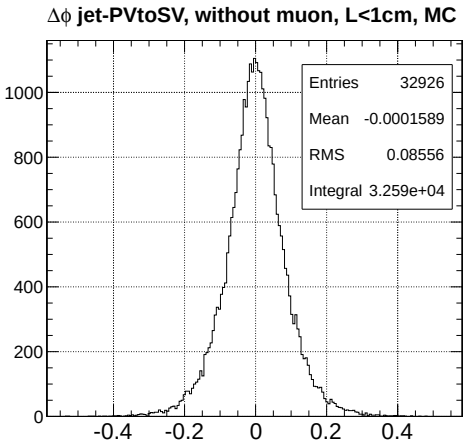

(a) $L < 1$ cm, MC.

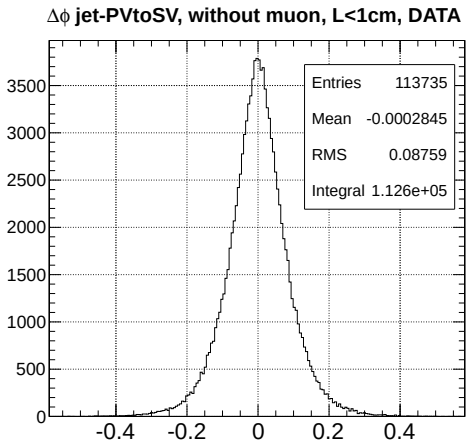

(b) $L < 1$ cm, Data.

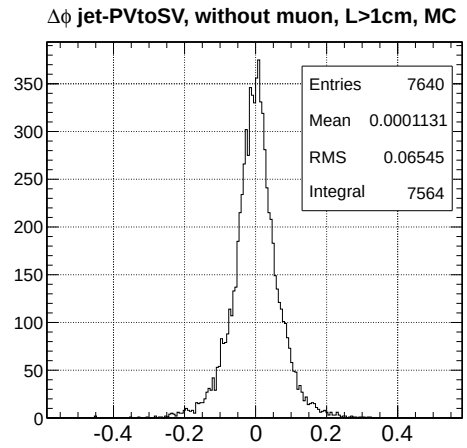

(c) $L > 1$ cm, MC.

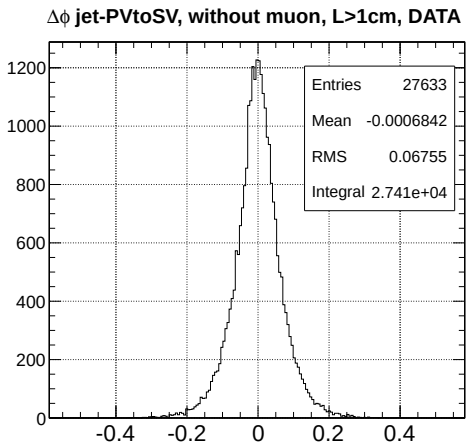

(d) $L > 1$ cm, Data.

Figure 5.33: $\Delta\phi$ distributions for jet without muon.

5.4.2 A sight on classes

During this chapter we talked about the class 1 as the class, in MC simulation, in which we have the muons from direct decay of B hadron $B \to \mu\nu_{mu}X$. Now we consider the other classes as defined in the introduction of this chapter.

In our MC sample with 281 342 events we don't find muon from class 3 (prompt muons) , that because this class is unlikely respect to the others. So we report in Figure 5.34, 5.35, 5.36, 5.37 and 5.38 the distributions of muons for classes 1, 2, 4 , 5 and 6 as a function of *Lflight* and the corresponding percentage respect to the events in presence of SV.

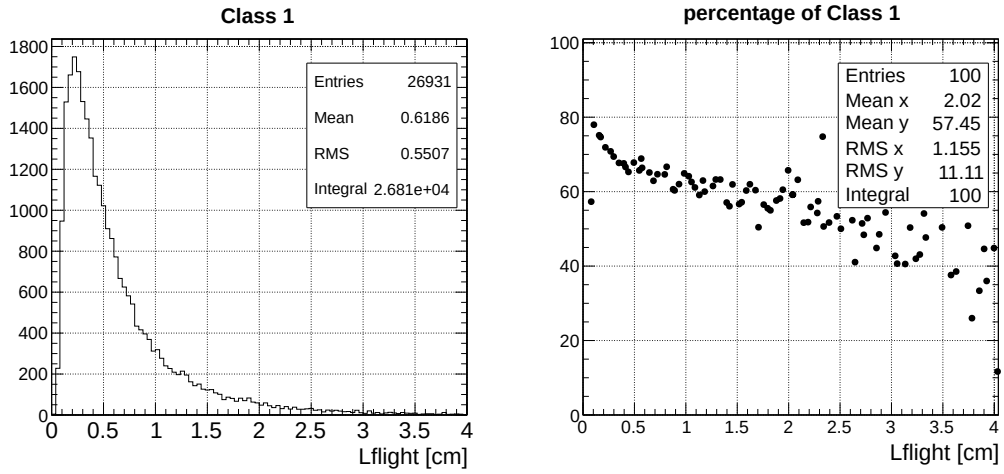

Figure 5.34: Class 1: primary B decays (B $\to \mu\nu_{\mu}X$)

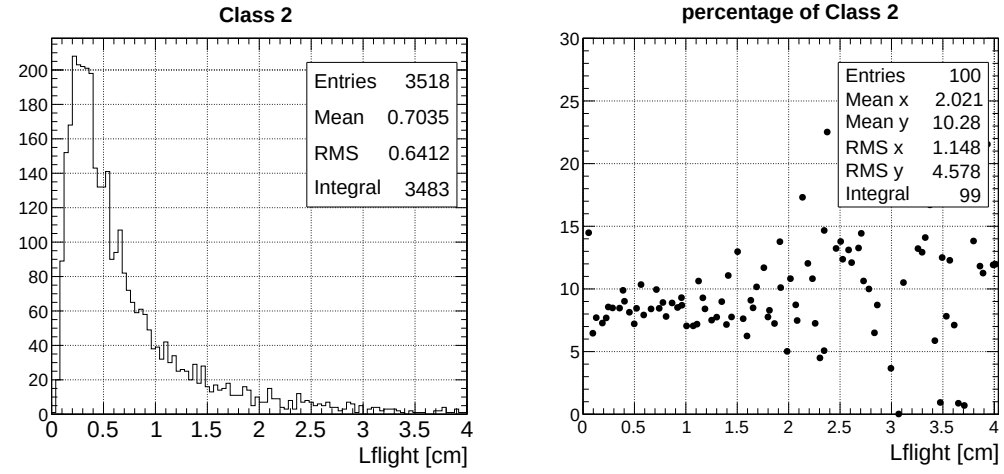

Figure 5.35: Class 2: primary C decays (C $\to \mu\nu_{\mu}X$)

Only one consideration: when *Lflight* increases, the percentage of class 5 (sequential decays) increases. This is the reason, at first sight, why the percentage of class 1 drops. There aren't other particular effects in these plots, many classes have poor statistics in order to do other considerations.

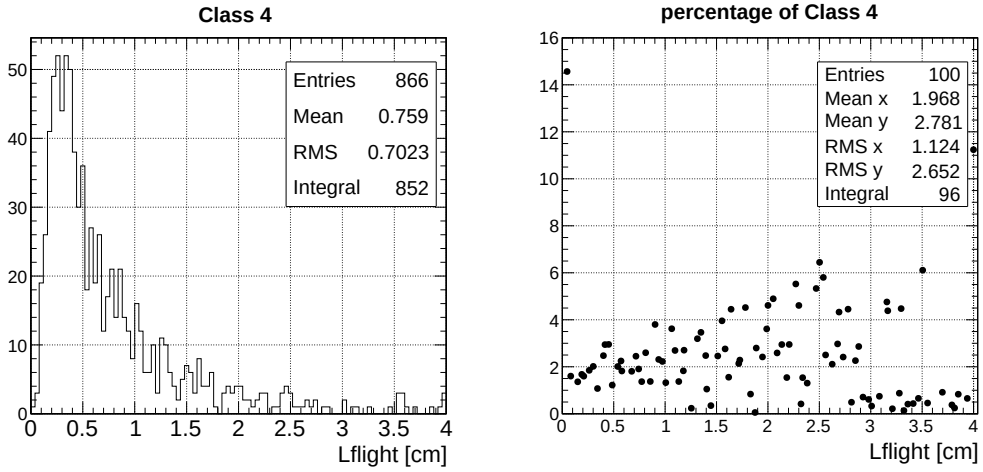

Figure 5.36: Class 4: muons from the decay in flight of a charged pion or kaon.

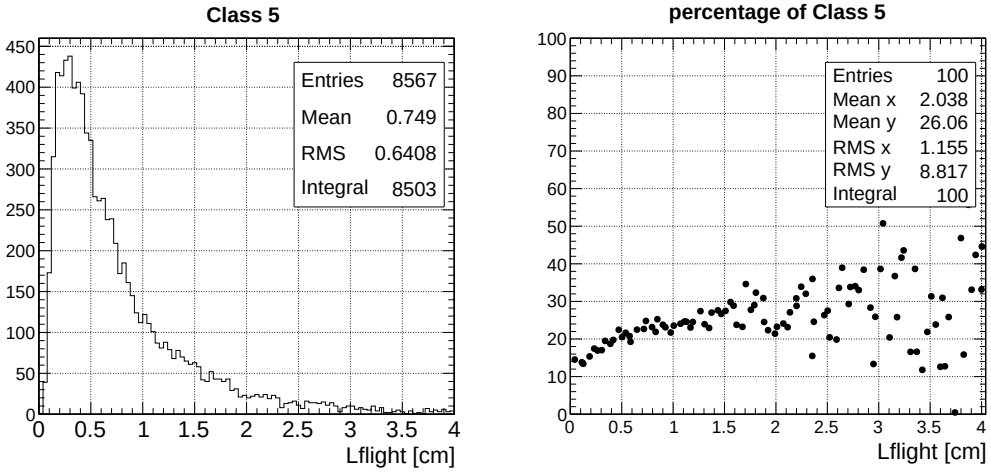

Figure 5.37: Class 5: sequential B decays (B $\rightarrow C \rightarrow \mu$ or B$\rightarrow \tau \rightarrow \mu$)

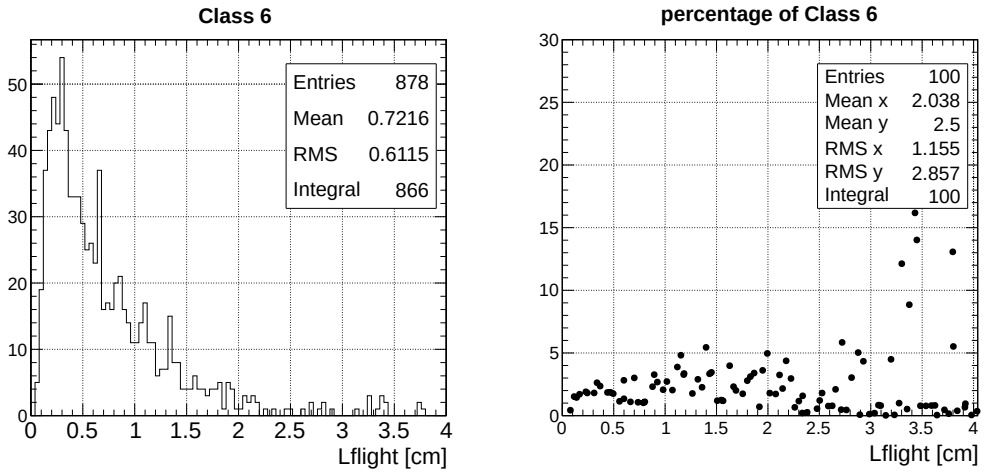

Figure 5.38: Class 6: fake, where there is no relation between the track reconstructed and the particle produced at the generation stage.

Chapter 6

Conclusions

This thesis, carried out within the CMS collaboration at LHC, was intended to make a preliminary studies for a measurement of the B-mixing with di-muon events, in particular a measurement of the average time integrated mixing probability $\bar{\chi}$.

As a first analysis we have evaluated the pile up effect on 2010 and 2011 data samples. As we have seen in 2010 we have less PU events respect to 2011, as we expected because of the increases of luminosity. However the PU effect is always small, the fraction of PU events in fact is always under 1%. This means that for successive analysis the PU effect is negligible also for the 2011 data where the luminosity is larger. Since the PU effect is usually rejected by imposing that the two muons come from same vertex, we have compared the data samples with a MC simulation devoid of PU. We have not found substantial differencies between data and MC distribution, confirming that PU effect is not important for the samples available.

As a second study we have determined the angular resolution in the measurement of the B-direction, to obtain a systematic uncertainty for the analysis of time integrated mixing probability. In this case we had available MC simulations only for 2010, so we have compared it with data 2010. From this comparison we have found the smearing between data and MC in some range of the jet energy (between 10 and 200 GeV), without noting anomalies.

The tools developed in the latter analysis could be used for the data 2011 as soon as a MC simulation relative to 2011 is available.

Bibliography

[1] S. Glashow, *Partial symmetries of weak interactions*, Nucl. Phys., **22** (1961) 579588.

[2] S. Weinberg, *A model of leptons*, Phys. Rev. Lett., **19** (1967) 12641266.

[3] A. Salam, Elementary Particle Physics: Relativistic Groups and Analyticity (Nobel Symposium No. 8) (ed. Svartholm, N.) **367** (Almqvist and Wiksills, Stockholm, 1968).

[4] Amsler C. et al. , Review of particle physics (and 2009 partial update for the 2010 edition). Phys. Lett., B667:1, 2008.

[5] LEP Collaboration, " LEP Electroweak Working Group". [http://lepewwg.web.cern.ch/LEPEWWG/].

[6] Tevatron Collaboration, "Tevatron Electroweak Working Group". [http://tevewwg.fnal.gov/].

[7] N. Cabibbo, *Unitarity Symmetry and Leptonic Decays*, Phys. Rev. Lett. **10** (1963) 531- 533.

[8] M. Kobayashi and T. Maskawa, *CP-Violation in the Renormalizable Theory of Weak Interaction*, Prog. Theor. Phys. **49** (1973) 652-657.

[9] D. J. Gross and F. Wilczek, *Asymptotically Free Gauge Theories. 1*, Phys. Rev., D8 (1973) 3633-3652.

[10] H. D. Politzer, *Reliable Perturbative Results for Strong Interactions*, Phys. Rev. Lett., 30 (1973) 1346-1349.

[11] H. D. Politzer, *Asymptotic Freedom: An Approach to Strong Interactions*, Phys. Rept., 14 (1974) 129-180.

[12] R. P. Feynman, *Quantum Electrodynamics*, W. A. Benjamin, Inc., New York (1961).

[13] S. S. Schweber, *QED and the men who made it: Dyson, Feynman, Schwinger, and Tomonaga*, Princeton, USA: Univ. Pr. (1994) 732 p.

[14] G. Sterman et al., *Handbook of perturbative QCD*, Rev. Mod. Phys., 67 (1995) 157-248.

[15] S. Bethke, *The 2009 World Average of α_s*, Eur. Phys. J., C64 (2009) 689-703.

[16] D. Duke and R. Roberts, *"Determinations of the QCD strong coupling α_s and the scale Λ_{QCD}"*, Physics Reports 120 (1985), no. 5-6 275-368. [doi:10.1016/0370-1573(85)90112-7].

[17] R. Ellis, H. Georgi, M. Machacek, H. Politzer, and G. G. Ross, *"Perturbation theory and the parton model in QCD"*, Nuclear Physics B 152 (1979), no. 2 285-329. [doi:10.1016/0550-3213(79)90105-6].

[18] J. C. Collins, D. E. Soper, and G. F. Sterman, *"Factorization of Hard Processes in QCD"*, Adv. Ser. Direct. High Energy Phys. 5 (1988) 1-91, [hep-ph/0409313].

[19] J. C. Collins and D. E. Soper, *"The Theorems of Perturbative QCD"*, Ann. Rev. Nucl. Part. Sci. 37 (1987) 383-409. [doi:10.1146/annurev.ns.37.120187.002123].

[20] J. C. Collins, D. E. Soper, and G. Sterman, *"Heavy particle production in high-energy hadron collisions"*, Nuclear Physics B 263 (1986), no. 1 3760. [doi:10.1016/0550-3213(86)90026-X].

[21] J. Pumplin et al., *"New generation of parton distributions with uncertainties from global QCD analysis"*, JHEP 07 (2002) 012, [hep-ph/0201195].

[22] A. Martin, R. Roberts, W. Stirling, and R. Thorne, *"MRST2001: partons and α_s from precise deep inelastic scattering and Tevatron jet data"*, The European Physical Journal C - Particles and Fields 23 (2002) 73-87. [doi:10.1007/s100520100842].

[23] A. D. Martin, W. J. Stirling, R. S. Thorne, and G. Watt, *"Parton distributions for the LHC"*, Eur. Phys. J. C63 (2009) 189-285. [doi:10.1140/epjc/s10052-009-1072-5].

[24] R. D. Ball, L. D. Debbio, S. Forte, A. Guffanti, J. I. Latorre, A. Piccione, J. Rojo, and M. Ubiali, *"A determination of parton distributions with faithful uncertainty estimation"*, Nuclear Physics B 809 (2009), no. 1-2 1-63. [doi:10.1016/j.nuclphysb.2008.09.037].

[25] R. D. Ball, L. D. Debbio, S. Forte, A. Guffanti, J. I. Latorre, A. Piccione, J. Rojo, and M. Ubiali, *"Erratum to: "A determination of parton distributions with faithful uncertainty estimation"* [Nucl. Phys. B 809 (2009) 1-63]", Nuclear Physics B 816 (2009), no. 1-2 293. [doi:10.1016/j.nuclphysb.2009.02.027].

[26] M. Gluck, J. F. Owens, and E. Reya, *"Gluon contribution to hadronic J/ψ production"*, Phys. Rev. D 17 (May, 1978) 2324-2331. [doi:10.1103/PhysRevD.17.2324].

[27] B. Combridge, *Associated production of heavy avour states in pp and $p\bar{p}$ interactions: Some QCD estimates"*, Nuclear Physics B 151 (1979), no. 0 429-456. [doi:10.1016/0550-3213(79)90449-8].

[28] J. Babcock, D. Sivers, and S. Wolfram, *Quantum-chromodynamic estimates for heavy-particle production"*, Phys. Rev. D 18 (Jul, 1978) 162-181. [doi:10.1103/PhysRevD.18.162].

[29] Particle Data Group, *"Review of Particle Physics"*, J. Phys. G 37 (2010) 075021. [doi:10.1088/0954-3899/37/7A/075021].

[30] E. . Bruning et al., *"LHC design report. Vol. I: The LHC main ring"*. CERN-2004-003-V-1, [http://lhc.web.cern.ch/lhc/LHC-DesignReport.html].

[31] ATLAS Collaboration, *"The ATLAS Experiment at the CERN Large Hadron Collider"*, JINST 3 (2008) S08003. [doi:10.1088/1748-0221/3/08/S08003].

[32] CMS Collaboration, *"The CMS Experiment at the CERN LHC"*, JINST 3 (2008) S08004. [doi:10.1088/1748-0221/3/08/S08004].

[33] LHCb Collaboration, *"The LHCb Detector at the CERN LHC"*, JINST 3 (2008) S08005. [doi:10.1088/1748-0221/3/08/S08005].

[34] ALICE Collaboration, *"The ALICE Experiment at the CERN LHC"*, JINST 3 (2008) S08002. [doi:10.1088/1748-0221/3/08/S08002].

[35] CMS Collaboration, *"CMS Luminosity - Public Results"*. [https://twiki.cern.ch/twiki/bin/view/CMSPublic/LumiPublicResults].

[36] CMS Collaboration, *"CMS Physics Technical Design Report Volume I: Detector Performance and Software"*. Technical Design Report CMS Series. CERN, Geneva, CMS-TDR-008-1, 2006. [https://cdsweb.cern.ch/record/922757].

[37] CMS Collaboration, *"CMS physics Technical Design Report, Volume II: Physics Performance"*, vol. 34. 2007. [doi:10.1088/0954-3899/34/6/S01].

[38] CMS Collaboration, *"The CMS Magnet Project: Technical Design Report"*. Technical Design Report CMS Series. CERN, CMS-TDR-001, 1997. [https://cdsweb.cern.ch/record/331056].

[39] CERN, *"Document Server Photo Archive"*. [http://cdsweb.cern.ch/collection/Photos].

[40] CMS Collaboration, *"The CMS Tracker Project: Technical Design Report"*. Technical Design Report CMS Series. CERN, CMS-TDR-005, 1998. [https://cdsweb.cern.ch/record/368412].

[41] CMS Collaboration, *"Addendum to the CMS Tracker Technical Design Report"*. Technical Design Report CMS Series. CERN, CMS-TDR-005 Addendum 1, 2000. [https://cdsweb.cern.ch/record/490194].

[42] W. A. et al., *"Track reconstruction in the CMS tracker"*. CMS NOTE-2006/041, [https://cdsweb.cern.ch/record/934067].

[43] Pierre and Billoir, *"Progressive track recognition with a Kalman-like fitting procedure"*, Computer Physics Communications 57 (1989), no. 1-3 390-394. [doi:10.1016/0010-4655(89)90249-X].

[44] T. Speer, K. Prokofiev, R. Fruhwirth, W. Waltenberger, and R. Vanlear, *"Vertex Fitting in the CMS Tracker"*. CMS NOTE-2006/032, [https://cdsweb.cern.ch/record/927395].

[45] CMS Collaboration, *"The CMS Muon Project: Technical Design Report"*. Technical Design Report CMS Series. CERN, CMS-TDR-003, 1997. [https://cdsweb.cern.ch/record/343814].

[46] CMS Collaboration, *"The CMS Electromagnetic Calorimeter Project: Technical Design Report"*. Technical Design Report CMS Series. CERN, CMS-TDR-004, 1997. [https://cdsweb.cern.ch/record/349375].

[47] CMS Collaboration, *"The CMS Hadron Calorimeter Project: Technical Design Report"*. Technical Design Report CMS Series. CERN, CMS-TDR-002, 1997. [https://cdsweb.cern.ch/record/357153].

[48] CMS Collaboration, *"The CMS TriDAS Project: Technical Design Report, Volume 1 - The Trigger System"*. Technical Design Report CMS Series. CERN, CMS-TDR-006-1, 2000. [https://cdsweb.cern.ch/record/706847].

[49] CMS Collaboration, *"The CMS TriDAS Project: Technical Design Report, Volume 2 - Data Acquisition and High Level Trigger"*. Technical Design Report CMS Series. CERN, CMS-TDR-006-2, 2002. [https://cdsweb.cern.ch/record/578006].